Honeycomb lattices of superconducting microwave resonators : Observation of topological Semenoff edge states

Alexis Morvan

université PARIS-SACLAY

NNT : 2019SACLS037

Thèse de doctorat

UNIVERSITÉ PARIS SUD

Comprendre le monde, construire l'avenir

Honeycomb lattices of superconducting microwave resonators: Observation of topological Semenoff edge states

Thèse de doctorat de l'Université Paris-Saclay
préparée à l'Université Paris-Sud, au Laboratoire de Physique du Solide (LPS)

École doctorale n°564 Physique en île-de-France (EDPIF)
Spécialité de doctorat: Physique

Thèse présentée et soutenue à Orsay, le 7 février 2019, par

Alexis Morvan

Composition du Jury :

Karyn Le Hur Directeur de recherche, Centre de Physique Théorique, Ecole Polytechnique	Présidente
Jérôme Cayssol Professeur, Laboratoire Ondes et Matière d'Aquitaine, Université Bordeaux	Rapporteur
Fabrice Mortessagne Professeur, Laboratoire de Physique de la Matière Condensée, Université Nice Sophia Antipolis	Rapporteur
Jean-Noël Fuchs Directeur de recherche, Laboratoire de Physique Théorique de la Matière Condensée, Sorbonne Université	Examinateur
Fabrice Lemoult Chargé de recherche, Institut Langevin, ESPCI	Examinateur
Julien Gabelli Chargé de recherche, Laboratoire de Physique des Solides, Université Paris-Sud	Directeur de thèse
Jérôme Esteve Chargé de recherche, Laboratoire de Physique des Solides, Université Paris-Sud	Co-directeur (Invité)

Remerciement

Cette thèse n'aurait pas été possible sans un environnement favorable et une multitude de personnes pour m'aider dans ce projet. Je tiens donc avant tout à remercier toutes les personnes qui m'ont aidé aux différentes étapes de cette thèse.

Tout d'abord, je remercie mes deux directeurs de thèse Julien Gabelli et Jérôme Estève pour m'avoir donné l'opportunité de réaliser cette thèse ainsi que pour leur accompagnement tout au long de celle-ci. Sans vous rien n'aurait été possible. Je tiens aussi à remercier tout particulièrement Jean-Noël Fuchs qui nous a présenté les modes de Semenoff et a répondu à toutes mes questions sur les propriétés topologiques de ce système.

Ce travail a été effectué au sein du groupe NS2 du LPS. Je tiens à remercier tous les membres de ce groupe : Marco Aprilli, Charis Quay, Julien Basset et Freek Massee, pour leurs conseils et pour les discussions de physiques que nous avons pu avoir ensemble. Je suis tout particulièrement reconnaissant aux thésards du groupe : Mathieu Féchant, Gianluca Aiello, Marko Kuzmanovich, Cyril Vaneph et Pierre Février. Vous avez été d'une aide et d'un soutien quotidien. J'ai réellement apprécié ces années avec vous ! Les échantillons de cette thèse ont été réalisés au LPS et au C2N. Pour tout ce qui concernait la fabrication au LPS, j'ai bénéficié de l'aide et des conseils de Sylvie Gauthier et Raphael Weil que je remercie ainsi que David Bouville pour son aide pour la part de fabrication réalisée au C2N.

Je tiens à remercier l'ensemble du groupe MESO : Hélène Bouchiat, Sophie Guéron, Richard Deblock et Meydi Ferrier. Leurs thématiques de recherche étant proche du groupe NS2, j'ai bénéficié de leurs nombreux conseils et des nombreuses discussions que nous avons eues. Merci également aux thésards : Anil Murani, Raphaëlle Delagrange et Kamilla Yunusova.

Je remercie également la direction et l'administration du LPS, notamment Véronique Thieulart pour l'aide qu'elle m'a apportée pour résoudre les questions administratives, et Sandrine Ermisse, comptable responsable de notre groupe.

Je tiens à remercier les nombreux thésards du LPS que je n'ai pas encore mentionnés mais qui ont su animer ce laboratoire : Raphaelle Taub, Anais Giustiniani, Thibaut gaillard, Frédéric Combe, Serguei Tchoumakov, Eloi Haltz et un big up à Marceau Hénot, mon acolyte d'escalade avec qui j'ai discuté de tout et n'importe quoi au bloc de Massy.

Je remercie l'ensemble des membres du jury de thèse pour avoir accepté d'y participer, ainsi que pour tous les commentaires et remarques qu'ils ont pu formuler et qui ont permis d'améliorer cette thèse.

J'ai aussi pu compter tout au long de cette thèse sur les nombreux soutiens de ma famille et de mes amis. Merci à Marie-Amélie de m'avoir supporté quotidiennement, merci aussi à ma famille pour son soutien.

Contents

Introduction

This thesis is part of a long-term project that aims to implement a quantum simulator using superconducting circuits, more specifically superconducting resonators that resonate in the microwave domain. The idea of a quantum simulator, which was developed almost 40 years ago by R.Feymann [1], is to use a well-controlled quantum system enabling the simulation of complex quantum matter. Experimental efforts to implement this idea have been pursued using ultracold atoms, trapped ions, photonic systems, NMR and other systems [2]. Among all the models that could be of interest to a quantum simulator, one is the Bose-Hubbard (BH) model, which is the canonical model for interacting bosons on a lattice. This model is particularly rich if one can implement a two-dimensional (2D) lattice, whose band structure has non trivial topological properties. Simulating 2D strongly correlated quantum fluids is motivated by the vast amount of results and questions raised by studies on the quantum Hall effect in 2D electron gases. The quantum Hall effect results from the Landau level quantization under a strong external magnetic field. Each filled Landau level is characterized by a bulk topological invariant: the first Chern number. With interactions, incompressible bulk states appear for specific partial fillings of the Landau levels [3, 4]. Those Fractional Quantum Hall states support fractionally charged excitations and non trivial edge modes. The quantum Hall physics has been generalized to topological insulators with dispersive bands carrying a nontrivial Chern number, the so-called Chern insulators or Quantum Anomalous Hall insulators both in the absence [5] and in presence of interactions, fractional Chern insulators [6].

The simulation of these fascinating effects in lattices of superconducting resonators has been proposed theoretically and seems to be an interesting route that deserves to be explored [7–10]. Superconducting circuits have become one of the most advanced experimental platform to tailor artificial quantum systems in particular for quantum information processing, a field of research known as circuit Quantum ElectroDynamics (cQED) [11–16]. In terms of lattice systems, the excitations are microwave photons ($f \simeq 6\,\mathrm{GHz}$) stored in superconducting resonators with high quality factor $Q \simeq 10^5$. The coupling between sites can be engineered from a few MHz to several hundreds MHz. The main interest of this platform is the possibility to reach the strongly interacting regime using Josephson junctions, which are non-linear and non-dissipative inductances. The quantum regime is reached for temperatures given by $k_B T \ll hf$, which corresponds to $T \ll 300\,\mathrm{mK}$, a condition that is easily reached in commercial dilution refrigerators that go down to temperatures $T \simeq 10\,\mathrm{mK}$. So far, experiments are far from realizing 2D lattices combining strong photon-photon interaction with non-trivial topology [17, 18]. It seems natural to first address separately the control of the

interaction and of the band structure. Concerning interactions, some recent experiments have demonstrated that the strongly interacting regime can be reached in 1D chains of resonators [19, 20], but are limited so far to small systems with less than 20 resonators.

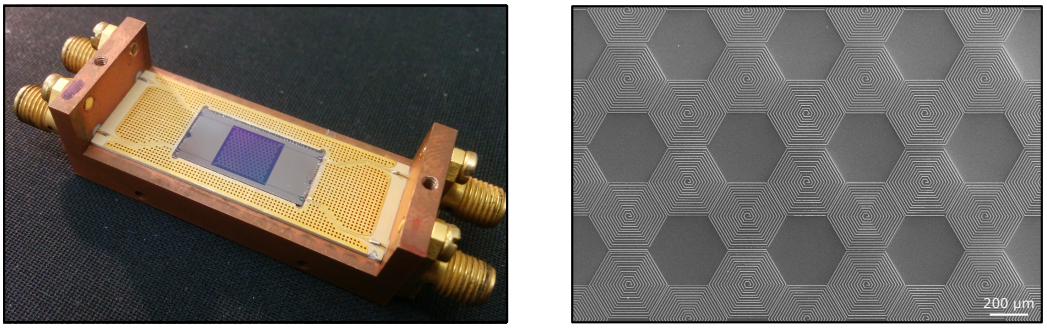

Figure 1: Honeycomb lattice of superconducting spiral resonators. The left image shows the sample installed in its holder. The right image is a SEM image of the lattice.

The second research direction, towards the realization of engineered band structures for photons, catches up with the rapidly growing field of photonic lattices [21–23]. One key motivation in the field is to bring to light topological properties of lattices that have been historically discovered in condensed matter physics [5, 24–27]. One strong motivation is the realization of topologically protected propagation channels that appear at the interface between two materials with different topological invariants [28–32]. Highlighting these topologically protected states constitutes a grail that requires the challenging realization of a lattice with broken time-reversal symmetry. Experiments in this direction have been performed in the optical domain using coupled waveguides [33, 34] and coupled ring resonators [35, 36], in the microwave domain [37, 38] and in the radio-frequency domain with printed board circuits [39]. However, it is still possible to observe topological effects in lattices with time reversal symmetry. It is one of the main goal of this thesis. The most emblematic system is undoubtedly the famous honeycomb lattice and its Dirac cones. They have already been studied in lattices of semi-conductor micro-cavity polaritons [40–42], dielectric microwave resonators [43, 44], soda can [45], two-dimensional electron gas [46], waveguides [47–49], nanopatterned GaAs quantum wells [50], and superconducting microwave billiards [51].

At the beginning of this thesis, we decided to focus on the realization of relatively large lattices in contrast to what had been realized so far in cQED. Such lattices had not yet been realized using superconducting resonators and we had first to answer very basic questions: is it possible to design a lattice to simulate any tight-binding model? If yes, is there an optimal architecture to control the hopping term in the tight binding Hamiltonian? Could we keep the disorder due to lithography process under control? We decided to concentrate our efforts on the honeycomb lattice because of its interesting topological properties and realized a first series of experiments to characterize such a lattice (see figure 1). An important experimental development was the realization of a laser scanning imaging setup that allowed us to measure the spatial distribution of the resonant modes across the lattice (see figure 2). This technique is similar to the laser scanning microscopy developed to observe the current density in superconductor films [52–54]. By Fourier transforming these images, the momentum of the mode is obtained, which enables us to reconstruct the dispersion relation in the first Brillouin zone

and to compare it to our *ab initio* calculations (see figure 3).

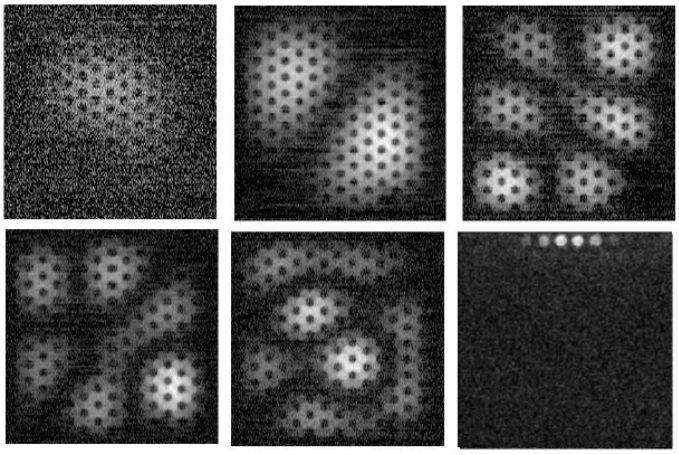

Figure 2: Spatial distribution of some resonant modes observed in a honeycomb lattice of superconducting resonators. The sample corresponds to **HoneycombSi**. The image brightness is proportional to the local microwave intensity.

The good agreement between our data and the model allowed us to consider a more advanced experiment aiming at the observation of the topological edge states known as Semenoff states. The band structure of the honeycomb lattice consists of two bands that touch at Dirac points. By introducing an on-site energy imbalance between the two inequivalent sites of the lattice, a gap opens at the Dirac points. Semenoff predicted that, at the interface between two lattices with opposite mass imbalance, propagating edge states appear that cross the gap [55]. We have realized such a domain wall between two honeycomb lattices of superconducting resonators with opposite on-site energy imbalance. Using the mode imaging technique (see figure 4), we have reconstructed the dispersion relation of the edge states that appear at the domain wall. These different experiments are detailed in the manuscript following the outline below:

Chapter 1 introduces the two tight-binding models realized in this thesis. The first part gives the band structure of the honeycomb lattice and shows the effects of next-nearest neighbors on the density of states (DOS). We then use an argument based on the low energy approximation to explain the existence of zigzag and bearded edge states but the absence of edge states on the armchair boundary of the honeycomb lattice. We further analyse these edge states with the tight-binding model to characterize them (dispersion relation, penetration length,...). The second part of this chapter is dedicated to the Semenoff insulator. We derive its band structure using the tight-binding model and derive the existence of propagating edge states along the domain wall between two Semenoff insulators with opposite mass with a low-energy model [55].

Chapter 2 presents the spiral superconducting resonators and how to design a lattice using electromagnetic (EM) simulation software. We characterize the spiral resonator that we used for all our lattices. We then show how to calculate the coupling between two spiral resonators. We then develop two models to characterize the electromagnetic resonators. The first model is based on the admittance matrix. It will be called *admittance model*. We present how to calculate the band structure by simulating a few number of sites in the lattice. The second

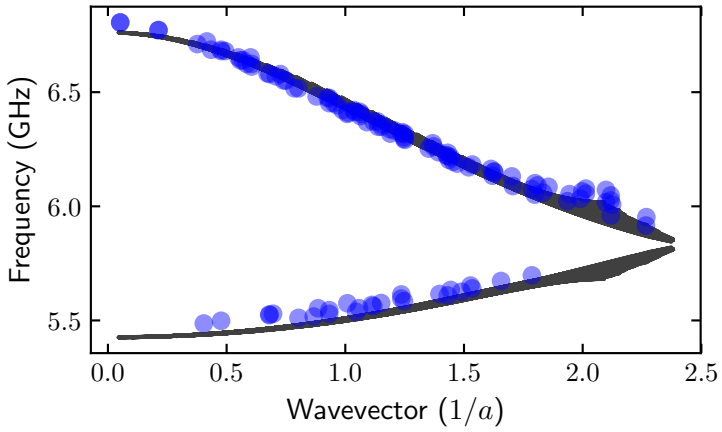

Figure 3: Dispersion relation of the resonant modes of a honeycomb lattice of superconducting resonators. The experimental data points come from the measurement of **ZigzagSi**. They are in good agreement with the predictions of an ab initio model of the lattice.

model is based on a coupled mode theory (CMT). We refer to this model as *CMT model*. We use the CMT to take into account the coupling between resonators and extend it to a periodic system. This approach uses the Maxwell equations to directly calculate the resonant frequencies from the overlap integrals associated to the magnetic and electric couplings.

Chapter 3 explains the laser scanning microscopy (LSM) technique. This experimental technique enables to probe the spatial distribution of the modes of the superconducting resonator lattices. This measurement corresponds to the measurement of the energy stored in the resonators and therefore makes it possible to give the spatial dependence of the corresponding electromagnetic mode and to label it.

Chapter 4 is devoted to the design and the study of the sample **HoneycombSi** corresponding to the honeycomb lattice on a silicon substrate. We present the design of the sample and characterize it. We then present the modes measured with the LSM. The LSM gives access to the value of weight of the modes squared. To retrieve their relative sign, we designed a optimization algorithm. Thanks to the mode imaging we are able to label the modes **i.e.** to determine the momentum quantum number (k_x, k_y) associate to the resonant frequency. This labelling allows us to reconstruct the band structure of the honeycomb lattice. This band structure is compared to both *admittance model* and *CMT model* presented in chapter 2 as well as a phenomenological model deduced from the DOS. Finally, we present the study of the zigzag and bearded edge modes of the honeycomb lattice by presenting their 1D band structure and their penetration length.

Chapter 5 present the design and the characterization of the domain wall edge states presented in chapter 1. We present the design of a Semenoff insulator sample with different domain walls. It gives rise to measurements of different samples named **ZigzagSi**, **ArmchairSi**, **ZigzagSa** where zigzag/armchair stand for the domain wall type and Si/Sa for the substrate material (silicon or sapphire). As for sample **HoneycombSi**, we were able to reconstruct the band structure of these samples and compare it to theoretical models. We then show that Semenoff edge states are localized on the domain wall. The observation of the edge states complements the main result of this thesis. We characterize them with

their band structure and their penetration length. Finally, we study disorder by looking at localized states induced by vacancies in the sample **ZigzagSi**.

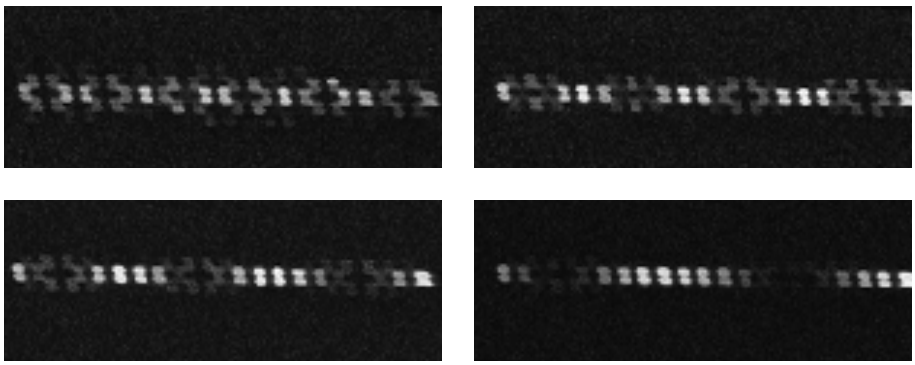

Figure 4: Experimental images of Semenoff edge states localized at the interface between two different honeycomb lattices. The existence of the states is due to the different topological properties of the two lattices.

Introduction (Français)

Cette thèse s'inscrit dans un cadre plus général de la réalisation d'un simulateur quantique avec des circuits supraconducteurs, et plus précisément en utilisant des résonateurs supraconducteurs résonnant dans le domaine des micro-ondes. L'idée d'un simulateur quantique a été développée il y a près de 40 ans par R. Feymann [1] : en utilisant des systèmes quantiques simples et bien contrôlés il est possible de simuler des modèles quantiques complexes. De nombreux efforts expérimentaux ont tenté de réaliser un simulateur quantique avec différents supports physiques comme les atomes ultra-froids, les ions piégés, les systèmes photoniques, la RMN et d'autres systèmes [2]. Parmi les modèles pertinents pour la réalisation d'un simulateur quantique, le modèle de Bose-Hubbard est le modèle type de bosons en interaction sur un réseau ou fluide quantique fortement corrélé. Ce modèle est particulièrement riche si l'on peut l'implémenter sur un réseau bidimensionnel (2D) dont la structure de bande possède des propriétés topologiques non triviales. La simulation de ces fluides quantiques fortement corrélés pour des systèmes bidimensionnels est motivée par la grande quantité de résultats et de questions soulevées par l'étude de l'effet Hall quantique dans les gaz électroniques 2D. L'effet Hall quantique résulte de la quantification en niveaux de Landau sous un fort champ magnétique externe. Chaque niveau de Landau rempli est caractérisé par un invariant topologique appelé premier nombre de Chern. Lorsque des interactions sont présentes, des états incompressibles avec des remplissages partiels des niveaux de Landau apparaissent [3, 4]. Ces états de Hall quantiques fractionnaires présentent des excitations avec une charge fractionnaire et des modes de bord non triviaux. Les propriétés topologiques de l'effet Hall ont été généralisées aux systèmes appelés isolant de Chern, ou l'Effet Hall quantique anormal en l'absence de champ magnétique [5] et de même en présence d'interactions avec les isolants de Chern fractionnaires [6].

La simulation de ces effets à l'aide de réseaux de résonateurs supraconducteurs a été proposée théoriquement [7–10]. Les circuits supraconducteurs sont devenus l'une des plates-formes expérimentales les plus avancées pour la mise au point de systèmes quantiques artificiels, en particulier pour le traitement de l'information quantique sous le nom de circuit Quantum ElectroDynamics (cQED) [11–16]. Pour des systèmes sur réseaux, les excitations sont des photons micro-ondes ($f \simeq 6\,\mathrm{GHz}$) stockés dans des résonateurs supraconducteurs à haut facteur de qualité $Q \simeq 10^5$. Le couplage entre sites peut aller de quelques MHz à plusieurs centaines de MHz. L'intérêt principal de cette plate-forme est la possibilité d'atteindre le régime d'interaction forte en utilisant des jonctions de Josephson, qui sont des inductances non linéaires et non dissipatives. Le régime quantique est atteint pour des températures données par $k_B T \ll hf$, ce qui correspond à $T \ll 300\mathrm{mK}$. Température facilement

atteinte dans les réfrigérateurs à dilution commerciaux qui descendent à des températures de l'ordre de $T \simeq 10\,\mathrm{mK}$. Jusqu'à présent, les expériences sont loin de réaliser des réseaux 2D combinant à la fois une forte interaction photon-photon et une topologie non triviale [17, 18]. Il est donc naturel d'aborder d'abord séparément le contrôle de l'interaction et de la structure de la bande. En ce qui concerne les interactions, des expériences récentes ont démontré que le régime d'interaction forte peut être atteint dans des chaînes de résonateurs 1D [19, 20], mais pour l'instant, ces expériences sont limitées à des systèmes de de 20 résonateurs.

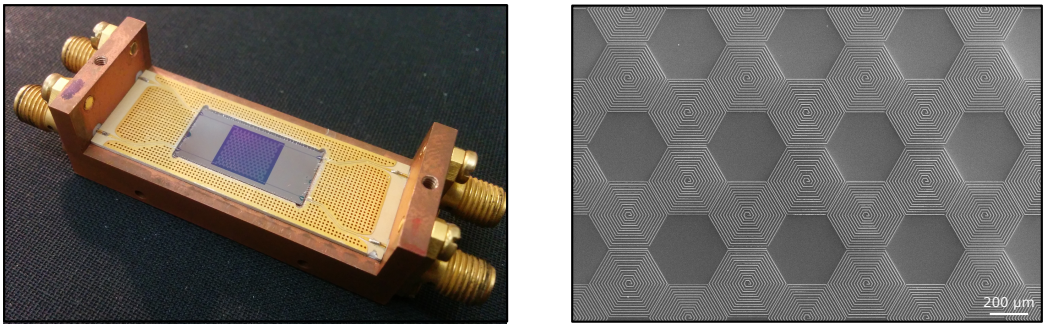

Figure 5: Réseau en nid d'abeilles de résonateurs supraconducteurs en forme de spirale. L'image de gauche montre l'échantillon installé dans son support. L'image de droite est une image du réseau prise au microscope électronique.

Le second axe de recherche, la réalisation de structures de bandes topologique pour les photons, rejoint le domaine en pleine croissance des réseaux photoniques [21–23]. L'une des principales motivations dans ce domaine est de mettre en avant les propriétés topologiques de réseaux qui ont été historiquement découverts en physique de la matière condensée [5, 24–27]. Une raison importante de cet intérêt est la réalisation de canaux de propagation topologiquement protégés qui apparaissent à l'interface entre deux matériaux avec des invariants topologiques différents [28–32]. La mise en évidence de ces états topologiquement protégés constitue un graal qui nécessite la réalisation techniquement difficile d'un réseau brisant la symétrie par renversement du temps. Des expériences dans ce sens ont été réalisées dans le domaine optique en utilisant des guides d'ondes couplés [33, 34], des résonateurs en anneau couplés [35, 36], dans le domaine micro-ondes [37, 38] et dans le domaine des radiofréquences avec circuits discrets [39]. Cependant, il est encore possible d'observer des effets topologiques dans des réseaux en préservant la symétrie par renversement du temps. C'est l'un des principaux objectifs de cette thèse. Le système le plus emblématique est sans aucun doute le réseau en nid d'abeille et ses cônes Dirac. Ce réseau a déjà été réalisé et étudié avec plusieurs types de plateformes : dans des réseaux microcavités semi-conductrices [40–42], de résonateurs diélectriques [43, 44], des canettes de soda [45], des gaz bidimensionnels d'électron [46], de guides d'ondes [47–49] des puits quantiques GaAs [50], des billards supraconducteurs pour micro-ondes [51].

Dans cette thèse, nous avons décidé de nous concentrer sur la réalisation de larges réseaux par opposition à ce qui avait été réalisé jusqu'à présent avec les circuits supraconducteurs. Les résonateurs supraconducteurs n'avaient pas encore été utilisés pour réaliser ce type d'expérience et nous devions d'abord répondre à des questions simples : est-il possible de concevoir un réseau de résonateurs supraconducteurs pour simuler tout modèle de liaisons fortes ? Si oui, existe-t-il une architecture optimale pour contrôler le terme de saut de ce

modèle ? Est-ce que les techniques de fabrication permettent de réaliser ces réseaux sans introduire trop de désordre ? Pour répondre à ces questions, nous avons décidé de concentrer nos efforts sur le réseau en nid d'abeilles en raison de ses propriétés topologiques et nous avons réalisé une première série d'expériences pour caractériser ce réseau (voir figure 5). Une part importante du travail expérimental a été la réalisation d'un dispositif d'imagerie de mode avec un laser qui nous a permis de mesurer la distribution spatiale des modes résonnants du réseau (voir figure 6). Cette technique est similaire à la microscopie à balayage laser développée pour observer la densité de courant dans les films supraconducteurs [52–54]. En analysant la transformée de Fourier de ces images, il est possible de remonter au vecteur d'onde de ces modes et de reconstruire la relation de dispersion dans la première zone de Brillouin et de la comparer à nos calculs *ab initio* (voir figure 7).

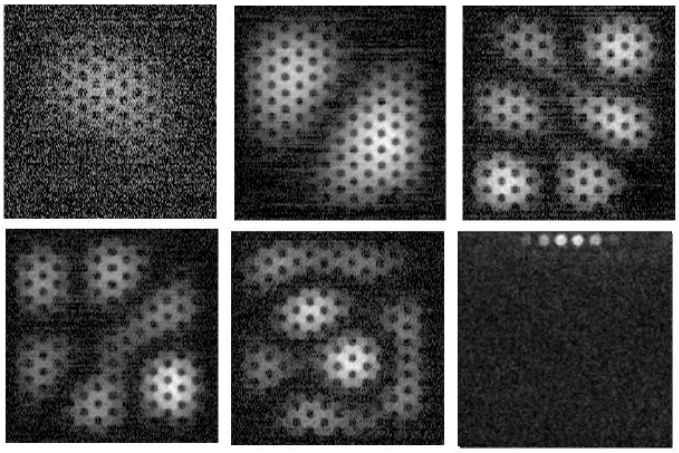

Figure 6: Distribution spatiale de certains modes résonnants observés dans un réseau en nid d'abeilles de résonateurs supraconducteurs. L'échantillon correspond à **HoneycombSi**. Le niveau de gris de l'image est proportionnel à l'énergie micro-onde locale stocké par les résonateurs.

Le bon accord entre nos données et nos modèles nous a permis d'envisager une expérience plus avancée pour observer des états de bordure topologique appelés états de Semenoff. La structure de bandes du réseau en nid d'abeilles est composée de deux bandes qui se touchent aux points Dirac. En introduisant un déséquilibre énergétique in situ entre les deux sites inéquivalents du réseau, une bande interdite s'ouvre aux points Dirac. Semenoff a prédit qu'à l'interface entre deux réseaux avec un déséquilibre de masse opposé, des états de bord apparaissent qui traversent la bande interdite [55]. Nous avons réalisé une telle paroi de domaine entre deux réseaux en nid d'abeilles de résonateurs supraconducteurs avec un déséquilibre d'énergie sur site opposé. En utilisant la technique d'imagerie en mode (voir figure 8), nous avons reconstruit la relation de dispersion des états de bord. Ces différentes expériences sont détaillées dans le manuscrit en suivant le plan exposé ci-dessous :

Le chapitre 1 présente les deux modèles réalisés dans cette thèse. La première partie donne la structure en bande du réseau en nid d'abeilles et montre les effets des voisins les plus proches sur la densité d'états (DOS). Nous utilisons ensuite un argument basé sur l'approximation de basse énergie pour expliquer l'existence d'états de bord pour des terminaisons zigzag et bearded, mais l'absence d'états de bords sur les terminaisons en armchair du réseau en nid

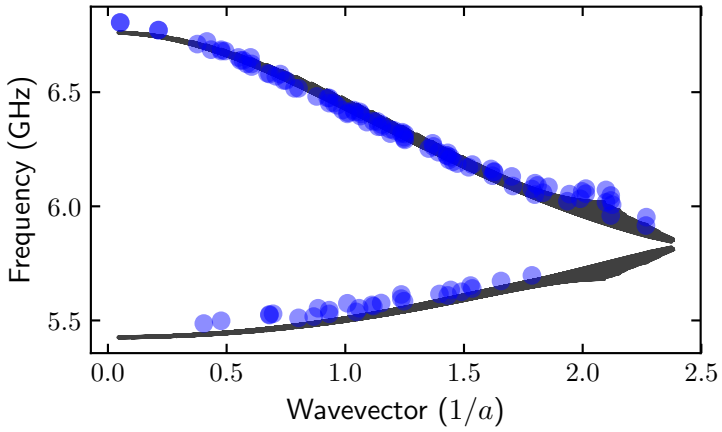

Figure 7: Relation de dispersion des modes résonnants d'un réseau en nid d'abeilles de résonateurs supraconducteurs. Les données expérimentales proviennent de la mesure de **ZigzagSi**. Ils sont en bon accord avec les prédictions d'un modèle ab initio du réseau.

d'abeilles. Nous analysons plus en détails ces états de bord à l'aide d'un modèle de liaisons fortes pour les caractériser (relation de dispersion, longueur de pénétration,...). La deuxième partie de ce chapitre est consacrée à l'isolant de Semenoff. Nous dérivons sa structure en bande en utilisant un modèle de liaison forte et nous dérivons l'existence d'états de bord le long de l'interface entre les deux isolants de Semenoff avec un modèle de basse énergie [55].

Le chapitre 2 présente les résonateurs supraconducteurs en spirale utilisés lors de cette thèse et comment concevoir un réseau en utilisant un logiciel de simulation électromagnétique (EM). Nous caractérisons le résonateur en spirale que nous avons utilisé pour tous nos réseaux. Nous montrons ensuite comment calculer le couplage entre deux résonateurs en spirale. Nous développons ensuite deux modèles pour caractériser les résonateurs électromagnétiques. Le premier modèle est basé sur la matrice d'admittance que nous appellerons *modèle d'admittance*. Nous présentons ensuite comment calculer la structure de bande du réseau en ne simulant que quelques sites du réseau. Le second modèle est basé sur une théorie des modes couplés (CMT). Nous appellerons ce modèle *CMT model*. Nous utilisons la théorie des modes couplés pour caractériser le couplage entre résonateurs et l'étendre à un système périodique. Cette approche utilise les équations de Maxwell pour calculer directement les fréquences de résonance à partir des intégrales de recouvrement associées aux couplages magnétiques et électriques.

Le chapitre 3 explique le fonctionnement de la technique de microscopie à balayage laser (LSM). Cette technique expérimentale permet de sonder la distribution spatiale des modes d'un réseau de résonateurs supraconducteurs. Cette mesure correspond à la mesure de l'énergie stockée dans les résonateurs et permet donc de donner la dépendance spatiale du mode électromagnétique correspondant.

Le chapitre 4 est consacré à la conception et à l'étude de l'échantillon **HoneycombSi** correspondant au réseau en nid d'abeille sur un substrat de silicium. Nous présentons le design de l'échantillon et ses propriétés. Nous présentons ensuite les modes mesurés avec l'imagerie de mode laser. Cette imagerie nous donne accès à la valeur du poids des modes. Pour récupérer le signe relatif de chaque site, nous avons conçu un algorithme qui, par une

méthode d'optimisation permet de reconstruire ce signe. Grâce à l'imagerie de mode, nous pouvons indexer les modes **i.e.** déterminer le vecteur d'onde (k_x, k_y) associé à la fréquence de résonnance. Cette indexation nous permet de reconstituer la structure en bande du réseau en nid d'abeilles. Cette structure de bande est comparée au *modèle admittance* et au *modèle CMT* présentés dans chapter 2 ainsi qu'à un modèle phénoménologique déduit de la DOS. Enfin, nous présentons l'étude des modes zigzag et bearded du réseau en nid d'abeilles en présentant leur structure en bande 1D et leur longueur de pénétration.

Le chapitre 5 présente la conception et la caractérisation des états de bord de Semenoff présentés dans le chapitre 1. Nous avons réalisé deux designs avec une interface entre les deux isolants de Semenoff différents. Ces designs nous ont permis de fabriquer et de mesurer plusieurs échantillons : **ZigzagSi**, **ArmchairSi**, **ZigzagSa** où zigzag/armchair correspond au type d'interface et Si/Sa au matériau du substrat (silicium ou saphir). Comme pour l'échantillon **HoneycombSi**, nous avons pu reconstruire la structure de bande de ces échantillons et la comparer aux modèles théoriques. Nous montrons ensuite que les états de bords de Semenoff sont localisés à l'interface entre les deux isolants. L'observation des états de bord est le résultat principal de cette thèse. Ces modes sont ensuite caractérisés expérimentalement par leur structure de bande ainsi que leurs longueurs de pénétrations. Finalement, ces échantillons nous ont aussi permis d'étudier le désordre en examinant la présence d'état localisés induits par des sites vacants dans l'échantillon **ZigzagSi**.

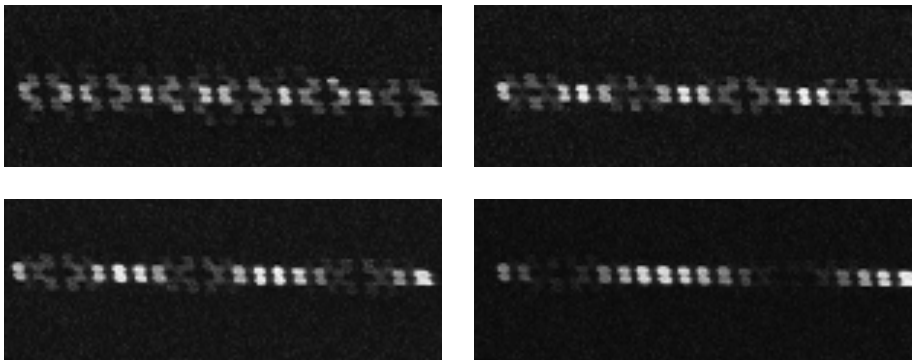

Figure 8: Images expérimentales d'états de bords de Semenoff localisés à l'interface entre deux réseaux en nid d'abeilles différents. L'existence de ces états est due aux différentes propriétés topologiques des deux réseaux de part et d'autre de l'interface.

Chapter 1

Properties of the honeycomb lattice and Semenoff insulators

Contents

The honeycomb lattice is one of the simplest example of a system that exhibits topological properties [56]. The band structure includes two Dirac cones around which the phase of the wavefunction winds in opposite directions. Because of these properties, the honeycomb lattice has been implemented as an artificial lattice in various experiments [42–44, 46, 57–61]. The experiments reported in this thesis use superconducting circuits to realize a honeycomb lattice for microwave photons. In particular, we have realized a variant of the honeycomb lattice with staggered onsite energies similar to boron nitride, which was considered by Semenoff [62] and is therefore named a Semenoff insulator. In this chapter, we first review the band structure and the density of state (DOS) of the honeycomb lattice with nearest-neighbor (NN) hopping. To take into account the long range coupling that appears in our superconducting lattices, we also present the effect of next-nearest neighbor (NNN) coupling on the band structure and DOS. In particular, we show that using the methodology developed by Bellec et al. [44], it is possible to extract the NN and the NNN couplings by locating a few points of interest in the DOS. We then show that for the zigzag and the bearded edges of a finite honeycomb lattice, edge states with a flat band structure appear. We derive the band structure of these modes with a Dirac equation formalism and with a tight-binding formalism.

The second part of this chapter analyses the Semenoff insulator [62]. We first extend the method presented in the first part to obtain the parameters of the tight-binding model. The Semenoff insulator possesses topological valley charges at the Dirac points. This topological property induces topological edge states when two Semenoff insulators with opposite mass are placed one next to another [55]. In the last part of this chapter, we review the proof of existence of these edges states using an effective low energy model. We then derive their band structure and their penetration length for two geometries of the domain wall.

1.1 Honeycomb lattice

In this section, we briefly review the tight-binding model of the honeycomb lattice and derive its band structure and DOS. As superconducting circuits have non-negligible long range coupling, we derive the effects of NNN hopping on the DOS and band structure. Following [44], we show how the identification of five points of interest in the DOS allows one to estimate an effective tight-binding model from a measured DOS.

1.1.1 Band structure

The honeycomb lattice is the superposition of two offset triangular sublattices respectively denoted A and B shown in red and blue in figure 1.1. The unit cell consists of two sites, one from the A sublattice, one from the B sublattice. The full lattice is spanned by the vectors of the Bravais lattice $\boldsymbol{a}_1 = \frac{a}{2}\left(\sqrt{3}, 3\right)$ and $\boldsymbol{a}_2 = \frac{a}{2}\left(-\sqrt{3}, 3\right)$ where a is the distance between two sites. We also define $\boldsymbol{a}_3 = \boldsymbol{a}_1 - \boldsymbol{a}_2$ for future use. A site of one sublattice is surrounded by three sites from the other sublattice. We denote by s_i for $i \in \{1, 2, 3\}$ the vectors that connect a A-site to its three nearest B-site neighbors. The NN tight-binding Hamiltonian is:

$$\mathcal{H} = t \sum_{\mathbf{r}} \sum_{i=1}^{3} c_B^\dagger(\mathbf{r} + \boldsymbol{s}_i) c_A(\mathbf{r}) + \text{H.c.} \tag{1.1.1}$$

where we have set $\hbar = 1$ and t is the NN hopping amplitude. The position $\mathbf{r}$ runs over all cells of the lattice and $c_\alpha^\dagger(\mathbf{r})$ creates an excitation on site $\mathbf{r}$ with α denoting the sublattice

$\alpha = A/B$.

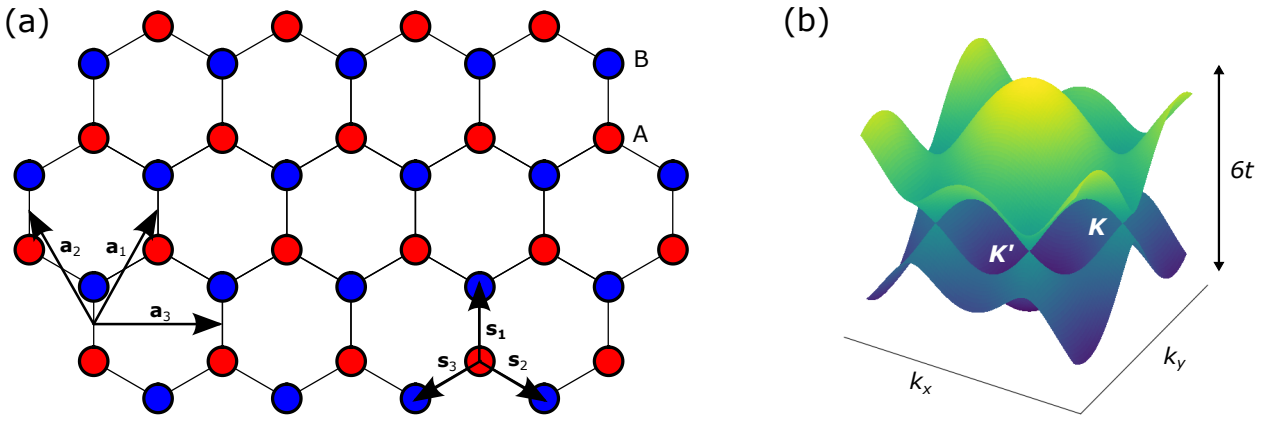

Figure 1.1: (a) Honeycomb lattice: $\boldsymbol{a}_1$ and $\boldsymbol{a_2}$ are the two primitive vectors. The vectors $\boldsymbol{s}_i$ for $i \in \{1, 2, 3\}$ are the nearest neighbor hopping vectors. The two sublattices are colored differently: the sublattice A in red and the sublattice B in blue. (b) Band structure of the honeycomb lattice. The two bands are symmetric and have a width of $3t$. They touch at the Dirac points $\boldsymbol{K}$ and $\boldsymbol{K'}$.

To find the energy band structure, we introduce the Fourier transform of the $c_\alpha(\mathbf{r})$ operators for each sublattice $\alpha = A, B$:

$$c_\alpha(\mathbf{r}_\alpha) = \frac{1}{\sqrt{N}} \sum_{\mathbf{k}\in \mathrm{BZ}} e^{-i\mathbf{k}\mathbf{r}_\alpha} c_\alpha(\mathbf{k}) \tag{1.1.2}$$

where the sum over $\mathbf{k}$ runs over the first Brillouin zone and N is the total number of sites. After substitution in equation (1.1.1), the Hamiltonian takes the form:

$$\mathcal{H} = \sum_{\mathbf{k}} \psi^\dagger_{\mathbf{k}} \mathcal{H}(\mathbf{k}) \psi_{\mathbf{k}} \quad \text{with} \quad \psi^\dagger_{\mathbf{k}} = \begin{bmatrix} c^\dagger_A(\mathbf{k}) & c^\dagger_B(\mathbf{k}) \end{bmatrix}. \tag{1.1.3}$$

We have introduced the two component spinor $\psi_{\mathbf{k}}$ and the Bloch Hamiltonian $\mathcal{H}(\mathbf{k})$:

$$\mathcal{H}(\mathbf{k}) = \begin{bmatrix} 0 & f_1(\mathbf{k}) \\ f_1^*(\mathbf{k}) & 0 \end{bmatrix} \quad \text{with} \quad f_1(\mathbf{k}) = t(1 + e^{i\mathbf{k}\cdot\boldsymbol{a}_1} + e^{i\mathbf{k}\cdot\boldsymbol{a}_2}) \tag{1.1.4}$$

The band structure is obtained by diagonalizing $\mathcal{H}(\mathbf{k})$ whose eigenvalues are:

$$\varepsilon_\pm(\mathbf{k}) = \pm|f_1(\mathbf{k})| = \pm t\sqrt{3 + 2\sum_{i=1}^{3} \cos \mathbf{k}\cdot\boldsymbol{a}_i}. \tag{1.1.5}$$

This band structure is represented in figure 1.1(b). It displays two bands, the valence and the conductance band. The two bands are symmetric with respect to the zero energy plane (particle-hole symmetry). A noticeable feature is the presence of Dirac points where the two bands touch. Theses points are solutions of the equation $\varepsilon(\mathbf{k}) = 0$. Solving it in the first Brillouin zone gives two inequivalent Dirac points positioned at:

$$\mathbf{k} = \pm\boldsymbol{K} = \left(\pm\frac{4\pi}{3\sqrt{3}a}, 0\right) \tag{1.1.6}$$

The others Dirac points can be linked by a reciprocal lattice vector to one of theses two points, and therefore describe the same physical state. The existence of these two Dirac points is topologically protected by sublattice inversion and time-reversal symmetry [56].

1.1.2 Density of state (DOS)

The DOS $D(E)$ counts the number of states per energy per unit cell. In order to compute the DOS, we calculate the imaginary part of the retarded green function $G(E,k)$ (or resolvent) in the eigenbasis of the tight-binding model [63]:

$$D(E) = -\frac{1}{\pi}\sum_{\mathbf{k}} \mathrm{Im}G(\mathbf{k},E) \quad \text{with} \quad G(\mathbf{k},E) = \sum_{j=\pm}\frac{1}{E-\varepsilon_j(\mathbf{k})+i\gamma} \tag{1.1.7}$$

with γ being a loss rate. The DOS of the honeycomb lattice is shown in figure 1.2.

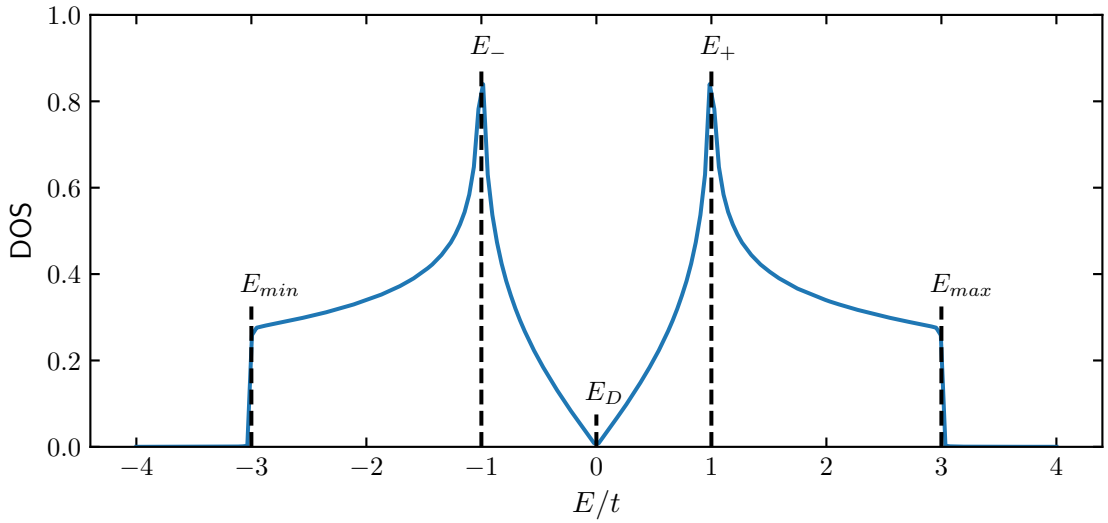

Figure 1.2: DOS of the honeycomb lattice with NN coupling $t = 1$. Five remarkable points appear in this DOS: the two extema $E_{\min}$, $E_{\max}$ of the band structure, the Dirac point at $E(\mathbf{k}) = 0$ where the density of states vanishes and two logarithmic divergences E_+, E_- due to saddle point in the dispersion relation.

Like the band structure, the DOS is symmetric with respect to $E = 0$. Five particular points can be identified as shown in the figure 1.2.

1.1.3 Role of the 2nd and 3rd nearest neighbor coupling

In our experimental realization of the honeycomb lattice, long range couplings naturally appear leading to an asymmetry of the two bands and to a shift of the points of interest. The Bloch Hamiltonian with 2nd (t_2) and 3rd (t_3) NN hopping terms is:

$$\mathcal{H}(\mathbf{k}) = \begin{bmatrix} f_2(\mathbf{k}) & f_1(\mathbf{k})+f_3(\mathbf{k}) \\ f_1^*(\mathbf{k})+f_3^*(\mathbf{k}) & f_2(\mathbf{k}) \end{bmatrix} \tag{1.1.8}$$

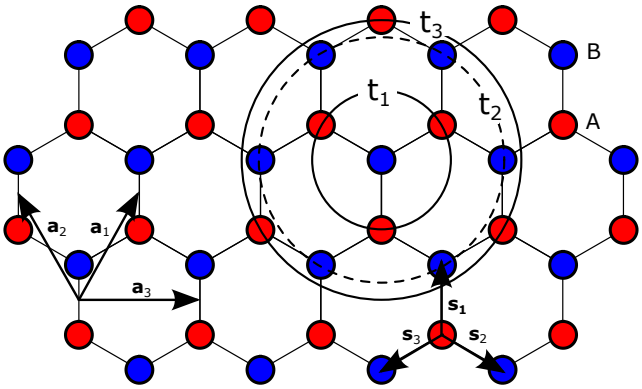

Figure 1.3: 2nd and 3rd NN hopping terms in the honeycomb lattice. The t_2 hopping couples sites of the same sublattice whereas t_3 couples sites from different sublattices.

where the link functions associated to each coupling in the Hamiltonian are:

$$f_1(\mathbf{k}) = t_1(1 + e^{i\mathbf{k}\cdot\boldsymbol{a}_1} + e^{i\mathbf{k}\cdot\boldsymbol{a}_2}) \tag{1.1.9}$$

$$f_2(\mathbf{k}) = 2t_2(\cos\mathbf{k}\cdot\boldsymbol{a}_1 + \cos\mathbf{k}\cdot\boldsymbol{a}_2 + \cos\mathbf{k}\cdot(\boldsymbol{a}_1 - \boldsymbol{a}_2)) \tag{1.1.10}$$

$$f_3(\mathbf{k}) = t_3(e^{i\mathbf{k}\cdot(\boldsymbol{a}_1+\boldsymbol{a}_2)} + e^{i\mathbf{k}\cdot(\boldsymbol{a}_1-\boldsymbol{a}_2)} + e^{i\mathbf{k}\cdot(\boldsymbol{a}_2-\boldsymbol{a}_1)}) \tag{1.1.11}$$

The band structure is then given by:

$$\varepsilon_\pm(\mathbf{k}) = f_2(\mathbf{k}) \pm |f_1(\mathbf{k}) + f_3(\mathbf{k})| \tag{1.1.12}$$

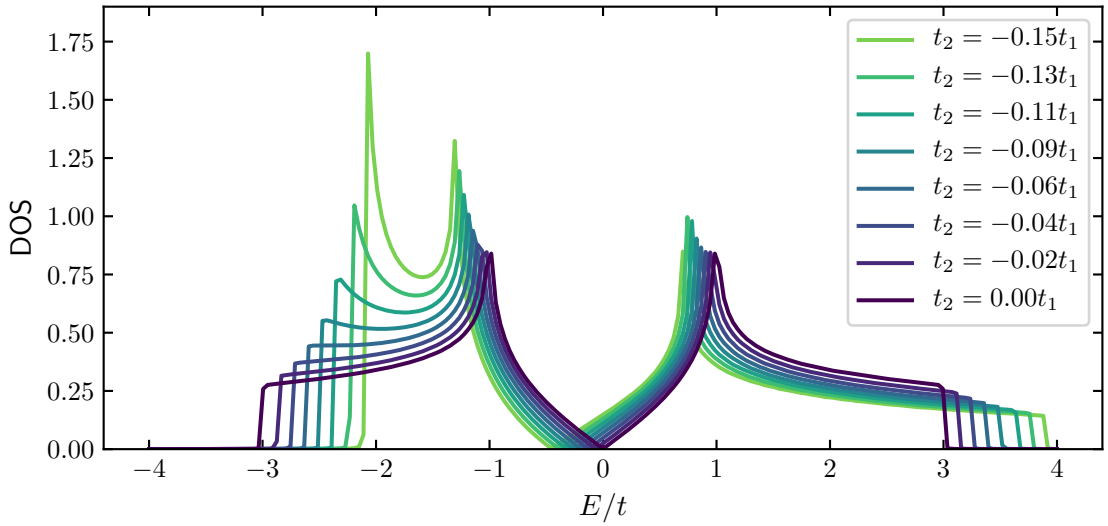

Figure 1.4: Density of state (DOS) of graphene with t_2 ranging from 0 to $-0.15t$. As t_2 becomes larger, the two bands become asymmetric. For large t_2, a Van Hove singularity appears at the lower band edge.

The figure 1.4 shows the evolution of the DOS with increasing t_2 and $t_3 = 0$. If t_2 has an opposite sign to t_1, the upper band is larger than the lower band. If they have the same sign,

the lower band is larger than the upper band. In order to quantify the importance of t_2 given an experimentally measured DOS, one can identify special points in the measured DOS and deduce t_1, t_2 and t_3 as shown in Bellec et al. [44]. The upper and the lower boundaries of the spectrum obtained when $\mathbf{k}\cdot\boldsymbol{a}_1 = \mathbf{k}\cdot\boldsymbol{a}_2 = 0$ are:

$$E_{\min} = 6t_2 - 3|t_1 + t_3| \tag{1.1.13}$$
$$E_{\max} = 6t_2 + 3|t_1 + t_3| \tag{1.1.14}$$

The two extremal points of the gap that are located at the two Dirac points ($\boldsymbol{K}\cdot\boldsymbol{a}_1 = \pm 2\pi/3$ and $\boldsymbol{K}\cdot\boldsymbol{a}_2 = \pm 2\pi/3$) become:

$$E_D = -3t_2 \tag{1.1.15}$$

Finally, the two logarithmic divergences corresponding to saddle points in the band structure are located at $\mathbf{k}\cdot\boldsymbol{a}_1 = \mathbf{k}\cdot\boldsymbol{a}_2 = \pi$ with energies:

$$E_- = -2t_2 - |t_1 - 3t_3| \tag{1.1.16}$$
$$E_+ = -2t_2 + |t_1 - 3t_3| \tag{1.1.17}$$

Since a model with 3$^{\text{rd}}$ NN hopping have 3 parameters t_1, t_2, t_3 plus a global offset f_0 and there are 5 points of interest, it is possible to estimate these parameters from the point of interest energies by inverting equations (1.1.13) – (1.1.17).

1.2 Zigzag and bearded edge states

A consequence of the winding of the phase of the wavefunction near the Dirac points is the existence of edge states on some edges of a finite size honeycomb lattice. It has been shown [31, 64, 65] that the existence of edge states on a specific boundary is related to a non-zero Berry phase defined by a path in the reciprocal space. These states have been observed in artificial systems [40, 48] and in particular in the microwave domain [43, 66]. In this section, we review the proof of existence of edge states on a zigzag and a bearded boundary as well as their non-existence on the armchair boundary using a Dirac equation approach. We then derive the band structure and the penetration length of the edge states with a tight-binding approach to finally show some results when NNN hopping is included.

1.2.1 Low energy analysis near the Dirac points

To understand the existence of edge states, we use a low energy approach near the Dirac point [56, 67, 68]. We expand the wavevector near the Dirac points $\mathbf{k} = \xi\boldsymbol{K} + \mathbf{q}$ where $\xi = \pm 1$ is the valley isospin and $\mathbf{q}$ a small deviation from the Dirac point ($|\mathbf{q}|a \ll 1$). Expanding the Hamiltonian in the Bloch representation gives:

$$\mathcal{H}^{\xi}(\mathbf{q}) \simeq \begin{bmatrix} 0 & \frac{3at}{2}(\xi q_x - iq_y) \\ \frac{3at}{2}(\xi q_x + iq_y) & 0 \end{bmatrix} = \mu\sigma_z + v_F(\xi q_x\sigma_x + q_y\sigma_y) \tag{1.2.1}$$

where the Fermi velocity is $v_F = 3ta/2$ and σ_i are the Pauli matrices. The energy dispersion of the low energy Hamiltonian reads:

$$\varepsilon^{\xi}(\mathbf{q}) = \pm v_F|\mathbf{q}| \tag{1.2.2}$$

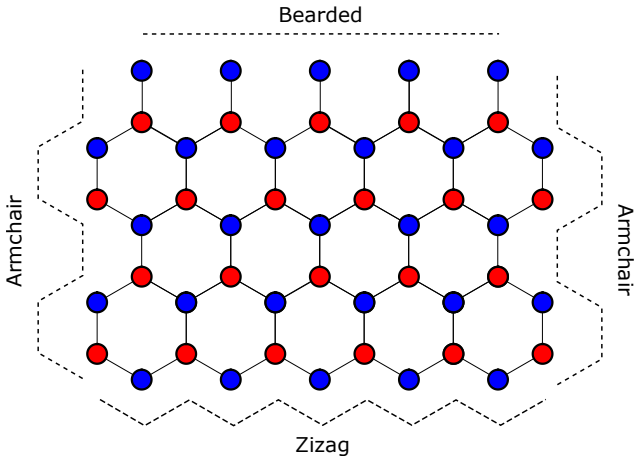

Figure 1.5: Different edges for a finite size lattice. Zigzag, bearded and armchair edges are represented. Without anisotropy, the armchair has no edge states whereas exponentially localized states are present at the zigzag and bearded edges.

This band structure is independent of the valley isospin ξ, so there is a twofold valley degeneracy. It is possible to concatenate the two valleys by defining a four component spinor where the first two components describe the valley at $+\boldsymbol{K}$ and the last two the valley at $-\boldsymbol{K}$ but with the two sublattices at inverted positions:

$$\Psi_{\mathbf{q}} = \begin{bmatrix} \psi^{+}_{\mathbf{q},A} \\ \psi^{+}_{\mathbf{q},B} \\ \psi^{-}_{\mathbf{q},B} \\ \psi^{-}_{\mathbf{q},A} \end{bmatrix} \tag{1.2.3}$$

The effective low energy Hamiltonian is then:

$$\mathcal{H}(\mathbf{q}) = v_F \tau_z \otimes \mathbf{q} \cdot \boldsymbol{\sigma} \tag{1.2.4}$$

where the Pauli matrix τ_z applies to the valley isospin and the Pauli matrices σ to the sublattice isospin. In real space, the Hamiltonian is obtained by substituting $\boldsymbol{q} \to -i\nabla$.

Zigzag edge

We consider a semi-infinite honeycomb lattice with a zigzag boundary at $y = 0$. The half plane $y > 0$ is occupied by the honeycomb lattice whereas the half plane $y < 0$ is empty. We look for solutions of the Schrödinger equation with a wavefunction $\Psi(\mathbf{r}) = e^{iq_x x}\Psi(y)$. The wavefunction must satisfy:

$$v_F \left(-i\tau_z \otimes \sigma_y \frac{\mathrm{d}}{\mathrm{d}y} + q_x \tau_z \otimes \sigma_x \right) \psi(y) = E\psi(y) \tag{1.2.5}$$

Multiplying this equation by $\tau_z \otimes \left(-i\sigma_y \frac{\mathrm{d}}{\mathrm{d}y} + q_x \sigma_x \right)$ yields the uncoupled equations:

$$\left(-\frac{\mathrm{d}^2}{\mathrm{d}y^2} + q_x^2 \right) \psi(y) = \left(\frac{E}{v_F} \right)^2 \psi(y) \tag{1.2.6}$$

For a solution localized near $y = 0$, we require that $|\psi(y)|^2 \to 0$ when $x \to \infty$. Localized solutions exist only if $|E| < v_F|q_x|$ and are of the form:

$$\psi(y) = \exp\left(-\frac{y}{2\xi(q_x)}\right)\begin{bmatrix}A_1\\B_1\\B_2\\A_2\end{bmatrix} \quad \text{with} \quad \xi^{-1}(q_x) = \frac{2}{v_F}\sqrt{v_F^2q_x^2 - E^2} \tag{1.2.7}$$

with A_1, A_2, B_1, B_2 being integration constants. The amplitude of the mode on the two lattices is:

$$\begin{bmatrix}\Psi_A(\mathbf{r})\\\Psi_B(\mathbf{r})\end{bmatrix} = e^{iq_xx}e^{-\frac{y}{2\xi(q_x)}}\begin{bmatrix}A_1e^{i\boldsymbol{K}\cdot\mathbf{r}} + A_2e^{i\boldsymbol{K'}\cdot\mathbf{r}}\\B_1e^{i\boldsymbol{K}\cdot\mathbf{r}} + B_2e^{i\boldsymbol{K'}\cdot\mathbf{r}}\end{bmatrix} \tag{1.2.8}$$

We can now implement the boundary condition. For the zigzag edge, the condition is that the wave function on the B sublattice cancels, $\Psi_B(y = 0) = 0$ for all x. This yields the solution $B_1 = B_2 = 0$. Injecting this solution in (1.2.5), there exists non-trivial solutions if:

$$E = 0 \quad \text{and} \quad \sqrt{v_F^2q_x^2 - E^2} = \xi v_F q_x \tag{1.2.9}$$

This means that zigzag edge states have a flat dispersion $E(q_x) = 0$ and exist only for $q_x > 0$ in the $\boldsymbol{K}$ valley and for $q_x < 0$ in the $\boldsymbol{K'}$ valley. This analysis shows that, in the low energy approximation near the Dirac points, zigzag edges present an edge state branch with a flat band at zero energy $E = 0$. The edge states exist for wavevectors $k_xa \in \left[\frac{2\pi}{3\sqrt{3}}, \frac{4\pi}{3\sqrt{3}}\right]$ and their penetration length is given by:

$$E(q_x) = 0 \quad \text{and} \quad \xi(q_x) = \frac{1}{2v_F|q_x|} \tag{1.2.10}$$

Bearded edge

The boundary condition for the bearded edge is obtained by imposing $\Psi^A(y = 0) = 0$ leading to $A_1 = A_2 = 0$ and:

$$E = 0 \quad \text{and} \quad \sqrt{v_F^2q_x^2 - E^2} = -\xi v_F q_x \tag{1.2.11}$$

Thus there exists edge modes for $q_x < 0$ in the $\boldsymbol{K}$ valley and for $q_x > 0$ in the $\boldsymbol{K'}$ valley or for $k_x \in \left[-\frac{2\pi}{3\sqrt{3}}, \frac{2\pi}{3\sqrt{3}}\right]$. The band structure is also flat at $E = 0$ and the penetration length is the same as before (1.2.10).

Armchair edge

For the armchair case, we swap x and y in (1.2.6) and in (1.2.7). The boundary condition is $\Psi_A(x = 0) = \Psi_B(x = 0) = 0$:

$$0 = e^{iq_yy}\begin{bmatrix}A_1 + A_2\\B_1 + B_2\end{bmatrix} \tag{1.2.12}$$

We therefore obtain

$$A_1 + A_2 = 0 \quad \text{and} \quad B_1 + B_2 = 0 \tag{1.2.13}$$

Injecting this solution into (1.2.5) leads to:

$$\left(\frac{v_F}{2\xi} \pm v_F q_y\right) A_1 = \mp E B_1 \tag{1.2.14}$$

$$\left(\frac{v_F}{2\xi} \pm v_F q_y\right) B_1 = \pm E A_1 \tag{1.2.15}$$

whose only solution is the trivial null solution. However, introducing anisotropy between the three nearest neighbors couplings leads to the existence of edge states on armchair boundaries [66].

Figure 1.6 summarizes our results by showing the band structure of semi-infinite lattices for the three boundaries considered above.

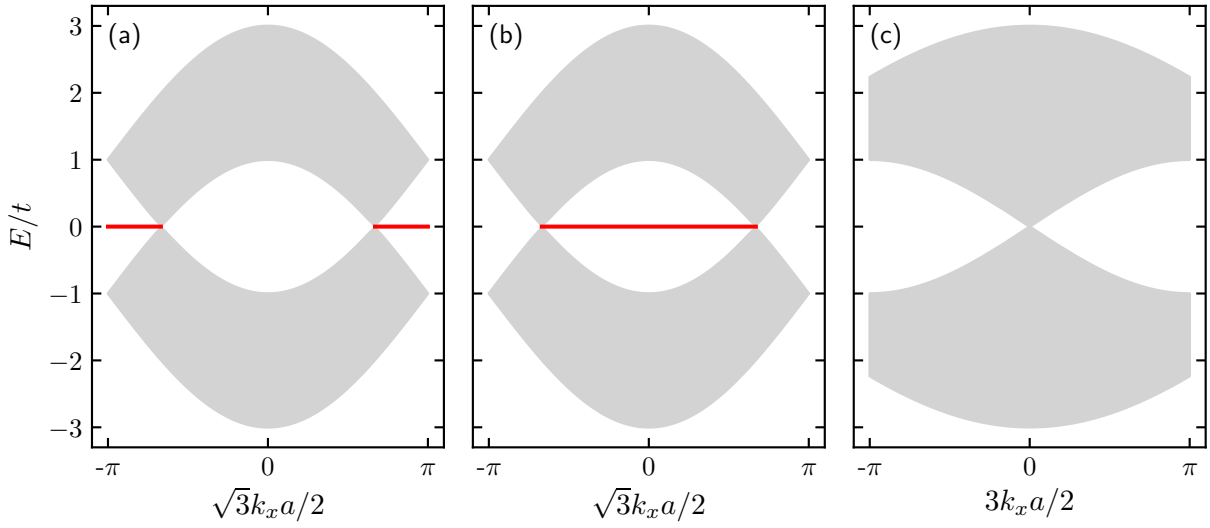

Figure 1.6: Band structure of semi-infinite honeycomb lattices with different free boundaries: (a) zigzag, (b) bearded, (c) armchair. The grey region corresponds to the bulk states and the red line to the edge states. No edge states appear in the armchair case, whereas zigzag and bearded boundaries host a flat band edge branch.

1.2.2 Tight-binding analysis

The previous analysis in continuous space is only valid near the Dirac points $\mathbf{k} = \boldsymbol{K}, \boldsymbol{K}'$. We now consider a tight-binding approach which is valid at all $\mathbf{k}$. As before, we look for solutions of the Hamiltonian (1.1.4) on a semi-infinite slab.

We first consider a semi-infinite honeycomb lattice with a zigzag edge at $y = 0$. We look for a solution localized on the edge as

$$\Psi = \lambda^{|n|} e^{ik_x x} \Phi(\lambda, k_x), \tag{1.2.16}$$

where n is the index of the unit cell starting from the edge, k_x the wavevector in the x direction and $\Phi(\lambda, k_x)$ the sublattice spinor. In order to be localized near the boundary

$y = 0$, we require that $|\lambda| < 1$. In the $y > 0$ half-plane, the Schrödinger equation for $\Phi(\lambda, k_x)$ reads:

$$\begin{bmatrix} E & -t - 2\lambda t \cos\left(\frac{\sqrt{3}}{2}k_x a\right) \\ -t - 2\lambda^{-1} t \cos\left(\frac{\sqrt{3}}{2}k_x a\right) & E \end{bmatrix} \begin{bmatrix} \Phi_1 \\ \Phi_2 \end{bmatrix} = 0 \tag{1.2.17}$$

which has non zero solutions if:

$$E^2 - t^2\left(1 + 4\cos^2\left(\frac{\sqrt{3}}{2}k_x a\right) + 2\cos\left(\frac{\sqrt{3}}{2}k_x a\right)\left(\lambda + \frac{1}{\lambda}\right)\right) = 0. \tag{1.2.18}$$

Two solutions are possible $\lambda = \mathcal{V} \pm \sqrt{\mathcal{V}^2 - 1}$ with:

$$\mathcal{V} = \left(\lambda + \frac{1}{\lambda}\right) = \frac{1}{2\cos\left(\frac{\sqrt{3}}{2}k_x a\right)}\left(\frac{E^2}{t^2} - 1 - 4\cos^2\left(\frac{\sqrt{3}}{2}k_x a\right)\right) \tag{1.2.19}$$

These solutions are associated with the eigenvectors:

$$\Phi \propto \begin{bmatrix} t + 2t\lambda \cos\left(\frac{\sqrt{3}}{2}k_x a\right) \\ E \end{bmatrix} \tag{1.2.20}$$

The zigzag boundary condition requires that $\Phi_B = 0$ leading to $E = 0$ and:

$$\lambda = -2\cos\left(\frac{\sqrt{3}}{2}k_x a\right) \quad \text{and} \quad \xi(k_x) = -\frac{1}{2|\log\left(2\cos\left(\frac{\sqrt{3}}{2}k_x a\right)\right)|} \tag{1.2.21}$$

As we require that $|\lambda| < 1$, the edge states exists only for $k_x a \in [\frac{2\pi}{3\sqrt{3}}, \frac{4\pi}{3\sqrt{3}}]$.

For the bearded edge, we impose $\Phi_A = 0$ and we obtain $E = 0$ and:

$$\lambda = -\frac{1}{2\cos\left(\frac{\sqrt{3}}{2}k_x a\right)} \quad \text{and} \quad \xi(k_x) = \frac{1}{2|\log\left(2\cos\left(\frac{\sqrt{3}}{2}k_x a\right)\right)|} \tag{1.2.22}$$

As we require that $|\lambda| < 1$, the bearded edge states exist only for $k_x a \in [-\frac{2\pi}{3\sqrt{3}}, \frac{2\pi}{3\sqrt{3}}]$. This tight-binding analysis confirms the low energy analysis and refines the prediction for the penetration length.

1.2.3 Effect of NNN hopping on edge states

The existence of edge states is governed by the position of the Dirac points in the Brillouin zone [65]. The t_2 and t_3 hopping terms change the energy of the Dirac point but do not displace them as they preserve sublattice inversion symmetry. Therefore, these hopping terms do not modify the argument for the existence of edge states (section 1.2.2). The only effect of NNN coupling is to give rise to dispersive edge state bands instead of flat bands (see figure 1.7).

1.3 Semenoff insulator

Without any additional degree of freedom (*e.g.* spin), there are only four possible mass terms [69] that generate gaps at the Dirac points. They are the Haldane mass [5], the

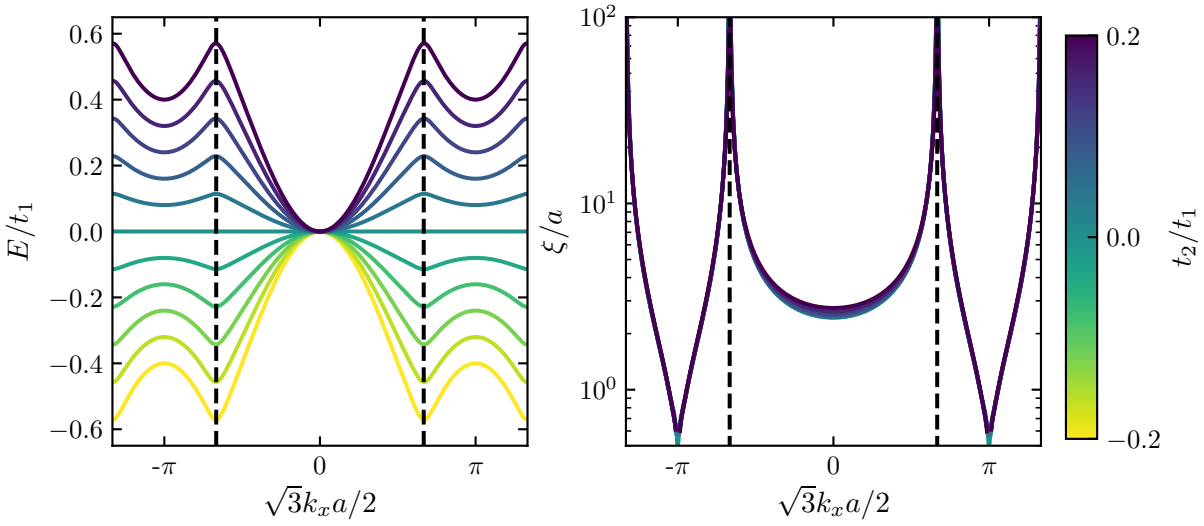

Figure 1.7: Band structure of the edge states of a ribbon with one zigzag and one bearded edge for different values of t_2. Increasing t_2 increases the width of the band but does not change the penetration length.

Semenoff mass [55] and the two Kekule distortions [70]. The Haldane mass does not break the lattice symmetry but breaks time reversal symmetry whereas the three other break sublattice symmetry without breaking the time reversal symmetry. The hexagonal boron-nitride is an example of non-zero Semenoff mass as the A and B sites are occupied by different atoms. In this section, we investigate the properties of such lattices with non-zero Semenoff mass, which are called Semenoff insulators. We first derive their band structure and their bulk properties. Then, using a low energy description, we describe their topological properties by calculating the Berry curvature near the Dirac points and show the existence of two opposites topological charges at the two Dirac points.

1.3.1 Band structure and DOS

The Semenoff insulator is a honeycomb lattice where the A and B sublattices are offset by an energy 2μ that breaks the sublattice inversion symmetry. The tight-binding Hamiltonian of the lattice reads:

$$\mathcal{H} = \left(t \sum_{\mathbf{r}} \sum_{i=1}^{3} c_B^\dagger(\mathbf{r} + \boldsymbol{s}_i) c_A(\mathbf{r}) + \text{H.c.} \right) + \mu \sum_{\mathbf{r}} c_A^\dagger(\mathbf{r}) c_A(\mathbf{r}) - \mu \sum_{\mathbf{r}} c_B^\dagger(\mathbf{r}) c_B(\mathbf{r}) \tag{1.3.1}$$

where we have used the same definitions as in (1.1.1) and μ is the Semenoff mass. In the Bloch representation, this Hamiltonian takes the form:

$$\mathcal{H}(\mathbf{k}) = \begin{bmatrix} \mu & f_1(\mathbf{k}) \\ f_1^*(\mathbf{k}) & -\mu \end{bmatrix} \quad \text{with} \quad f_1(\mathbf{k}) = t(1 + e^{i\mathbf{k}\cdot\boldsymbol{a}_1} + e^{i\mathbf{k}\cdot\boldsymbol{a}_2}), \tag{1.3.2}$$

which gives the band structure:

$$\varepsilon_{\pm}(\mathbf{k}) = \pm\sqrt{\mu^2 + |f_1(\mathbf{k})|^2} = \pm\sqrt{\mu^2 + t^2\left(3 + 2\sum_{i=1}^{3}\cos\mathbf{k}\cdot\boldsymbol{a}_i\right)} \tag{1.3.3}$$

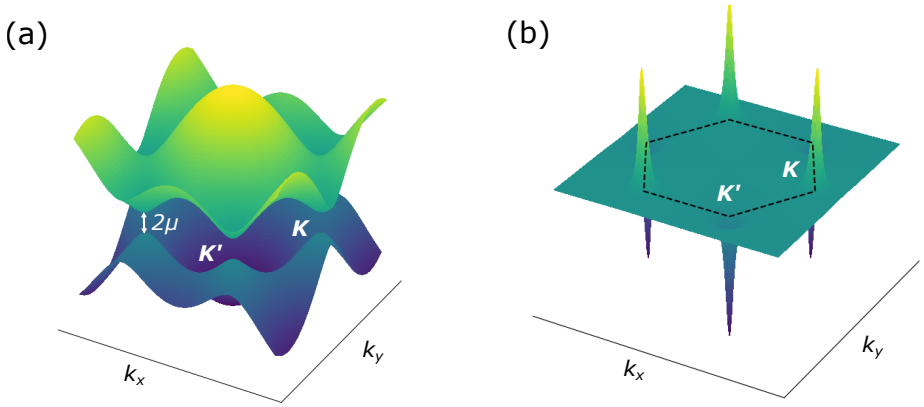

Figure 1.8: (a) Band structure of the Semenoff insulator for a Semenoff mass $\mu = 0.1t$. A gap of 2μ appears at the Dirac points $\boldsymbol{K}$ and $\boldsymbol{K}'$. (b) Berry curvature of the upper band for $\mu > 0$. The Berry curvature presents sharp peaks near the two Dirac points. The sign of the peak maximum depends on the Dirac points: here positive for $\boldsymbol{K}$ and negative for $\boldsymbol{K}'$.

In comparison to the honeycomb lattice, the Semenoff insulator is a bulk insulator with a gap 2μ at the Dirac points. The band structure is depicted in figure 1.8 and the DOS in figure 1.9.

1.3.2 Role of the 2nd and 3rd nearest neighbor coupling

The bulk properties of Semenoff insulators are modified by next-nearest neighbor coupling. The principal effect is to change the gap position and to distort the bands as in the case of the honeycomb lattice. The Hamiltonian of a Semenoff insulator with 2nd and 3rd nearest neighbor coupling is:

$$\mathcal{H}(\mathbf{k}) = \begin{bmatrix} f_2(\mathbf{k}) + \mu & f_1(\mathbf{k}) + f_3(\mathbf{k}) \\ f_1^*(\mathbf{k}) + f_3^*(\mathbf{k}) & f_2(\mathbf{k}) - \mu \end{bmatrix} \tag{1.3.4}$$

where f_i is the i-nth nearest neighbor contribution as in (1.1.11). The bulk energy spectrum is given by:

$$\varepsilon_{\pm}(\mathbf{k}) = f_2(\mathbf{k}) \pm \sqrt{\mu^2 + |f_1(\mathbf{k}) + f_3(\mathbf{k})|^2} \tag{1.3.5}$$

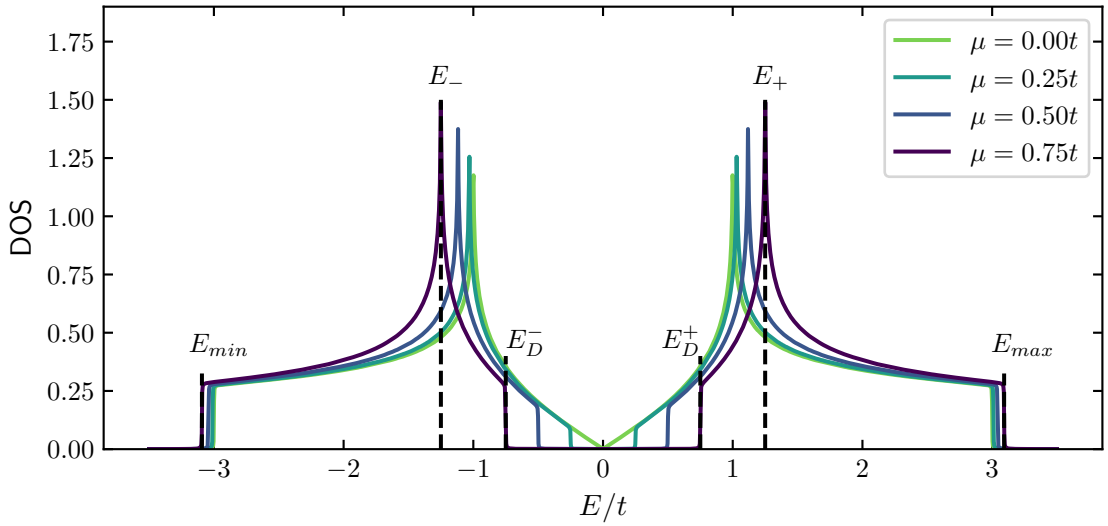

Figure 1.9: DOS of Semenoff insulators with Semenoff mass ranging from 0 to $0.75t$. The Dirac points split in two points marking the gap between the two bands. The points of interest are also shifted.

Following the notations of figure 1.3, we obtain the following energies for the 6 points of interest:

$$E_{\min} = 6t_2 - \sqrt{\mu^2 + 9(t_1 + t_3)^2} \tag{1.3.6}$$

$$E_{\max} = 6t_2 + \sqrt{\mu^2 + 9(t_1 + t_3)^2} \tag{1.3.7}$$

$$E_- = -2t_2 - \sqrt{\mu^2 + (t_1 - 3t_3)^2} \tag{1.3.8}$$

$$E_+ = -2t_2 + \sqrt{\mu^2 + (t_1 - 3t_3)^2} \tag{1.3.9}$$

$$E_D^- = -3t_2 - \mu \tag{1.3.10}$$

$$E_D^+ = -3t_2 + \mu \tag{1.3.11}$$

1.4 Edge modes between two Semenoff insulators: massive Dirac equation

When two Semenoff insulators with opposite Semenoff masses are set aside, edge states appear at the boundary as discovered by Semenoff et al. [55]. In this section, we first derive the low energy Hamiltonian from which the topological argument for the existence of the edge states follows.

1.4.1 Berry curvature of Semenoff insulators

In the previous section, we have seen numerically that the Berry curvature of the bands presents sharp peaks near the Dirac points. Here, we use the the low energy Dirac Hamiltonian to recover this property. Expanding the wavevector around the Dirac point, we obtain

$$\mathcal{H}(\mathbf{q}) = \mu\tau_z \otimes \sigma_z + v_F\tau_z \otimes \mathbf{q}\cdot\boldsymbol{\sigma} \tag{1.4.1}$$

with the same definition as in (1.2.3) for the four component spinor. The energy spectrum reads:

$$\varepsilon^{\xi}(\mathbf{q}) = \pm\sqrt{\mu^2 + v_F^2|\mathbf{q}|^2} \tag{1.4.2}$$

with $\xi = \pm 1$ the valley isospin. The associated Berry curvature is defined as:

$$\Omega(\mathbf{q}) = \xi\frac{\mu}{2\left(\mu^2 + v_F^2|\mathbf{q}|^2\right)^{3/2}} \tag{1.4.3}$$

It presents two sharp peaks centered at the two Dirac points [56, 71]. Each valleys carries a topological charge:

$$\mathcal{C}_\xi = \frac{1}{2\pi}\int \mathrm{d}^2\mathbf{q}\Omega(\mathbf{q}) = \frac{1}{2}\xi\mathrm{sign}(\mu) \tag{1.4.4}$$

Hence, for a given Semenoff mass μ, each valley has a topological charge $\mathcal{C}_\xi$. However, the total Chern invariant is zero ($\mathcal{C}_+ + \mathcal{C}_- = 0$) because of the time reversal symmetry of the system. The Semenoff insulator is a trivial insulator in the sense of Chern invariant but still possesses topological valley charges at each Dirac point.

1.4.2 Existence of edge states at domain walls

The sign of the Semenoff mass does not modify the band structure. However, it changes the sign of the topological valley charge (1.4.4). For the valley $\xi = +1$, the charge is $C_+ = 1/2$ for $\mu > 0$ whereas $C_+ = -1/2$ for $\mu < 0$. Let us construct a domain wall between two Semenoff insulators with opposite Semenoff masses. We consider a position dependent Semenoff mass $\mu(x)$ that changes sign at $x = 0$ and with the two limits:

$$\lim_{x\mapsto-\infty}\mu(x) = -\mu < 0 \quad \text{and} \quad \lim_{x\mapsto+\infty}\mu(x) = \mu > 0 \tag{1.4.5}$$

For $x > 0$, this system has a $\mathcal{C}_+ = 1/2$ (resp. $\mathcal{C}_- = -1/2$) and for $x < 0$, $\mathcal{C}_+ = -1/2$ (resp. $\mathcal{C}_- = 1/2$). This configuration leads to the existence of $\mathcal{C}_+(x > 0) - \mathcal{C}_+(x < 0) = 1$ edge state branch for the + valley as well as one edge branch for the other valley [71]. We now derive

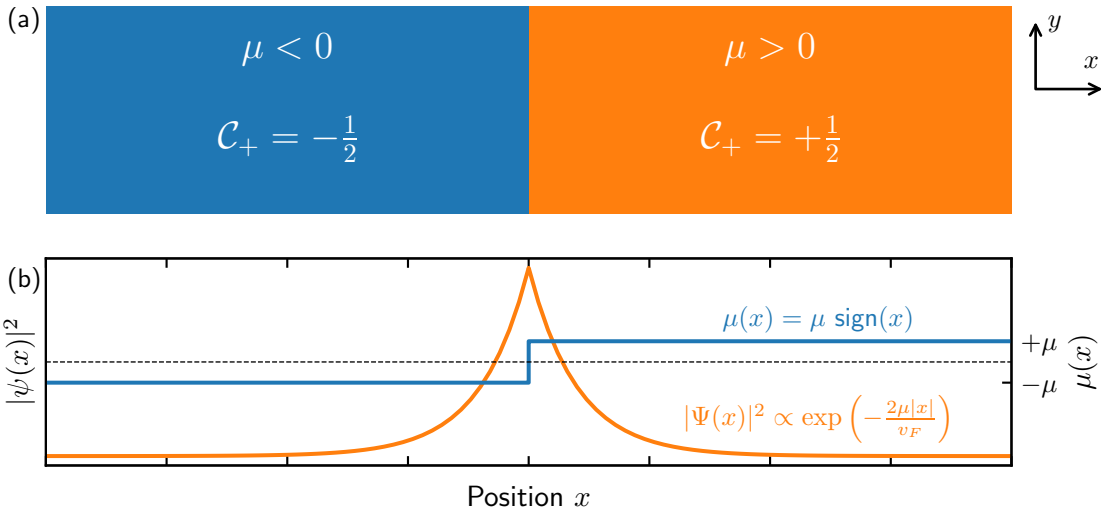

Figure 1.10: (a) Kink in the Semenoff mass: on each side there is a Semenoff insulator with a sign difference between the mass on the right and on the left side. The topological valley charge $\mathcal{C}_+$ changes sign from one side to the other. There is always a twofold degenerate zero energy bound state localized near the domain wall. (b) Edge state profiles showing their exponential decay.

these branches by looking for solutions of the Schrödinger equation with a wavefunction of the form $\Psi(\mathbf{r}) = e^{iqy}\psi(x)$. The Schrödinger equation for $\psi(x)$ reads:

$$\left(-iv_F\tau_z \otimes \sigma_x \frac{\mathrm{d}}{\mathrm{d}x} + v_F q \tau_z \otimes \sigma_y + \mu(x)\tau_z \otimes \sigma_z\right)\psi(x) = E\psi(x) \tag{1.4.6}$$

The two solutions are:

$$\psi_L(x) = \exp\left(-\frac{1}{v_F}\int_0^x \mathrm{d}x'\mu(x')\right)\begin{bmatrix}1\\ i\\ 0\\ 0\end{bmatrix}, \quad \text{with} \quad E = v_F q \tag{1.4.7}$$

$$\psi_R(x) = \exp\left(-\frac{1}{v_F}\int_0^x \mathrm{d}x'\mu(x')\right)\begin{bmatrix}0\\ 0\\ 1\\ -i\end{bmatrix}, \quad \text{with} \quad E = -v_F q \tag{1.4.8}$$

Theses two solutions correspond to two counter-propagating localized states at the domain wall. The band structure of this 1D metal inside the gap of the Semenoff insulator is reminiscent of the Dirac cone $E(q_y) = \pm v_F q_y$ with no degeneracy except at $E = 0$ (figure 1.11). A noticeable feature is that both slabs are insulator in the bulk and on their free edges (zigzag edge states exist but do not cross the gap) but conduct at their interface. Contrary to Chern insulators, the edge states are not topologically protected, which is consistent with the time-reversal symmetry of the Semenoff insulator. Each propagating state comes with a counter-propagating state at the same energy, which makes them not protected against back-scattering.

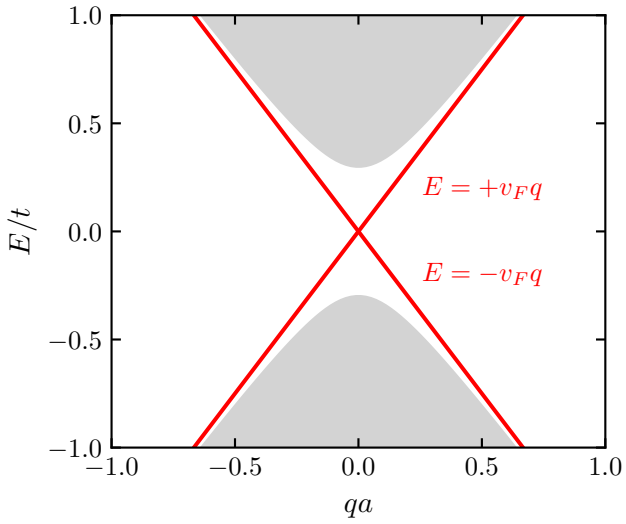

Figure 1.11: Band structure in the low energy approximation of a Semenoff insulator with two domains of opposite masses. The grey area corresponds to the bulk states (see (1.4.2)). The two edge state branches are in red. They present a linear dispersion relation $E(q) = \pm v_F q$ and form a 1D metal between the two Semenoff insulators.

1.5 Edge modes between two Semenoff insulators: tight-binding approach

The low energy analysis near the Dirac point does not specify the size of the domain wall. Actually the topological argument is valid for any shape and any thickness of the domain wall. In this section, we consider two atom-thin domain walls as proposed by Semenoff et al. [55]: a zigzag domain wall and an armchair domain wall. For both interfaces, we calculate the band structure of the 1D metal and the penetration length of the edge states, and compare these calculations to the predictions of the low energy model.

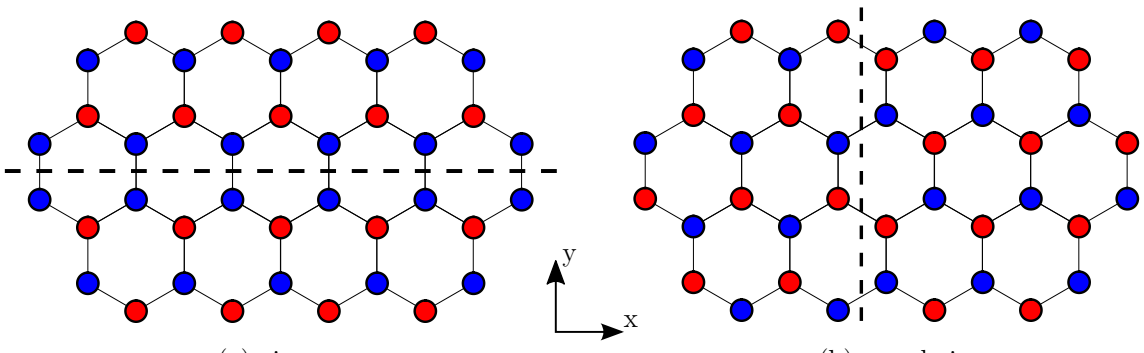

(a) zigzag (b) armchair

Figure 1.12: (a) Zigzag domain wall. (b) Armchair domain wall. The on-site energies are $-\mu$ for the blue dots and $+\mu$ for the red dots. The two sublattices are swapped at the domain wall denoted by a dashed line. Theses figures are taken from [55].

1.5.1 Zigzag domain wall

We consider two semi-infinite Semenoff insulators set aside at $y = 0$ along a zigzag domain wall. The zigzag domain wall is represented in figure 1.12 (a). In this geometry, the system keeps the translation invariance along the x-axis allowing to write the edge mode wavefunction as:

$$\Psi(x, y) = \lambda^{|n|} e^{ik_x x} \Phi(\lambda, k_x), \tag{1.5.1}$$

where n is the index of the unit cell starting from the domain wall along the y-axis, k_x the wavevector in the x direction and $\Phi(\lambda, k_x)$ the sublattice spinor. To find the general solution on the full lattice, we look for solutions $\Phi^{y>0}$ in the $y > 0$ half-plane, and $\Phi^{y<0}$ in the $y < 0$ plane. Then, we impose matching conditions on the domain wall, namely that $|\Psi(\mathbf{r})|^2$ should be symmetric with respect to the $y = 0$ line. In the $y > 0$ half-plane, the Schrödinger equation for $\Phi(\lambda, k_x)$ reads:

$$\begin{bmatrix} E - \mu & -t - 2\lambda t \cos\left(\frac{\sqrt{3}}{2} k_x a\right) \\ -t - 2\lambda^{-1} t \cos\left(\frac{\sqrt{3}}{2} k_x a\right) & E + \mu \end{bmatrix} \begin{bmatrix} \Phi_1 \\ \Phi_2 \end{bmatrix} = 0 \tag{1.5.2}$$

which gives rise to non trivial solutions if:

$$E^2 - \mu^2 - t^2 \left(1 + 4\cos^2\left(\frac{\sqrt{3}}{2} k_x a\right) + 2\cos\left(\frac{\sqrt{3}}{2} k_x a\right)\left(\lambda + \frac{1}{\lambda}\right)\right) = 0. \tag{1.5.3}$$

Two solutions are possible $\lambda = \mathcal{V} \pm \sqrt{\mathcal{V}^2 - 1}$ with:

$$\mathcal{V} = \left(\lambda + \frac{1}{\lambda}\right) = \frac{1}{2\cos\left(\frac{\sqrt{3}}{2} k_x a\right)} \left(\frac{E^2 - \mu^2}{t^2} - 1 - 4\cos^2\left(\frac{\sqrt{3}}{2} k_x a\right)\right) \tag{1.5.4}$$

These solutions are associated with two eigenvectors:

$$\Phi^{y>0} \propto \begin{bmatrix} t + 2t\lambda \cos\left(\frac{\sqrt{3}}{2} k_x a\right) \\ E - \mu \end{bmatrix} \tag{1.5.5}$$

For $y < 0$, the results are the same by symmetry, except that the two lattices are interchanged. The eigenvectors read:

$$\Phi^{y<0} \propto \begin{bmatrix} E - \mu \\ t + 2t\lambda \cos\left(\frac{\sqrt{3}}{2} k_x a\right) \end{bmatrix} \tag{1.5.6}$$

At the interface, the wave function has to be symmetric or anti-symmetric in order to have $|\Psi(\mathbf{r})|^2$ symmetric. The wave matching condition at the interface reads $\Phi^{y>0} = \pm\Phi^{y<0}$. The condition $|\lambda| < 1$ allows us to calculate λ and $E(k_x)$. This derivation recovers the results from Semenoff et al. [55]:

$$\varepsilon_\pm(k_x) = \pm t - \sqrt{\mu^2 + 4t^2 \cos^2 \frac{\sqrt{3} a}{2} k_x} \tag{1.5.7}$$

Figure 1.13 (b) shows this band structure in red compared to the bulk band structure in grey. Figure 1.13 (a) shows the DOS calculated using (1.1.7) for the bulk and edge states. A noticeable feature is the existence of another edge state branch in the lower bulk band.

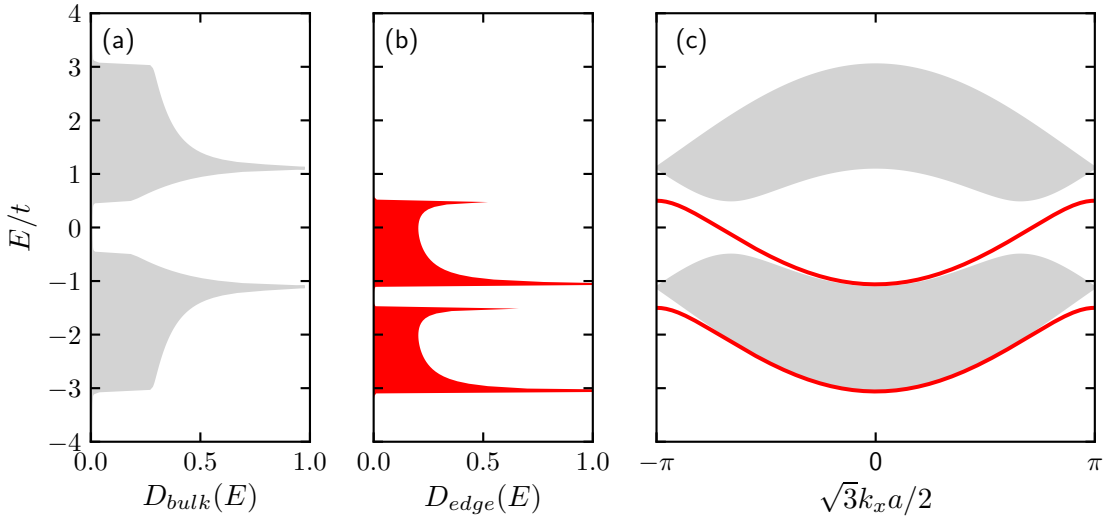

Figure 1.13: Zigzag domain wall: (a) DOS of the bulk on the left and DOS of the edge states for a Semenoff mass $\mu = 0.5t$ on the right. (b) The grey area corresponds to bulk states and the red lines show the dispersion relation of the edge states.

This branch is not predicted by the low energy model. The existence of this branch is not topologically protected but rather peculiar to this specific domain wall. For instance, if one considers a domain wall with A sites rather than B sites at the interface, this branch appears in the upper band.

In order to recover the results obtained in the previous section using the low energy model, we expand the wavevector around the Dirac points for the branch that lies in the gap $k_x = \pm\frac{4\pi}{3\sqrt{3}a} + q$:

$$\varepsilon(q) \simeq t - \sqrt{\mu^2 + t^2} \pm \frac{3t^2}{2\sqrt{\mu^2 + t^2}} qa + O(q^2). \tag{1.5.8}$$

In the limit $t \gg \mu$, we recover the linear dispersion relation $E(q) \simeq \pm\frac{3ta}{2}q$ of the low energy model as shown in figure 1.14

Penetration length

The resolution of the wave-matching problem also gives us access to λ, from which we can define a penetration length ξ:

$$\xi = -\frac{3a}{2}\frac{1}{2\log|\lambda|} \quad \text{with} \quad \lambda = \frac{\sqrt{\mu^2 + 4t^2\cos^2\left(\frac{\sqrt{3}}{2}k_x a\right)} - \mu}{2t\cos\left(\frac{\sqrt{3}}{2}k_x a\right)}. \tag{1.5.9}$$

The factor $\frac{3a}{2}$ is the distance along the y-axis between two cells and the factor 2 comes from our definition of the penetration length as being the decay length of $|\Psi|^2$.

The localization length is plotted in figure 1.14 (b) for increasing Semenoff mass μ. The dashed line shows the localization length predicted by the low energy analysis. A major

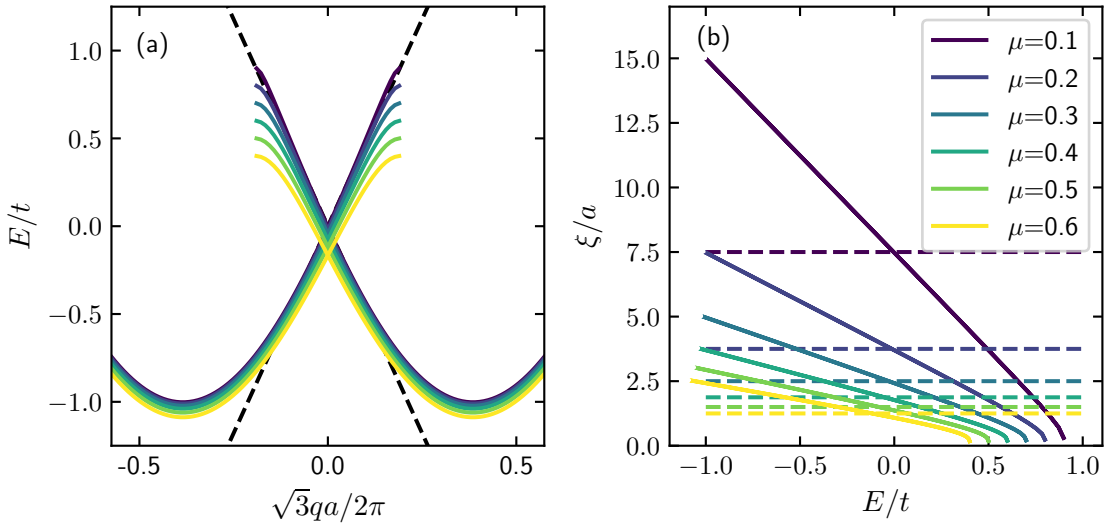

Figure 1.14: (a) Edge state band structure around the Dirac point for different values of μ for a zigzag domain wall. (b) The penetration length (solid line) strongly depends on k contrary to the penetration length predicted by the continuous analysis (dashed lines).

difference between the tight-binding model and the low energy model is that the penetration length depends on the wavevector k_x.

We can expand the penetration length near the Dirac point:

$$\lambda = \frac{\mu}{t} - \sqrt{1 + \frac{\mu^2}{t^2}} + \frac{3\mu}{2t}\left(1 - \sqrt{\frac{\mu^2}{\mu^2 + t^2}}\right) qa + O\left(q^2\right) \tag{1.5.10}$$

At $q = 0$ and in the limit $t \gg \mu$, we obtain $\lambda \simeq -1 + \frac{\mu}{t} \simeq -\exp(-\frac{\mu}{t})$ to first order μ/t. We thus recover the prediction of the low energy model $\xi = \frac{3ta}{4\mu}$. At $q \neq 0$, we obtain to first order:

$$\lambda = -1 + \frac{\mu}{t}\left(1 + \frac{3}{2}qa\right) \simeq -\exp\left(-\frac{\mu}{t}\left(1 - \frac{3}{2}qa\right)\right), \tag{1.5.11}$$

1.5.2 Armchair domain wall

The armchair domain wall is represented on figure 1.12 (b). This geometry is invariant by translation along the y-axis with the vector $\boldsymbol{b} = 3a\,(0, 1)$, which is not a primitive vector of the honeycomb lattice. This complicates the calculation as the edge states are now superposition of two planes waves with wave vectors k_y and $k_y + 2\pi/3a$. We follow the same procedure as for the zigzag domain wall. The wave function takes the form $\Psi = \lambda^{|n|} e^{ik_y y}\Phi$. In the $x > 0$ half plane, the Schrödinger equation reads:

$$\begin{bmatrix} E - \mu & -t\left(1 + \lambda + \lambda^{-1}e^{i3k_y a}\right) \\ -t\left(1 + \lambda^{-1} + \lambda e^{-i3k_y a}\right) & E + \mu \end{bmatrix} \begin{bmatrix} \Phi_1 \\ \Phi_2 \end{bmatrix} = 0 \tag{1.5.12}$$

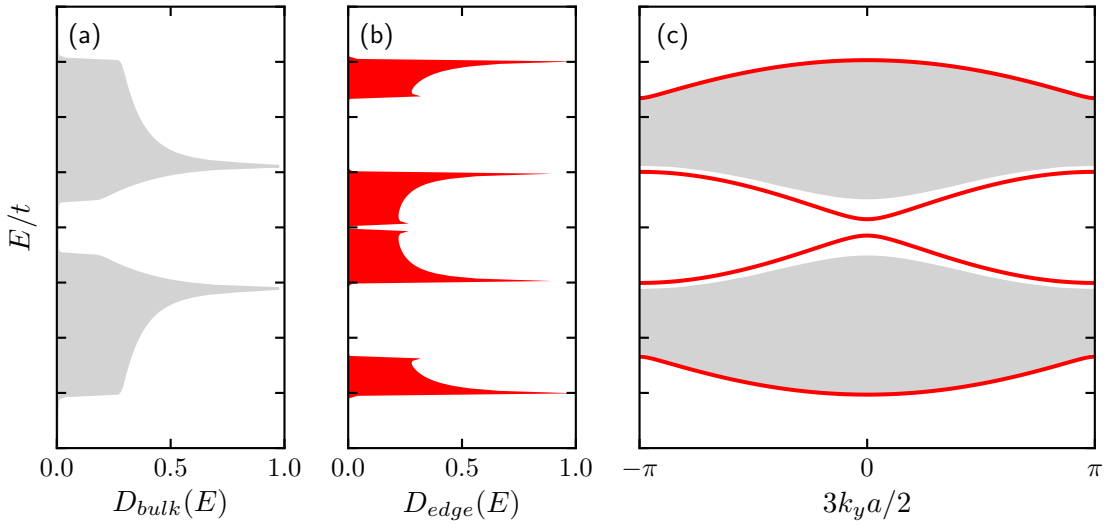

Figure 1.15: Armchair domain wall: (a) DOS of the bulk on the left and DOS of the edge states for a Semenoff mass $\mu = 0.5t$ on the right. (b) The grey area corresponds to bulk states and the red lines show the dispersion relation of the edge states.

We can change the phase of λ without changing the equation by setting: $\tilde{\lambda} = \lambda e^{-i3k_y a/2}$ and to introducing $2C = \lambda + \lambda^{-1}$:

$$\begin{bmatrix} E-\mu & -t\left(1+2e^{i3k_y a/2}C\right) \\ -t\left(1+2e^{-i3k_y a/2}C\right) & E+\mu \end{bmatrix} \begin{bmatrix} \Phi_1 \\ \Phi_2 \end{bmatrix} = 0. \tag{1.5.13}$$

Non-trivial solutions exist if:

$$E^2 - \mu^2 - t^2\left(4C^2 + 4C\cos\frac{3a}{2}k_y + 1\right) = 0 \tag{1.5.14}$$

This is a second order equation in C with two solutions C_1 and C_2. We use the relation between coefficients and roots of a 2$^{\text{nd}}$ order polynomial to write:

$$C_1 + C_2 = -\cos\frac{3a}{2}k_y \tag{1.5.15}$$

$$E^2 = \mu^2 + t^2 - 4t^2 C_1 C_2 \tag{1.5.16}$$

We now introduce K such that:

$$\varepsilon(k_y) = \pm\sqrt{t^2\sin^2\frac{3a}{2}k_y + \mu^2 K} \tag{1.5.17}$$

Using this definition of K and the two equations (1.5.15), (1.5.16), we obtain:

$$K - 1 = \frac{t^2}{\mu^2}\left(C_1 - C_2\right)^2 \tag{1.5.18}$$

This equation and (1.5.15) are equivalent to the equations obtained in Semenoff et al. [55]. By applying wave-matching at $y = 0$ and taking into account that there are two solutions, we get:

$$K(1-\lambda_1^2)(1-\lambda_2^2) = (1-\lambda_1\lambda_2)^2 \tag{1.5.19}$$

The set of equations (1.5.15) – (1.5.19) have to be solved numerically. The figure 1.15 shows the DOS and the band structure of the edge modes. There is a gap between the edge state branches at $E = 0$. We also observe two supplementary branches. In order to compare to the low energy model, we first expand the energy spectrum for $\mu \ll t$. The two branches read:

$$\varepsilon_1(q) = \pm\sqrt{\mu^2 + t^2\left(5 + 4\cos\frac{3a}{2}q\right)} \tag{1.5.20}$$

$$\varepsilon_2(q) = \pm\sqrt{t^2\sin^2\frac{3a}{2}q + \frac{4\mu^4}{t^2\left(4-\cos^2\frac{3a}{2}q\right)^2}} \tag{1.5.21}$$

At first order in μ/t and $qa \ll 1$, we recover the linear dispersion relation $\varepsilon(q) = \pm v_F q$. However, a gap appears at order μ^4/t^2 in the dispersion relation. This gap is of the order $\Delta E = 4\mu^2/3t$ and goes to zero in the $\mu \ll t$ limit.

Penetration length

The resolution of the wave matching problem also gives two solutions Φ_1 and Φ_2 associated with two values λ_1 and λ_2. The general form of the edge state is a linear combination of these two solutions:

$$\Psi(\mathbf{r}) = \alpha\lambda_1^{|n|}e^{iqy}\Phi_1 + \beta\lambda_2^{|n|}e^{i\left(q+\frac{2\pi}{3a}\right)y}\Phi_2 \tag{1.5.22}$$

To define the penetration length, we see that one of the two solutions decays faster than the other, and we define:

$$\xi = \max_{i=1,2}\left\{-\frac{\sqrt{3}a}{2}\frac{1}{2\log|\lambda_i|}\right\} \tag{1.5.23}$$

Figure 1.16 (b) shows this penetration length as a function of the energy (solid line) compared to the prediction of the continuous model (dashed line). Unlike the zigzag domain wall, the penetration length is almost constant.

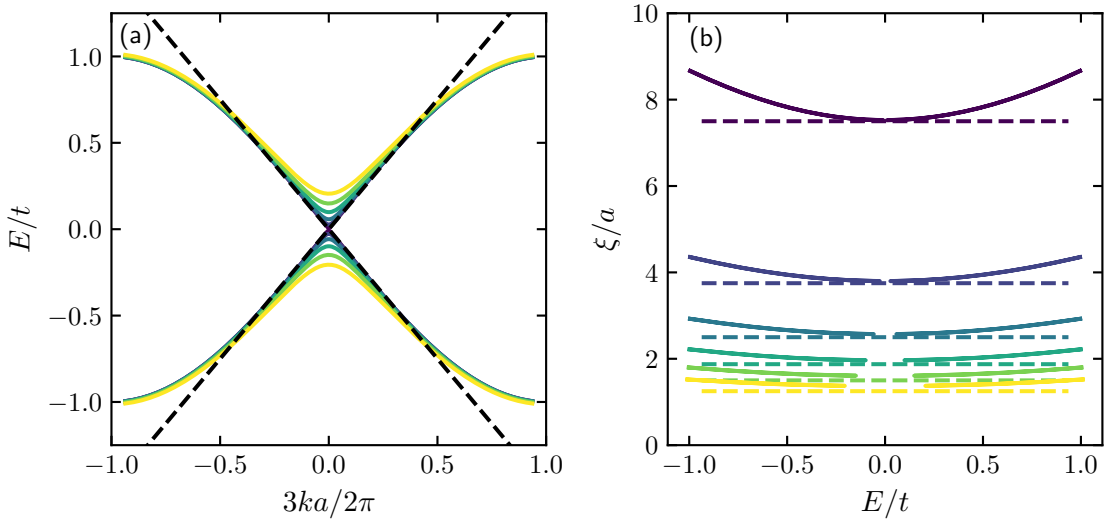

Figure 1.16: (a) Edge state band structure around the Dirac point for different values of μ for an armchair domain wall. A gap appears that increases with μ. (b) The penetration length (solid line) weakly depends on the mode wavevector and is close to the localization length obtained from the low energy model (dashed line).

1.6 Conclusion

In this chapter, we have analyzed the bulk properties of the honeycomb lattice without and with a Semenoff mass. For both, it is possible to identify a set of points of interest in the DOS that allow us to deduce the tight-binding parameters. For the honeycomb lattice, we have derived the flat band structure of zigzag and bearded edge states and their penetration length. In the case of the Semenoff insulator, we have characterized its topological properties, namely the two topological valley charges at the Dirac points. These charges allow us to understand the existence of edge states between two Semenoff insulators with opposite masses. These edge states have been further characterized for two domain walls: zigzag and armchair. For both geometries, we have derived their band structure as well as their penetration length. In both cases, we have seen that in the Dirac limit $\mu \ll t$ and in the low energy limit $qa \ll 1$, the tight-binding model recovers the results from the low energy model.

Chapter 2

Models for superconducting lattices

Contents

In this chapter, we present the two different models that we have developed in order to describe lattices of superconducting resonators. The starting point for each model is the numerical simulation by the Sonnet software of a single or a few coupled resonators, from which we extrapolate a model of the full lattice. The first model takes as an input the admittance matrix computed by Sonnet for a few lattice sites and periodize it. We then look for Bloch wave solutions to the equation of motion for the voltage amplitude across the lattice. The second model only needs the simulation of a single resonator and takes as an input the charge and current distribution of the fundamental mode. We then apply a coupled mode theory (CMT) in order to obtain the lattice band structure.

The chapter starts by a description of the spiral resonator that constitutes the building block of all the lattices described in this manuscript. In particular, we show the simulated charge and current distributions of the first resonant modes that are used in the CMT model. We then detail the two models and compare them. In the strong coupling regime, which is relevant for the experiment shown in chapter 4, we show that the admittance model is more appropriate. We have performed several checks that indicate that the admittance model correctly describe the lattice despite the large coupling strength. In the moderate coupling range, which is relevant for the experiment shown in chapter 5, both models agree.

2.1 Properties of the spiral resonator

2.1.1 Resonant modes

The spiral is a folded $\lambda/2$ resonator with a total length $l = 8.6\,\mathrm{mm}$ as shown in figure 2.1. The characteristic impedance of a microstrip line having the same width as the wire forming the spiral is $Z_0 = 143.2\,\Omega$ and the phase velocity is $v_p = 9.25 \times 10^7\,\mathrm{m \cdot s^{-1}}$. For a straight line resonator, this would give rise to resonance frequencies being multiples of $v_p/2l = 5.38\,\mathrm{GHz}$.

Figure 2.1 shows the imaginary part of the self-admittance calculated by Sonnet using a port at the center of the spiral. Qualitatively, the admittance is similar to the one of a $\lambda/2$ resonator, which is a tangent function. But the positions of the zeros, which correspond to the resonances, and the variation around a resonance are quantitatively different because of the spiral shape[1]. We observe that the resonance frequencies are equidistant and their value is well approximated by $5.95\,\mathrm{GHz} + n \times 8.17\,\mathrm{GHz}$ where $n = 0, 1, \ldots$ labels the resonance.

Figure 2.2 shows the current and charge distributions of the first three lowest modes. Once again, we observe a qualitative but not quantitative agreement with the expected sine and cosine mode distributions of a $\lambda/2$ resonator. Because of the presence of the ground plane below the substrate, the complete charge and current distributions for a given mode also include the image distributions that must be taken into account to compute the electric and magnetic field. We will detail this point when we describe the CMT model.

2.1.2 Coupling between two resonators

To characterize the coupling between two resonators, we simulate with Sonnet two resonators separated by an edge to edge distance d and we extract the admittance matrix (or Y-matrix)

[1]Of course, the self-admittance function depends on the location of the port in the resonator. Only the positions of the zeros that indicate the resonances are independent of the port location.

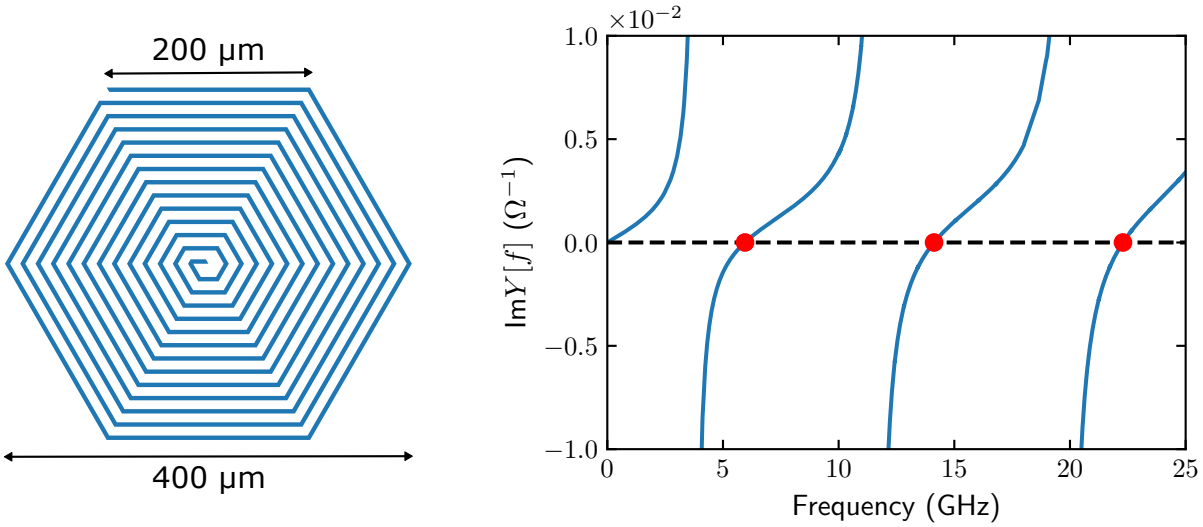

Figure 2.1: On the left, design of the spiral used for the sites of our different lattices. The spiral is a 8.6 mm long wire with a width of 4.33 µm and a gap between adjacent line of 8.66 µm. The wire is deposited on a dielectric substrate (usually Si), whose back side is covered with metal and connected to the ground. On the right, we show the self-admittance calculated for a port located at the center of the spiral. The resonances correspond to the zero-crossings (red dots), which are linearly spaced with a fundamental resonance at 5.95 GHz.

calculated with two ports, one at the center of each spiral. The voltage amplitude at each port is given by the solution of the linear system

$$Y[\omega]V = I \tag{2.1.1}$$

where I is the vector representing the current injected at each port. In the absence of source terms $I = 0$ and the system has a non-trivial solution iff $\det Y[\omega] = 0$, which gives the resonance condition. The output of Sonnet is an estimation of the Y matrix coefficients in a given frequency range with a given number of frequency points. From this output, we build an interpolating function $Y[\omega]$ that we use later for our numerical calculations. Because the system is lossless, we suppose that the admittance is purely imaginary and discard the real part given by Sonnet, which is anyway negligible. The function $\det Y[\omega]$ is then real and its zero-crossings correspond to the resonance frequencies.

Figure 2.3 shows the evolution of the diagonal and off-diagonal elements of the imaginary part of $Y[\omega]$ as a function of frequency for a distance $d = 5$ µm. The evolution of $\log|\det Y[\omega]|$ is also shown, with two dips corresponding to the two resonances of the coupled system. We define the coupling t as the half-splitting between these resonances. The figure 2.3c shows the evolution of t as a function of the distance d. Because the spiral is not invariant by a rotation of $\pi/3$, the coupling t depends on the spiral orientation with respect to the direction of separation. More details about this anisotropy are given in 4.1.

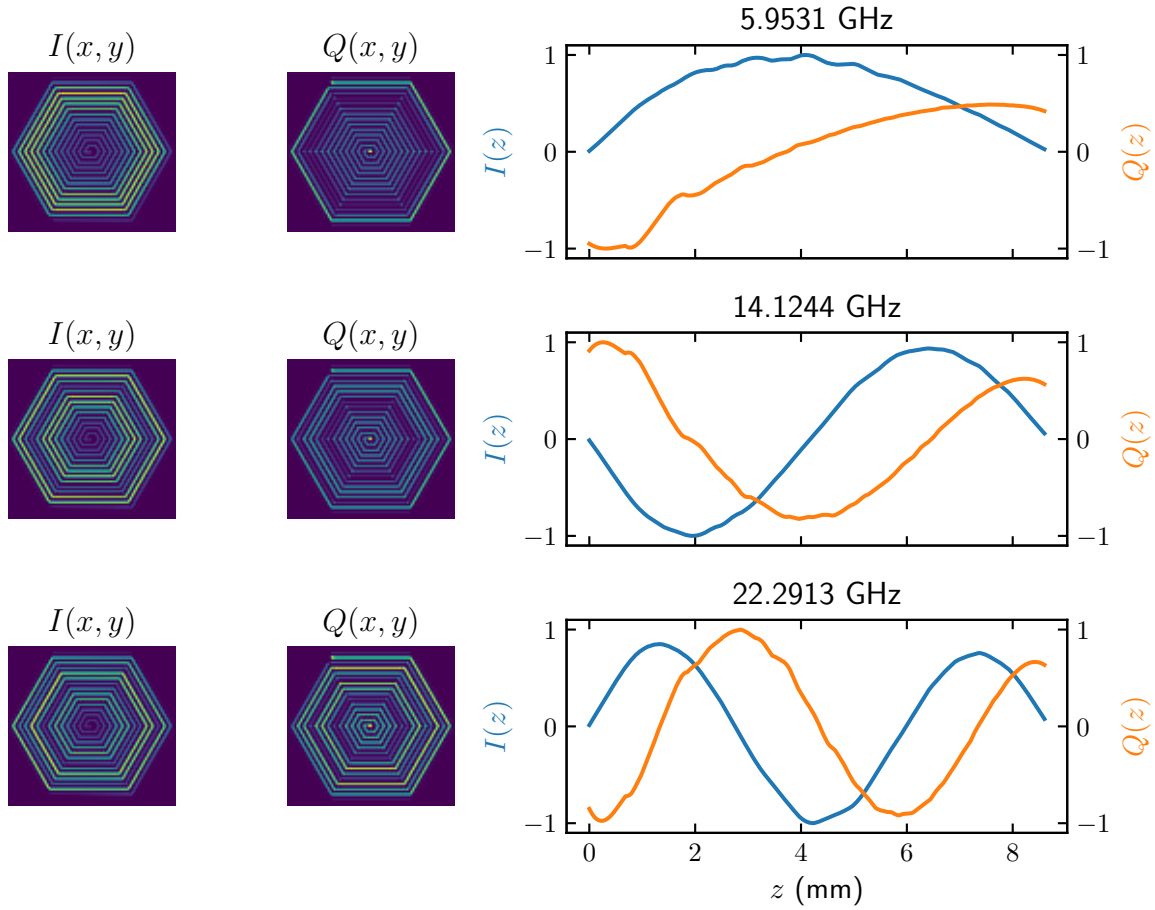

Figure 2.2: Current and charge distributions in the spiral resonator for the first three lowest modes. The right figures show the normalized unfolded distributions along the wire. They are qualitatively similar to the ones of a straight $\lambda/2$ resonator.

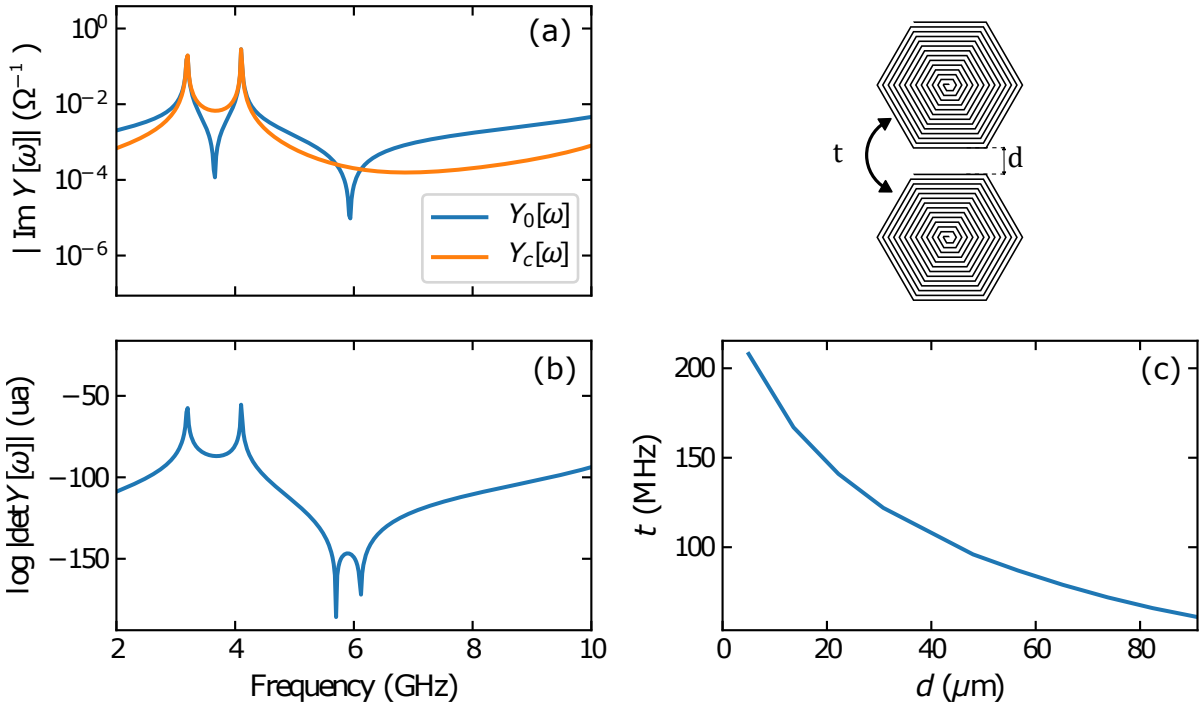

Figure 2.3: Coupling of two spiral resonators. (a) Evolution of the diagonal Y_0 and off-diagonal Y_c elements of the admittance matrix as function of frequency for $d = 5\,\mu\mathrm{m}$. (b) Evolution of $\log|\det Y[\omega]|$. The two minima indicate the position of the two resonances. (c) Evolution of the half-splitting between the two resonances as a function of the distance d. The spiral orientation is shown above.

2.2 Admittance matrix periodization

In the last section, we have used the admittance matrix to find the resonances of a single resonator and of two coupled resonators. In principle, one could extend this method to a larger system and look for the zeros of $\det Y[\omega]$ in order to find the eigenmodes of the finite size lattice corresponding to the one that is experimentally realized. However, this method is not very satisfying and is anyway impractical. Our lattices with a few hundred resonators cannot be simulated directly with Sonnet, at least on a standard desktop computer. In this section, we show how we can approximate the periodic admittance of an infinite lattice from the numerical simulation of a small circuit with only a few sites. The solutions of the equation $YV = 0$ are then easily found as Bloch waves. This method has already been used to describe lumped element lattices with non-trivial topology [39, 72].

2.2.1 Band structure from the admittance matrix

We consider an infinite lattice of resonators with N ports per unit cell and look for a solution at a given frequency ω. The voltage amplitude $V(\mathbf{r})$ at the site $\mathbf{r}$ is a complex vector with N components that satisfies

$$Y_0[\omega]V(\mathbf{r}) + \sum_i Y_i[\omega]V(\mathbf{r}+\boldsymbol{a}_i) + Y_i^T[f]V(\mathbf{r}-\boldsymbol{a}_i) = 0 \tag{2.2.1}$$

Here, $Y_0[\omega]$ is the admittance matrix between the ports belonging to the same cell and $Y_i[\omega]$ is the admittance matrix between the ports corresponding to two cells separated by a lattice vector $\boldsymbol{a}_i$. In principle, the sum over i is infinite but, in practice, the matrix elements of Y_i decrease with i and the sum can be truncated to $i_{\max}$ terms. We look for a Bloch wave solution $V[\mathbf{r}] = Ve^{i\mathbf{kr}}$ and obtain

$$\left(Y_0[\omega] + \sum_i^{i_{\max}} Y_i[\omega]e^{i\mathbf{k}\boldsymbol{a}_i} + Y_i^T[\omega]e^{-i\mathbf{k}\boldsymbol{a}_i}\right)V = 0 \tag{2.2.2}$$

The dispersion relation is obtained from the solution of:

$$\det\left(Y[\omega] + \sum_i^{i_{\max}} Y_i[\omega]e^{i\mathbf{k}\boldsymbol{a}_i} + Y_i^T[\omega]e^{-i\mathbf{k}\boldsymbol{a}_i}\right) = 0 \tag{2.2.3}$$

Two practical problems arise: one must choose the number of ports N per unit cell and their locations, and one has to determine the number of coupling terms $i_{\max}$. As we show below, the two quantities N and $i_{\max}$ are actually linked.

We emphasize that the number of terms appearing in the sum is not directly connected to the number of coupling terms in an effective tight-binding description of the lattice. For example, a chain of capacitively coupled LC resonators is exactly described by a nearest-neighbor admittance matrix but the effective tight-binding model contains a coupling that decreases exponentially with the distance and is not strictly a NN coupling. The converse is also true, a lattice may be well described by a NN tight-binding model even though the coefficients of the Y_i matrices decrease slowly with i.

2.2.2 Influence of the number of ports

We now consider the case of a honeycomb lattice of spiral resonators. Figure 2.4 shows the band structure obtained from the simulation of a small system with only four resonators and one port at the center of each resonator. The Sonnet simulation yields a 4×4 admittance matrix. From this matrix, we extract the orientation dependent admittance coupling Y_i between two resonators and the self-admittance Y_0 from the self-admittance of the central resonator. We see that, for the smallest distance $d = 5\,\mu\text{m}$, the calculation fails to find a

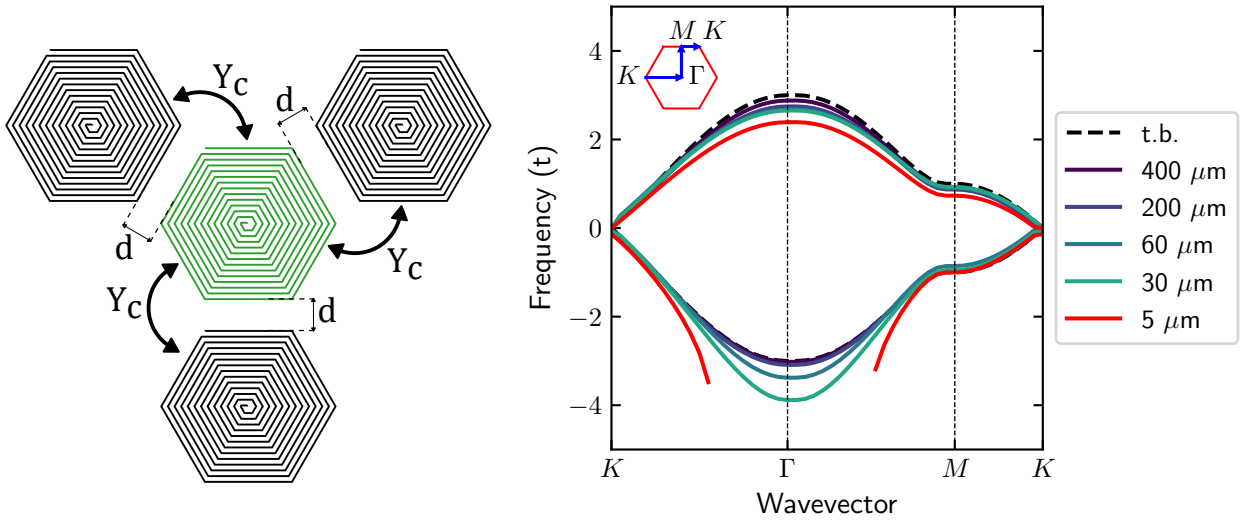

Figure 2.4: Band structure of a honeycomb lattice of spiral resonators. The Sonnet simulation is done with a four resonator system. We plot the band structure deduced from the computed admittance matrix. The inset shows the path followed in the first Brillouin zone. The band structure is normalized to the coupling t that is calculated from the two resonator case. At the smallest distance, the band structure calculation fails to find the lower band.

complete lower band. This indicates that the truncation to the NN admittance coupling with one port per resonator is very inaccurate. This problem is cured by increasing the number of ports as shown in figure 2.5. Already with two ports, the calculation finds two bands in the complete Brillouin zone and adding a third port almost does not change the band structure.

2.2.3 Influence of the coupling range

In order to understand better the convergence of the calculated band structure, we have performed simulations on a larger system with 16 resonators (see figure 2.8) and different numbers of ports per resonator (from 1 to 6). The distance d is fixed to $5\,\mu\text{m}$, which is the most problematic case. Figure 2.6 shows the decay of the Y_i coefficients as a function of distance for different numbers of ports per resonator. With only one port per resonator, the coefficients slowly decrease but that increasing the number of ports leads to a much faster decay.

In figure 2.7, we compare the calculated band structures as a function of $i_{\max}$ for different numbers of ports. With two ports or more, the results barely change, as already observed

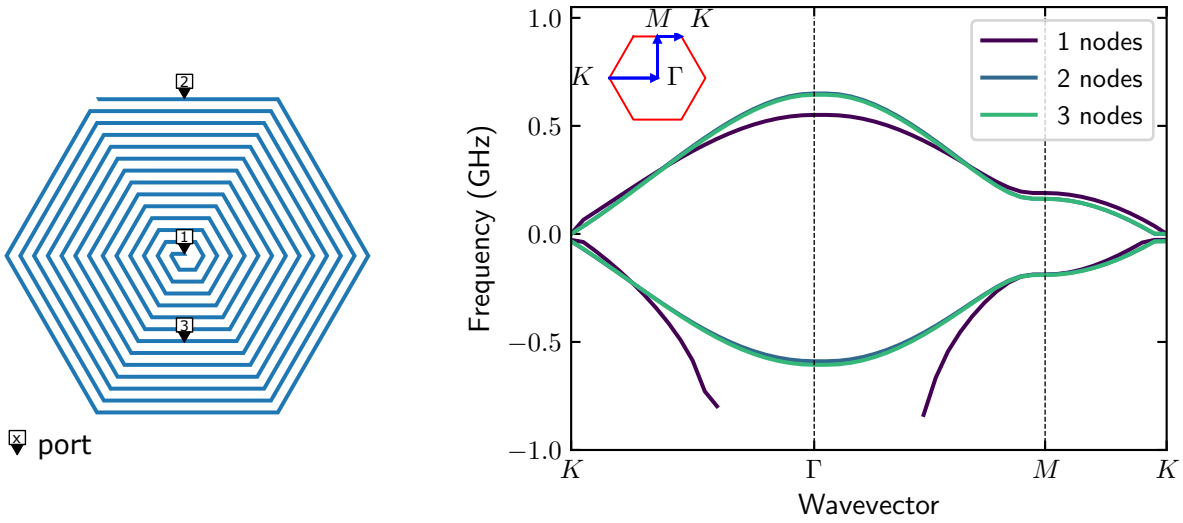

Figure 2.5: Band structure of a honeycomb lattice of spiral resonators. The Sonnet simulation is done with four resonators as shown in figure 2.4. We vary the number of ports per resonator, their locations are shown on the left. The distance between resonators is $d = 5\,\mu\text{m}$. The calculated band structure rapidly converges when the number of ports is larger or equal to two.

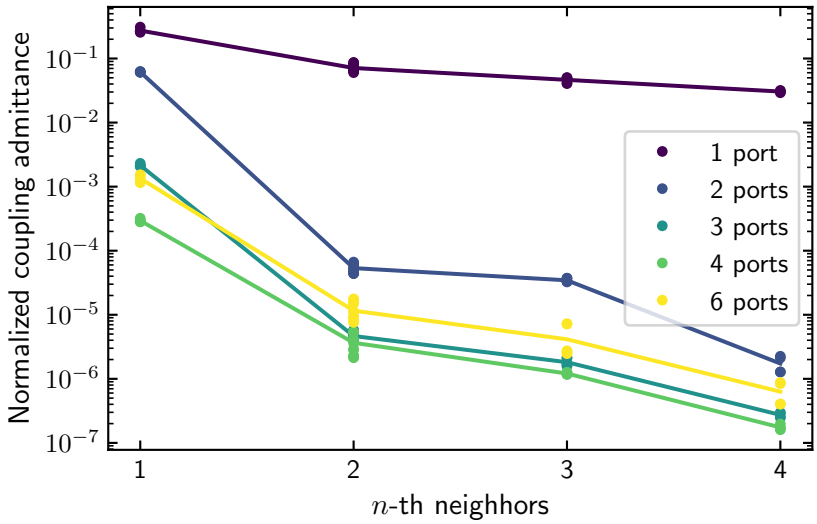

Figure 2.6: Decay of the Y_i matrix elements as a function of distance. Each color corresponds to a different number of ports per resonator. The ports are located in order to split the spiral wire in approximately equal pieces. Each point corresponds to the average of the admittance in a frequency band from 5 to 7 GHz. The different points with the same index correspond to the same distance but different coupling directions. The line shows the decay of the average over the different directions.

above in the four site simulation. We also see that keeping the fourth neighbor admittance matrix does not modify the band structure as compared to the calculation including NN, NNN and NNNN admittance terms, except for the single port case. In this case, the inclusion of more terms has a strong effect because of the slow decay of the Y_i coefficients.

Finally, we compare in figure 2.8 the band structures obtained with fourth neighbor coupling and different numbers of ports. We also consider two different locations of the ports in the case of the three port simulation. All the curves with two or more ports are identical up to a global offset that we substract. We are thus confident that the simulated band structure calculated with the admittance model is an accurate numerical description of the lattice.

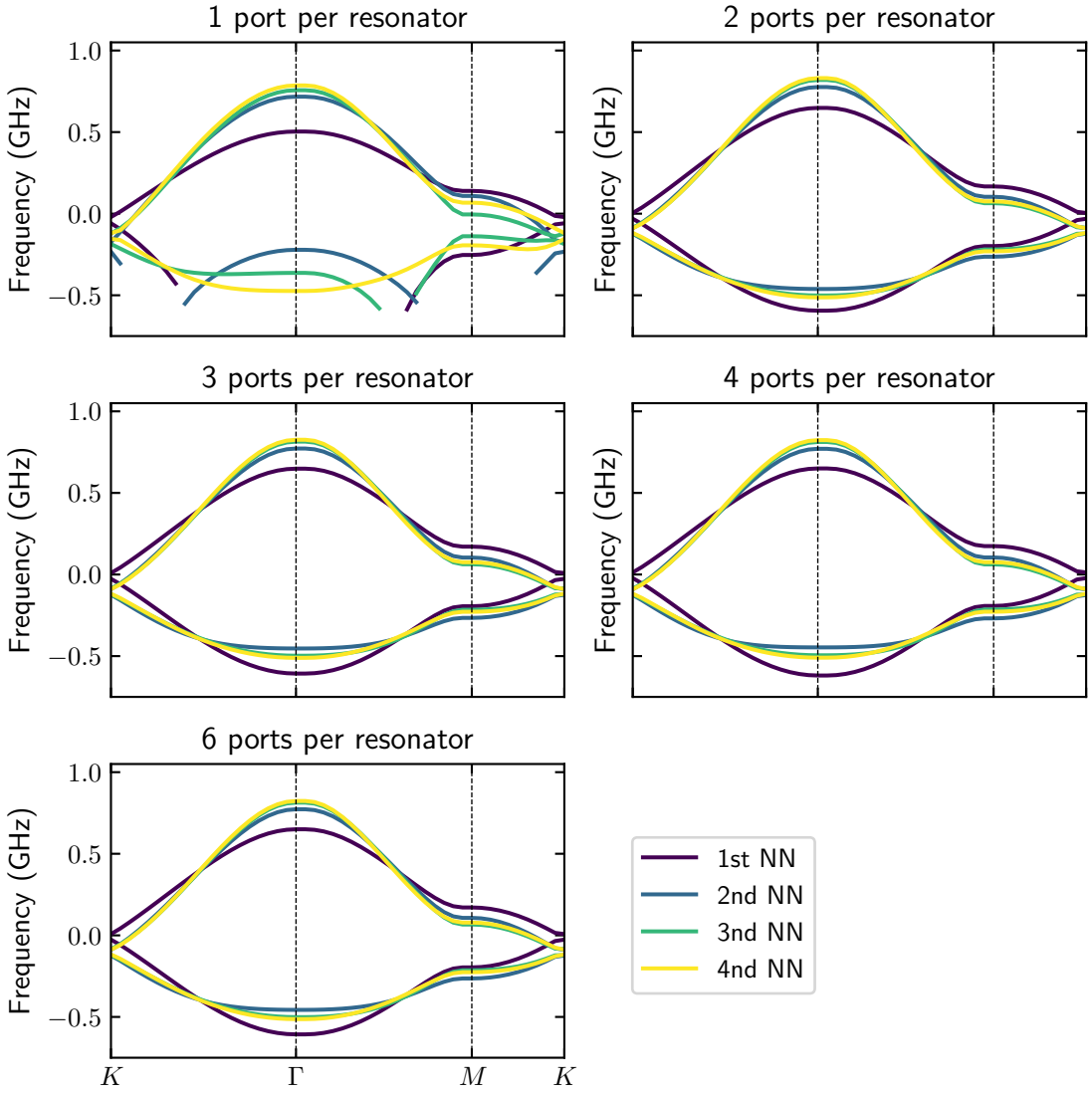

Figure 2.7: Band structure of a honeycomb lattice of spiral resonators. The Sonnet simulation is done with 16 resonators. Each plot corresponds to a given number of ports per resonator. Each line is the calculated band structure where we increase the number $i_{\max}$ of coupling admittance matrices that are taken into account in the calculation.

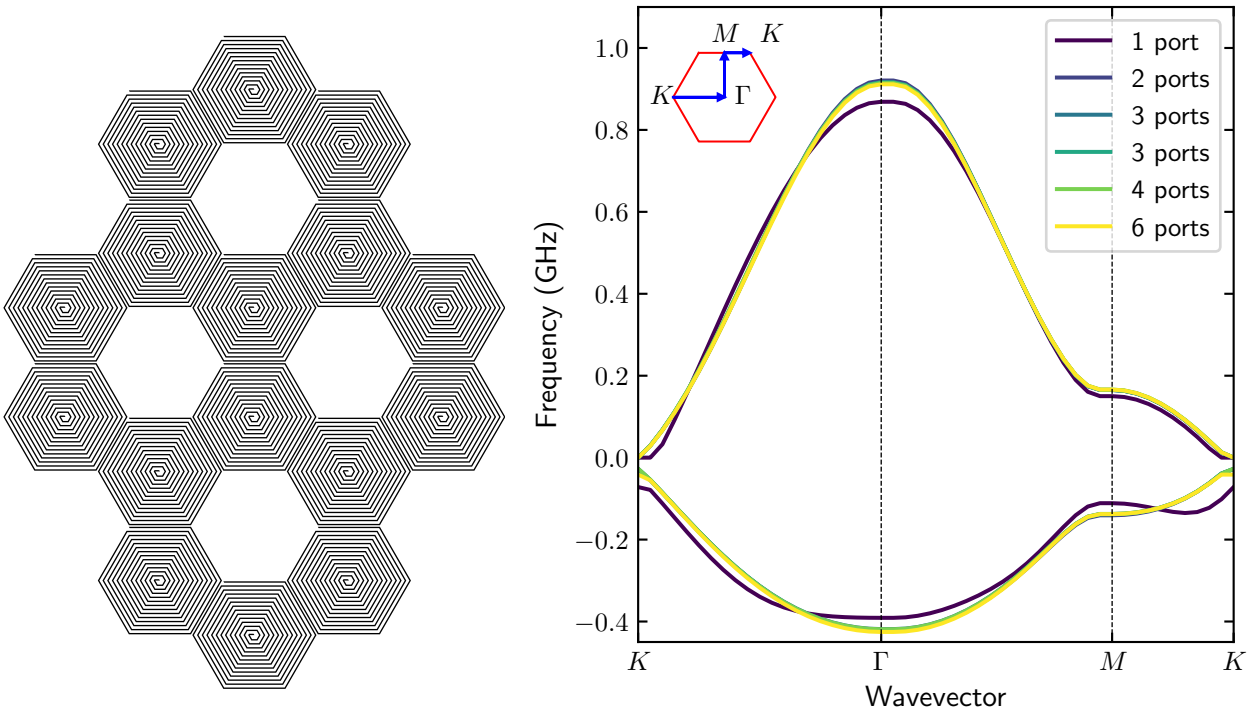

Figure 2.8: Band structure of a honeycomb lattice of spiral resonators. The Sonnet simulation is done with 16 resonators as shown on the left. Each curve is obtained with a different number of ports per resonator. In the case of three ports, we consider two different locations of the central port. Except for the single port case, all the curves lead to the same band structure up to a small offset that is here subtracted.

2.3 Coupled mode theory

In the last section, we have presented a calculation of the band structure of a lattice of resonators using the admittance matrix. In the context of meta-material based on arrays of resonators, several works [73–75] have developed a coupled mode theory (CMT) in order to predict the band structure. In this section, we briefly review this approach and apply it to our situation. We then compare the obtained results with the ones of the admittance model.

2.3.1 Coupled mode theory for a periodic lattice

The coupled mode theory is a generic method where the fields of interest are expanded on a mode basis in order to drastically reduce the number of degrees of freedom and obtain an easily tractable model. The application of CMT to coupled microwave resonators is detailed in Elnaggar et al. [75]. In its simplest form, the expansion is performed over the modes of the uncoupled elements, which are supposed to be known. The CMT is then a perturbative approach and its regime of validity is limited to the weak coupling regime.

In the case of our lattice of resonators, we suppose that we know the current and charge distribution $\boldsymbol{j}_i$ and ρ_i of the i^{th} resonant mode with resonant frequency ω_i of an isolated spiral resonator. These charge and current distributions give rise to an electric field $\boldsymbol{E}_i$ and a magnetic field $\boldsymbol{B}_i$. We look for a solution to the Maxwell equations in the lattice as

$$\boldsymbol{E}(\mathbf{r}', t) = \sum_r \sum_i a_i(\mathbf{r}) \boldsymbol{E}_i(\mathbf{r}' - \mathbf{r})\, e^{i\omega t} \tag{2.3.1}$$

$$\boldsymbol{B}(\mathbf{r}', t) = \sum_r \sum_i b_i(\mathbf{r}) \boldsymbol{B}_i(\mathbf{r}' - \mathbf{r})\, e^{i\omega t} \tag{2.3.2}$$

where the sum over $\mathbf{r}$ is over the lattice cells and the complex coefficients $a_i(\mathbf{r})$ and $b_i(\mathbf{r})$ are the electric and magnetic amplitudes of the i^{th} mode at site $\mathbf{r}$. The resonance condition for the coupled system is obtained by equating the electric and magnetic energies $\boldsymbol{a}^\dagger D \boldsymbol{a} = \boldsymbol{b}^\dagger G \boldsymbol{b}$. The coefficient of the D and G matrices are overlap integrals of the electric and magnetic fields of the modes at different sites. The vector $\boldsymbol{b}$ can be eliminated using Maxwell equations and the resonance condition yields the eigenvalue problem [75]:

$$\Omega G^{-1} \Omega D \boldsymbol{a} = \omega^2 \boldsymbol{a} \tag{2.3.3}$$

where Ω is a diagonal matrix containing the resonance frequencies of the different modes at the different sites. Here, we suppose that all the materials are non-magnetic and we also neglect the fact the fields of a given resonator may not fulfill the correct boundary conditions on the conductor of a nearby resonator.

In order to take advantage of the lattice periodicity, we rather look for a periodic solution with momentum $\mathbf{k}$ as:

$$\boldsymbol{E}_{\mathbf{k}}(\mathbf{r}', t) = \sum_{\mathbf{r}} \sum_i e^{i\mathbf{k}\mathbf{r}} a_i(\mathbf{k}) \boldsymbol{E}_i(\mathbf{r}' - \mathbf{r})\, e^{i\omega t} \tag{2.3.4}$$

$$\boldsymbol{B}_{\mathbf{k}}(\mathbf{r}', t) = \sum_{\mathbf{r}} \sum_i e^{i\mathbf{k}\mathbf{r}} b_i(\mathbf{k}) \boldsymbol{B}_i(\mathbf{r}' - \mathbf{r})\, e^{i\omega t} \tag{2.3.5}$$

The resonance condition is then

$$\Omega G^{-1}(\mathbf{k}) \Omega D(\mathbf{k}) \boldsymbol{a}(\mathbf{k}) = \omega^2(\mathbf{k}) \boldsymbol{a}(\mathbf{k}) \tag{2.3.6}$$

where $\boldsymbol{a}(\mathbf{k})$ is now a small vector, whose length corresponds to the number of orbitals per lattice cell. The matrix Ω is the diagonal matrix obtained from the resonance frequencies of each orbital. Finally, the matrix elements of $G(\mathbf{k})$ and $D(\mathbf{k})$ are given by

$$D_{ij}(\mathbf{k}) = \sum_{\mathbf{r}} e^{i\mathbf{kr}} \langle \boldsymbol{E}_i \boldsymbol{E}_j \rangle_{\mathbf{r}} \quad \text{and} \quad G_{ij}(\mathbf{k}) = \sum_{\mathbf{r}} e^{i\mathbf{kr}} \langle \boldsymbol{B}_i \boldsymbol{B}_j \rangle_{\mathbf{r}} \tag{2.3.7}$$

where the overlap integrals are defined as

$$\langle \boldsymbol{E}_i \boldsymbol{E}_j \rangle_{\mathbf{r}} = \frac{1}{4} \int_V \epsilon(\mathbf{r}') \mathrm{Re}\left[\boldsymbol{E}_i^*(\mathbf{r}') \cdot \boldsymbol{E}_j(\mathbf{r}' - \mathbf{r}) \right] \mathrm{d}^3\mathbf{r}' \tag{2.3.8}$$

$$\langle \boldsymbol{B}_i \boldsymbol{B}_j \rangle_{\mathbf{r}} = \frac{1}{4\mu_0} \int_V \mathrm{Re}\left[\boldsymbol{B}_i^*(\mathbf{r}') \cdot \boldsymbol{B}_j(\mathbf{r}' - \mathbf{r}) \right] \mathrm{d}^3\mathbf{r}' \tag{2.3.9}$$

2.3.2 Evaluation of the overlap integrals

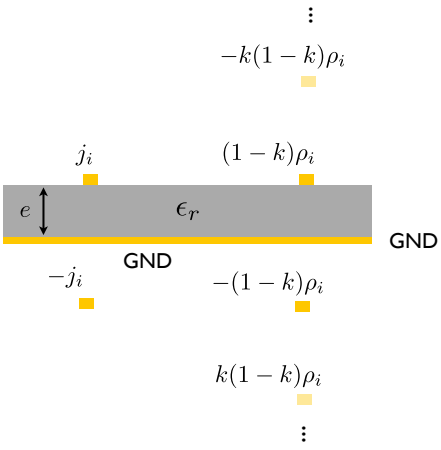

Figure 2.9: Image current and image charge. The image current is simply the mirror image of the current distribution of the resonator by the ground plane. The case of the charge distribution is more complicated because of the dielectric interface. There is an infinite series of image charges with decreasing values.

The integrals appearing in the definition of D and G correspond to the electric and magnetic coupling energies between two resonators separated by a lattice vector $\mathbf{r}$. In the absence of the dielectric substrate and without the ground plane, these coupling energies could be simply rewritten in terms of charge and current distributions as [76]:

$$\langle \boldsymbol{E}_i \boldsymbol{E}_j \rangle_{\mathbf{r}} = \frac{1}{16\pi\epsilon_0} \int \mathrm{Re}[\rho_i^*(\mathbf{r}_1)\rho_j(\mathbf{r}_2 - \mathbf{r})] \frac{1}{|\mathbf{r}_1 - \mathbf{r}_2 + \mathbf{r}|} \mathrm{d}^2\mathbf{r}_1 \mathrm{d}^2\mathbf{r}_2 \tag{2.3.10}$$

$$\langle \boldsymbol{B}_i \boldsymbol{B}_j \rangle_{\mathbf{r}} = \frac{\mu_0}{16\pi} \int \mathrm{Re}[j_i^*(\mathbf{r}_1) j_j(\mathbf{r}_2 - \mathbf{r})] \frac{1}{|\mathbf{r}_1 - \mathbf{r}_2 + \mathbf{r}|} \mathrm{d}^2\mathbf{r}_1 \mathrm{d}^2\mathbf{r}_2 \tag{2.3.11}$$

The presence of the image current and the image charges, as shown in figure 2.9, modify

these formula to

$$\langle \boldsymbol{E}_i \boldsymbol{E}_j \rangle_{\mathbf{r}} = \frac{1-k}{16\pi\epsilon_0} \int \mathrm{Re}[\rho_i^*(\mathbf{r}_1)\rho_j(\mathbf{r}_2-\mathbf{r})] \left(\frac{1}{|\mathbf{r}_1-\mathbf{r}_2+\mathbf{r}|} + \sum_{n=1}^{M} \frac{(-1)^n k^{n-1}(1+k)}{|\mathbf{r}_1-\mathbf{r}_2+\mathbf{r}-2ne\boldsymbol{z}|} \right) \mathrm{d}^2\mathbf{r}_1 \mathrm{d}^2\mathbf{r}^2 \tag{2.3.12}$$

$$\langle \boldsymbol{B}_i \boldsymbol{B}_j \rangle_{\mathbf{r}} = \frac{\mu_0}{16\pi} \int \mathrm{Re}[j_i^*(\mathbf{r}_1) j_j(\mathbf{r}_2-\mathbf{r})] \left(\frac{1}{|\mathbf{r}_1-\mathbf{r}_2+\mathbf{r}|} - \frac{1}{|\mathbf{r}_1-\mathbf{r}_2+\mathbf{r}-2e\boldsymbol{z}|} \right) \mathrm{d}^2\mathbf{r}_1 \mathrm{d}^2\mathbf{r}_2 \tag{2.3.13}$$

where e is the wafer thickness, $k = (\epsilon_r - 1)/(\epsilon_r + 1)$, ϵ_r is the dielectric constant of the wafer and M is the number of image charges at which the sum is truncated, we use $M = 4$. These expressions neglect any propagation effect, we have checked that this approximation is fully justified in our situation.

We numerically compute these integrals from the charge and current distribution ρ_i and $\boldsymbol{j}_i$ that we obtain from Sonnet. Before calculating the band structure of a full lattice, let us compare the coupling between two resonators as predicted by the CMT to the one obtained from the admittance model. We consider the fundamental mode and define the electric and magnetic coupling constants κ_e and κ_m as

$$\kappa_e = \langle \boldsymbol{E}_0 \boldsymbol{E}_0 \rangle_{\mathbf{r}} / \langle \boldsymbol{E}_0 \boldsymbol{E}_0 \rangle_0 \tag{2.3.14}$$

$$\kappa_m = \langle \boldsymbol{B}_0 \boldsymbol{B}_0 \rangle_{\mathbf{r}} / \langle \boldsymbol{B}_0 \boldsymbol{B}_0 \rangle_0 \tag{2.3.15}$$

The resonance condition can then be written

$$\begin{pmatrix} 1 & \kappa_m \\ \kappa_m & 1 \end{pmatrix}^{-1} \begin{pmatrix} 1 & \kappa_e \\ \kappa_e & 1 \end{pmatrix} \boldsymbol{a} = \frac{\omega^2}{\omega_0^2} \boldsymbol{a} \tag{2.3.16}$$

We have used the fact that $\langle \boldsymbol{E}_0 \boldsymbol{E}_0 \rangle_0 = \langle \boldsymbol{B}_0 \boldsymbol{B}_0 \rangle_0$, which corresponds to the resonance condition of the uncoupled resonator. The two resonance frequencies are given by

$$\omega_\pm = \sqrt{\frac{1 \pm \kappa_e}{1 \pm \kappa_m}} \omega_0 \tag{2.3.17}$$

Figure 2.10 shows the evolution of κ_e, κ_m and $\omega_\pm$ as a function of the distance d between two spiral resonators. The electric coupling decays more rapidly than the magnetic coupling which dominates at large distances. This is due to the fact that the spiral is a magnetic dipole and a higher order electric multipole. The resonance frequencies match well the predictions of the admittance model as long as $d > 30\,\mu\mathrm{m}$. For shorter distances, the approximation that the total field is a linear combination of the fields of two uncoupled resonators is not valid.

2.3.3 Comparison to the admittance model

We now compare the predictions of the two models for the band structure of the two lattices that are measured in chapter 4 and 5. The band structure of the CMT model is obtained by diagonalizing $\Omega G^{-1}(\mathbf{k})\Omega D(\mathbf{k})$ and taking the square root of the eigenvalues. We have checked that the first excited mode at 14 GHz does not influence the band structure of the first two bands. We therefore restrict the number of orbitals to one per site. The matrix to

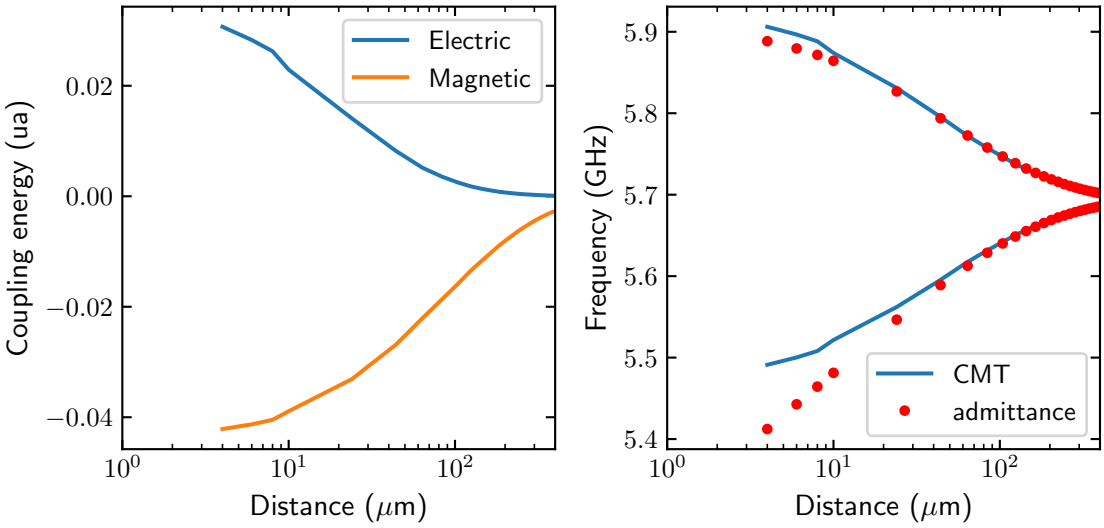

Figure 2.10: Coupling between two spirals as predicted by the CMT model. The left plot shows the evolution of the electric and magnetic coupling constants as a function of the distance d between the resonators. The right plot compares the predicted resonance frequencies by the CMT and the admittance model. The CMT model is valid in the region $d > 30\,\mu$m.

diagonalize is a 2×2 matrix, where the two components correspond to the A and B sites of the honeycomb lattice.

If we suppose that the overlap integrals are isotropic, we can obtain an analytic formula for the band structure by following the same calculation as in the first chapter. The $D(\mathbf{k})$ and $G(\mathbf{k})$ matrices are given by

$$D(\mathbf{k}) = \varepsilon_0 \begin{pmatrix} 1 + f_{2,e}(\mathbf{k}) & f_{1,e}(\mathbf{k}) + f_{3,e}(\mathbf{k}) \\ f^*_{1,e}(\mathbf{k}) + f^*_{3,e}(\mathbf{k}) & 1 + f_{2,e}(\mathbf{k}) \end{pmatrix} \tag{2.3.18}$$

$$G(\mathbf{k}) = \varepsilon_0 \begin{pmatrix} 1 + f_{2,m}(\mathbf{k}) & f_{1,m}(\mathbf{k}) + f_{3,m}(\mathbf{k}) \\ f^*_{1,m}(\mathbf{k}) + f^*_{3,m}(\mathbf{k}) & 1 + f_{2,m}(\mathbf{k}) \end{pmatrix} \tag{2.3.19}$$

where $\varepsilon_0 = \langle \boldsymbol{E}_0 \boldsymbol{E}_0 \rangle_0 = \langle \boldsymbol{B}_0 \boldsymbol{B}_0 \rangle_0$ and the $f_{i,e}$ and $f_{i,m}$ functions are defined as in (1.1.11). The coupling t_i is replaced by the corresponding overlap integral of the electric (magnetic) field normalized by ε_0 in the case of the $f_{i,e}$ ($f_{i,m}$) function. The two matrices $D(\mathbf{k})$ and $G(\mathbf{k})$ are diagonal in the same basis with eigenvalues $1 + f_{2,\alpha}(\mathbf{k}) \pm |f_{1,\alpha}(\mathbf{k}) + f_{3,\alpha}(\mathbf{k})|$ where $\alpha = e, m$. The band structure is therefore given by

$$\omega_\pm = \sqrt{\frac{1 + f_{2,e}(\mathbf{k}) \pm |f_{1,e}(\mathbf{k}) + f_{3,e}(\mathbf{k})|}{1 + f_{2,m}(\mathbf{k}) \pm |f_{1,m}(\mathbf{k}) + f_{3,m}(\mathbf{k})|}}\, \omega_0 \tag{2.3.20}$$

In the weak coupling limit and considering only NN and NNN couplings, we recover the band structure of the tight-binding model (1.1.12). The coupling t_i are given by the half difference of the corresponding electric and magnetic couplings. For example, in the nearest-neighbor approximation, we obtain

$$\omega_\pm = \sqrt{\frac{1 \pm \kappa_e \tilde{f}_1(\mathbf{k})}{1 \pm \kappa_m \tilde{f}_1(\mathbf{k})}}\, \omega_0 \simeq \left(1 \pm \frac{\kappa_e - \kappa_m}{2} \tilde{f}_1(\mathbf{k})\right) \omega_0 \tag{2.3.21}$$

where $\tilde{f}_1(\mathbf{k}) = |1 + e^{i\mathbf{k}\cdot\boldsymbol{a}_1} + e^{i\mathbf{k}\cdot\boldsymbol{a}_2}|$.

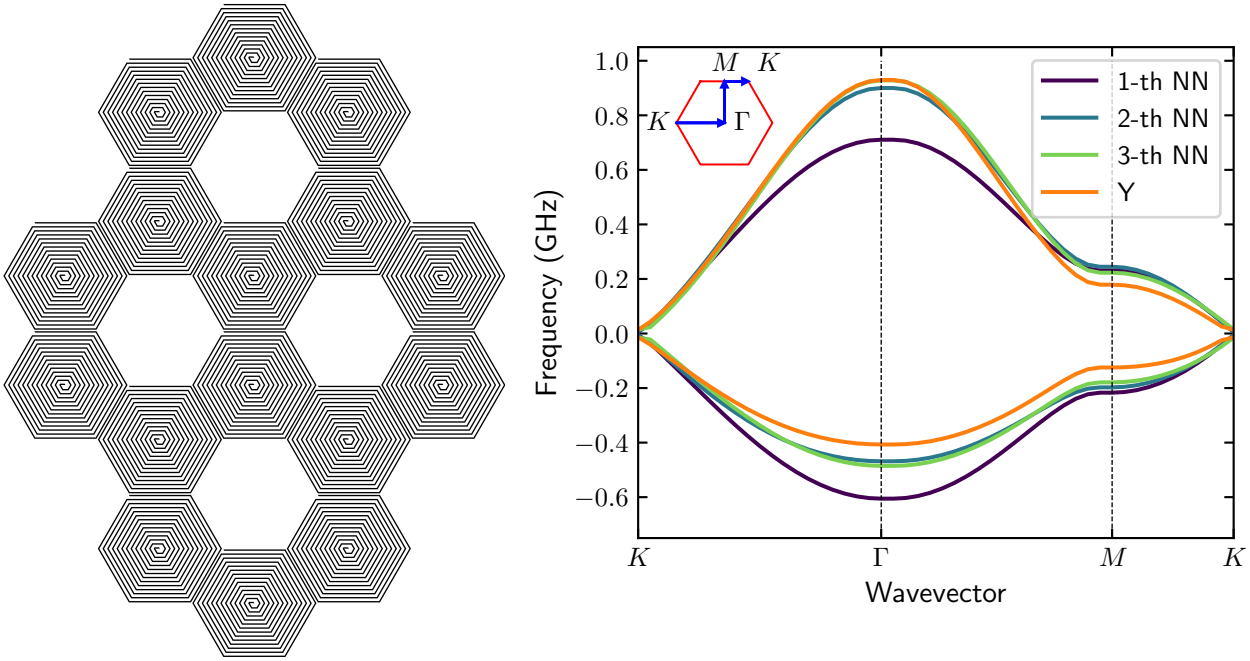

Figure 2.11: Band structure of a strongly coupled honeycomb lattice as realized in chapter 4. The admittance model corresponds to the 3 port model with 16 resonators as shown in figure 2.8. We expect that this model is an accurate simulation of the lattice. We compare it to the predictions of the CMT model for different coupling ranges. The agreement is not perfect because the coupling is too strong for the CMT model to be valid.

In our numerical simulation, we take into account the coupling anisotropy and we numerically diagonalize $\Omega G^{-1}(\mathbf{k})\Omega D(\mathbf{k})$ for each $\mathbf{k}$. Figure 2.11 shows the comparison of the two models for the strongly coupled honeycomb lattice that is measured in chapter 4. The distance d is only 5 µm, which is outside the validity regime of the CMT model. As expected, the two models lead to slightly different band structures. In chapter 5, we use a different lattice with less coupling ($d = 35$ µm) and with two inequivalent A and B sites to realize a Semenoff insulator. Figure 2.12 shows the lattice geometry (more details can be found in chapter 5), and the comparison of the two models. Because d is large enough, the models match very well up to an offset, which is removed in the plot.

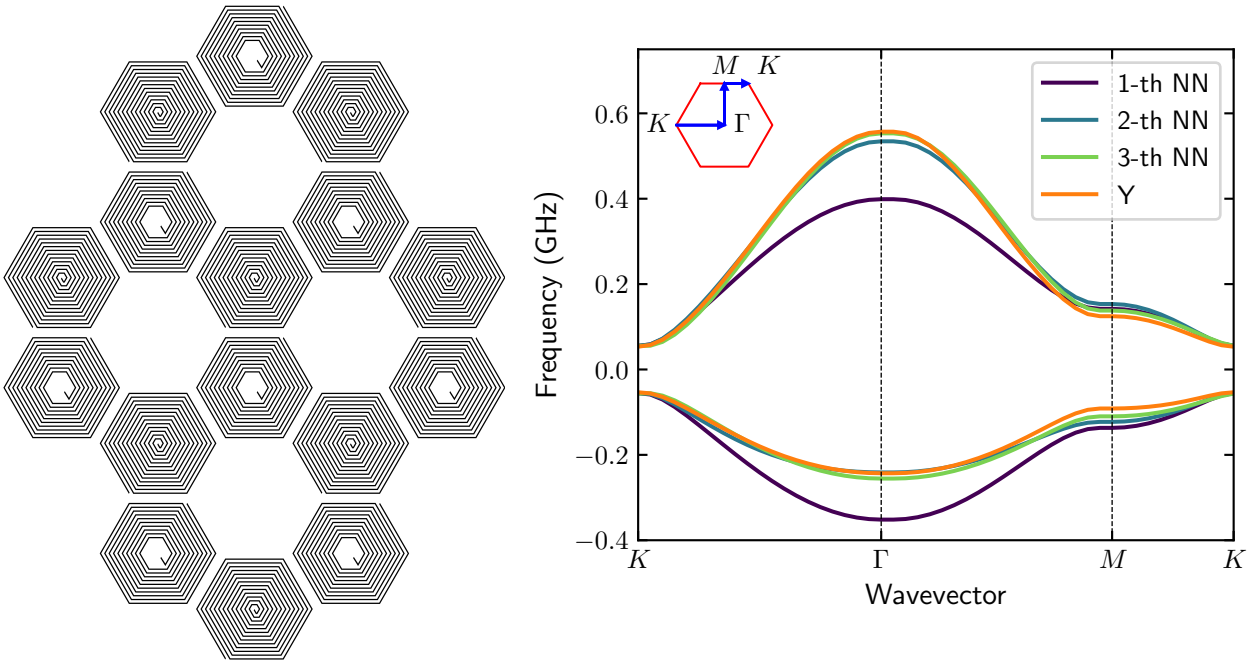

Figure 2.12: Band structure of a Semenoff insulator as realized in chapter 5. The admittance model corresponds to a 2 port model with 16 resonators. We compare it to the predictions of the CMT model for different coupling ranges. When we include NNNN coupling, both models perfectly match up to a global offset that is here removed.

Chapter 3

Mode imaging using laser scanning microscopy

Contents

In order to probe the spatial dependence of the mode wavefunctions in lattices of superconducting resonators, two different approaches have been considered. For small 1D lattices, it is possible to couple every sites to a transmission line and to measure directly the amplitude of the mode on every site [18, 20]. This becomes impractical in large chains or in 2D lattices. In [77], Underwood et al. used a piezo actuator to move a small piece of dielectric across a 2D lattice of CPW resonators. The dielectric introduces a local defect corresponding to a shift of the resonance frequency of the site below the dielectric. Therefore the variation of the resonance frequency of a lattice mode as a function of the defect position leads to a map of the mode wavefunction. In this chapter we present a new method relying on the same principle but where the defect is created by a laser spot. This laser scanning microscopy method (LSM) has been previously used to map the wavefunction of resonant modes of single superconducting resonators [53]. In the first section, we present the principle of the measurement. We then show the two optical setups that we used to obtain an homogeneous and intensity constant laser spot across the sample. Finally we characterize the lattice response to the laser light. In particular, we identify the regime of laser intensity where the response is linear and present the different protocols used to obtain the mode images shown in chapters 4 and 5.

3.1 Principle of laser scanning microscopy

Laser scanning microscopy was first developed to optically probe the spatial profile of microwave frequency superconducting currents [52, 53, 78] in a resonant structure. Figure 3.1 shows the principle of the measurement. A Vector Network Analyzer (VNA) is used to monitor the change in transmission induced by the laser as a function of position. As shown in [53], the main effect of the light is to locally increase the resistivity of the superconducting material and thus to decrease the microwave transmission. In this section, we show how this method can be adapted to obtain the weights of a lattice mode on each site of the lattice.

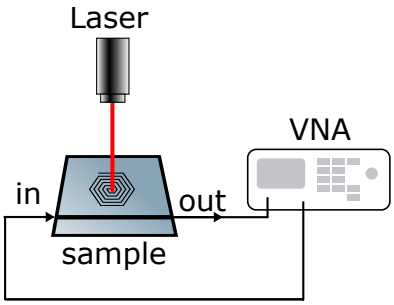

Figure 3.1: Principle of laser scanning microscopy. A laser is used ad a spatial probe of the superconducting circuit which is measured in transmission at the same time. Usually, the microwave generator and detector are a Vector network analyzer (VNA). The variation of transmission as a function of the laser position leads to a map of the resonant mode.

Close to a resonance, the transmission between two ports can be approximated by a Lorentzian function:

$$S_{21}[\delta] = \frac{\kappa}{\delta + i(\gamma_i + \gamma_l + \kappa)} \tag{3.1.1}$$

where δ is the detuning to the resonance, κ is the loss rate to the transmission line, γ_i is the intrinsic loss rate and γ_l the added loss due to the laser. Considering that the laser spot is a Gaussian of waist w centered at position $\mathbf{r}_l$, the model of Zhuravel et al. [53] leads to the following expression for γ_l as a function of the laser position:

$$\gamma_l(\mathbf{r}_l) = \int \rho_l \exp\left(-\frac{2\left(\mathbf{r}-\mathbf{r}_l\right)^2}{w^2}\right) |\boldsymbol{j}(\mathbf{r})|^2 \mathrm{d}\mathbf{r} \times E^{-1} \tag{3.1.2}$$

where ρ_l is the sheet resistance induced by the laser at the center of the spot, $\boldsymbol{j}$ is the current density of the mode and E is the total energy stored in the mode. Figure 3.2 shows $\gamma_l(\mathbf{r}_l)$ for different laser waists and an experimental image taken with a waist of 60 µm. The measurement shows the same ringlike structure than the simulation. This qualitatively confirms that the laser mostly probes the current distribution.

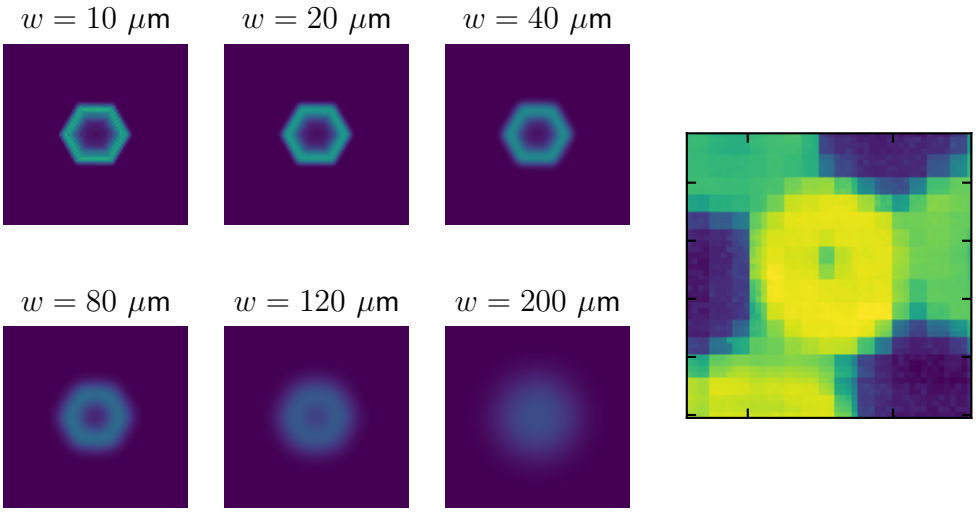

Figure 3.2: Convolution of the current distribution $|j(\mathbf{r})|^2$ of a spiral resonator with the shape of the laser spot. For small laser spot, we can distinguish the structure of the spiral. When the size of the spot is increased, this structure is blurred. For large spot, the hexagonal shape of the resonator disappears. The right image shows the measured loss rate for a spiral in a lattice, the image is qualitatively similar to the one computed on the left.

The current distribution can be expanded as:

$$\boldsymbol{j}(\mathbf{r}) = \sum_i \Psi(\mathbf{r}_i)\boldsymbol{j}_0(\mathbf{r}-\mathbf{r}_i) \tag{3.1.3}$$

where $\boldsymbol{j}_0$ is the current distribution of the orbital of the mode and $\Psi(\mathbf{r}_i)$ is the mode amplitude on site i at position $\mathbf{r}_i$. The loss induced by the laser can be rewritten as:

$$\gamma_l(\mathbf{r}_l) = \sum_i |\Psi(\mathbf{r}_i)|^2 \int \rho_l \exp\left(-\frac{2\left(\mathbf{r}+\mathbf{r}_i-\mathbf{r}_l\right)^2}{w^2}\right) |\boldsymbol{j}_0(\mathbf{r})|^2 \mathrm{d}\mathbf{r} \times E^{-1} \tag{3.1.4}$$

In order to retrieve the weight $|\Psi(\mathbf{r}_i)|^2$, we average γ_l over a region corresponding to the site i:

$$\langle \gamma_l \rangle_i = \frac{1}{M} \sum_{j=1}^{M} \gamma_l(\mathbf{r}_i + \delta\mathbf{r}_j) \times E^{-1} \tag{3.1.5}$$

$$\simeq |\Psi(\mathbf{r}_i)|^2 \rho_l \left[\frac{1}{M} \sum_{j=1}^{M} \int \exp\left(-\frac{2\left(\mathbf{r} + \delta\mathbf{r}_i\right)^2}{w^2} \right) |\boldsymbol{j}_0(\mathbf{r})|^2 \mathrm{d}\mathbf{r} \right] \times E^{-1} \tag{3.1.6}$$

Here, we suppose that the overlap of the Gaussian spot centered at $\mathbf{r}_i + \delta\mathbf{r}_i$ with the current distribution of the neighboring sites is negligible. The number of positions M varies between 6 and 200 points depending on the scan method.

3.2 Optical and microwave setups

Our lattices are made of niobium (Nb) which has a critical temperature $T_c = 9\,\mathrm{K}$. This high critical temperature allows us to operate on the 1 K stage of the Hexadry 400 dilution fridge. In this section, we present how we implement the laser scanning microscopy by reviewing the two optical and microwave setups used in this thesis. We will refer to these setup as **setup A** and **setup B** in the rest of the manuscript. For each setup, we have characterized the homogeneity of the laser spot over the sample area.

3.2.1 Setup A

The optical setup must focus a laser spot on the sample which is clamped to the 1 K stage of the dilution fridge. The 1 K plate is separated from the top of the fridge by 606 mm. The laser goes through a sealed optical windows and three lenses that are fixed in a cage system (see figure 3.3). The first two lenses ($f' = 100\,\mathrm{mm}$) form a telescope with an optical magnification of 1. The last lens is positioned at $f'_3 = 100\,\mathrm{mm}$ to refocus the beam on the sample. For a sample size of $d = 8\,\mathrm{mm}$, the maximum tilt angle of the laser is given by $\theta_M = \arctan\left(d/(2f'_3)\right) = 2.3°$. The two tilt angles are controlled by two motors mounted on a mirror mount on which the laser is fixed. Pictures of the setup are shown in figure 3.4. The

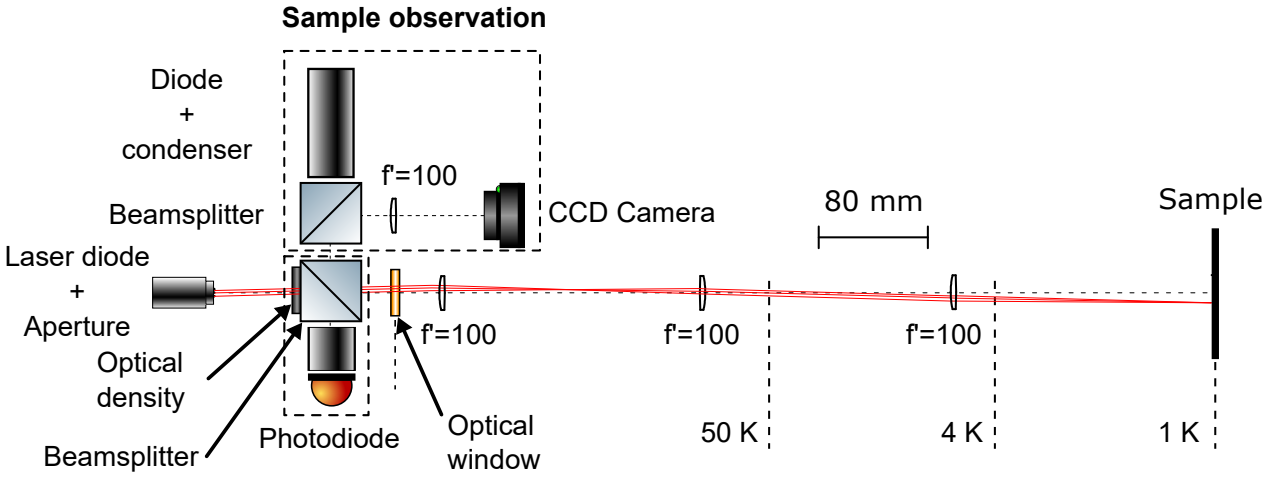

Figure 3.3: Schematic view of the optical **setup A**. The 8:92 beamsplitter and the photodiode are used to measure the intensity of the laser beam and its position.

laser source is a Thorlab Laser diode CPS635F with an aperture of 1 mm diameter. In order to measure the laser intensity, the beam is separated before entering the dilution fridge with a 8:92 pellicle beamsplitter. The transmitted light goes towards the sample and the reflected light goes to a photodiode. The beam intensity can be reduced by adding optical densities between the laser diode and the beamsplitter. For the alignment of the laser spot on the sample, the sample can be illuminated by a LED and a condenser and imaged with the camera A. The position of the laser spot on the sample can be tracked during the measurement. The presence of the beamsplitter on the laser path gives rise to a gradient of laser intensity on the sample. This is due to the fact that the transmission and reflection coefficients of the beamsplitter strongly depend on the angle of incidence.

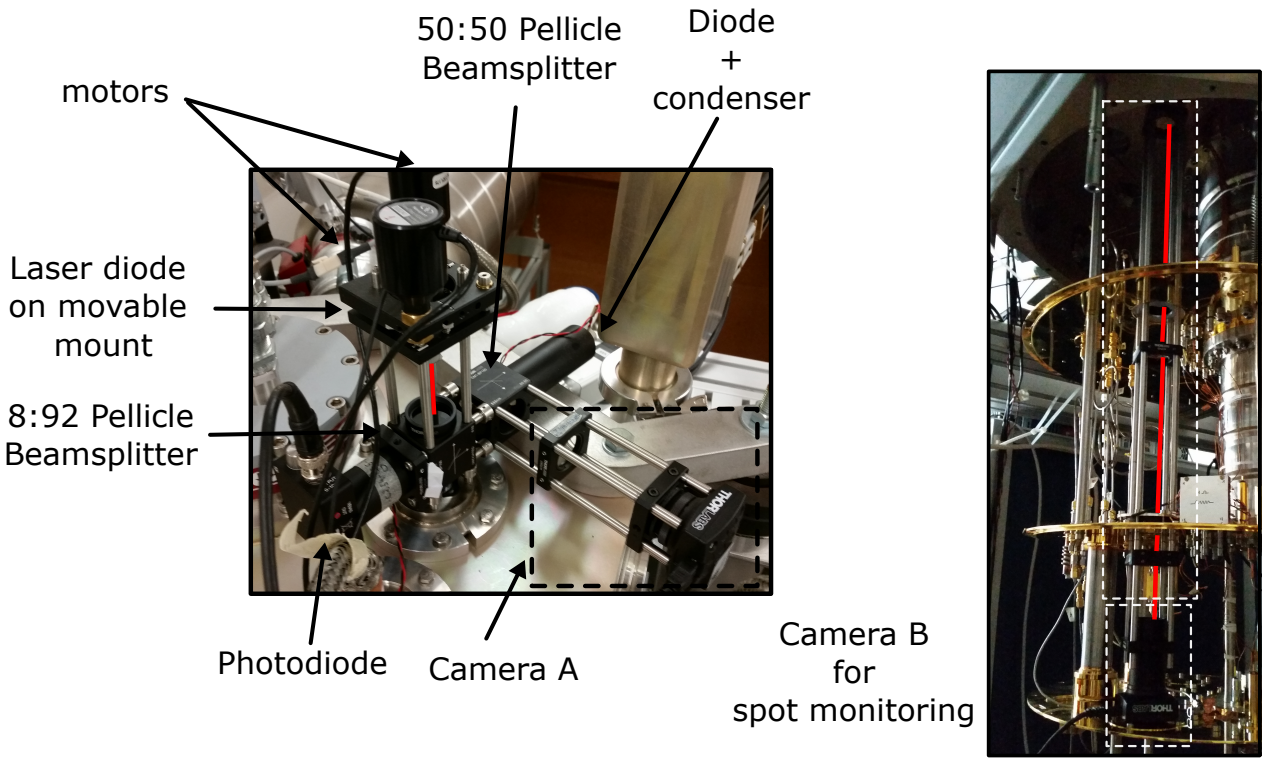

Figure 3.4: Pictures of the **Setup A**. The left picture shows the optics outside of the fridge. The LED with the condenser can illuminate homogeneously the sample. The reflected light is then collected by the camera A. The right picture shows the optical path in the dilution fridge. For spot calibration, the sample is replaced by a camera in order to measure the spot size as well as the homogeneity of the spot as a function of the position.

Homogeneity of the laser spot

To control the size of the spot on the sample, we use a camera at the sample position (camera B in figure 3.4). With this setup, we measure at room temperature the profile of the spot in order to check that the spot size and intensity are homogeneous over the area corresponding to the lattice to be measured. Figure 3.5 shows a typical profile observed with the camera. The spot is well approximated by a Gaussian:

$$I(x,y) = I_0 \exp\left(-\frac{2(x-x_0)^2}{w_x^2}\right) \exp\left(-\frac{2(y-y_0)^2}{w_y^2}\right) \tag{3.2.1}$$

In order to probe the homogeneity of the laser spot, we repeat this measurement on a grid.

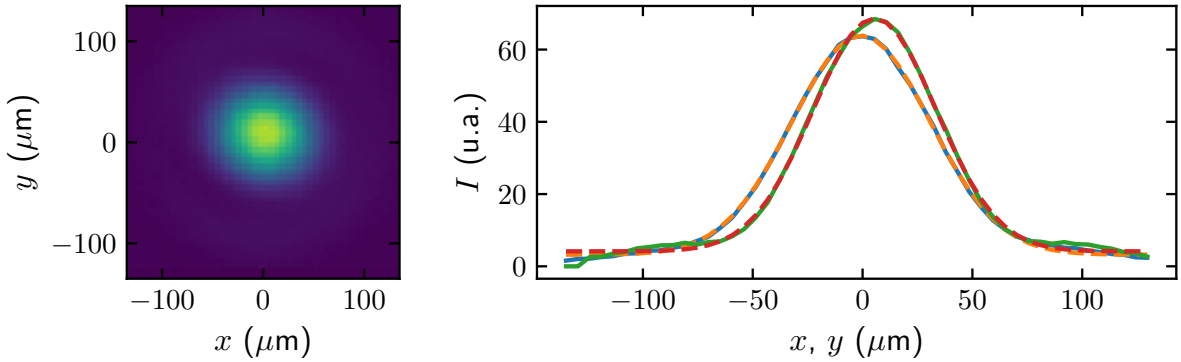

Figure 3.5: Image of the spot obtained with camera B in figure 3.4. The pixel size is 5.4 µm. The image is averaged on the x-axis and the y-axis to obtain the Gaussian profile of the spot. Here, the fit yields a waist of about 55 µm with a slight asymmetry between the two axes.

The figure 3.6 shows the evolution of the fitted waists as well as the intensity of the laser spot. The mean waist size is 59 µm and its variation is less than 2 % over the sample area. The variation of intensity is less than 5 %.

Microwave setup

The measurements are realized with a VNA directly connected to the probing transmission lines. Figure 3.7 shows the different microwave cables used with the **SetupA**. Attenuators are used to avoid parasitic reflections at the connections between cables.

3.2.2 Setup B

For the Semenoff experiment, the optical setup was modified to measure larger samples. The spot size needs to be homogeneous on a region of about 15 mm of diameter. To realize this, we use the optical setup presented in figure 3.8. Compared to **setup A** in figure 3.3, the last lens has a bigger focal $f_3' = 300$ mm. We have also changed the first lens for one with a bigger diameter. We have simplified the optical setup outside the fridge by removing the two beamsplitters.

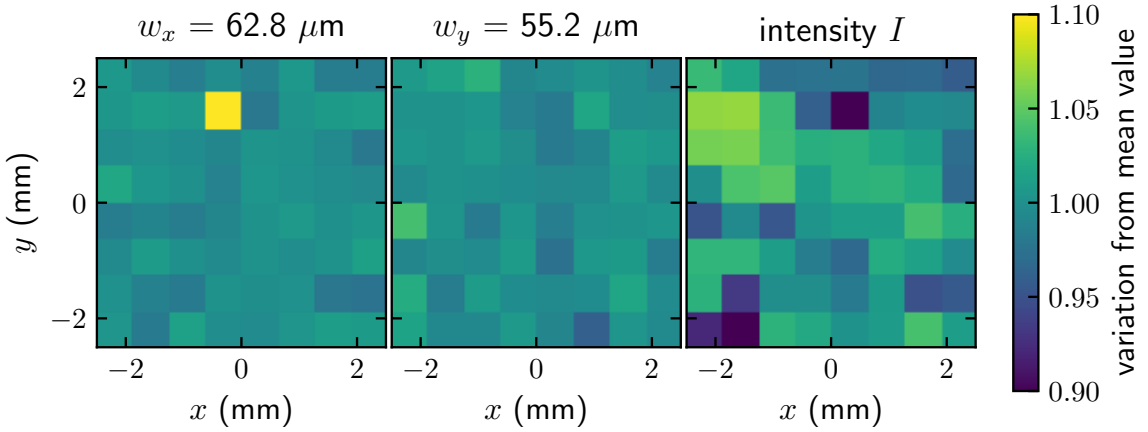

Figure 3.6: Homogeneity of the waists of the laser spot and of its intensity for the **Setup A**. The plot shows the variation of these quantities compared to their mean values. Over the whole measurement, the variation of the waists is less than 2 % and the variation of intensity is less than 5 % for this setup.

The maximum angle needed to reach the border of the sample is $\theta_M = 1.5°$. Assuming that the beam is Gaussian with an entering diameter of D (controlled by a diaphragm), its waist at the focus point of the last lens is:

$$w = \frac{2\lambda}{\pi}\frac{f_3'}{D}. \tag{3.2.2}$$

This relation holds only for the on-axis spot. For $D = 4\,\text{mm}$ and a wavelength $\lambda = 635\,\text{nm}$, this relation yields a waist of $w = 60\,\mu\text{m}$. Using the optical design program OSLO, we recover this value for the on-axis spot size. The same simulation shows that with an angle of $\theta = 1.5°$, the spot size remains the same.

Homogeneity of the laser spot

We have measured the evolution of the waist as a function of the position on the sample. The position of the spot was measured at room temperature using the same camera as before. In order to cover a larger area, the camera is fixed to a linear micrometer positioning stage. The measured waists and the intensity are shown in figure 3.10. The mean waist is 56 µm with a standard deviation of less than 1 % over a radial distance of 8 mm. The standard deviation of the intensity is less than 3 % over the same area.

Positioning accuracy

In order to check the reproducibility of the positioning of the laser spot, we use the camera at the sample level to track the spot position and loop over different spot positions every 2 s

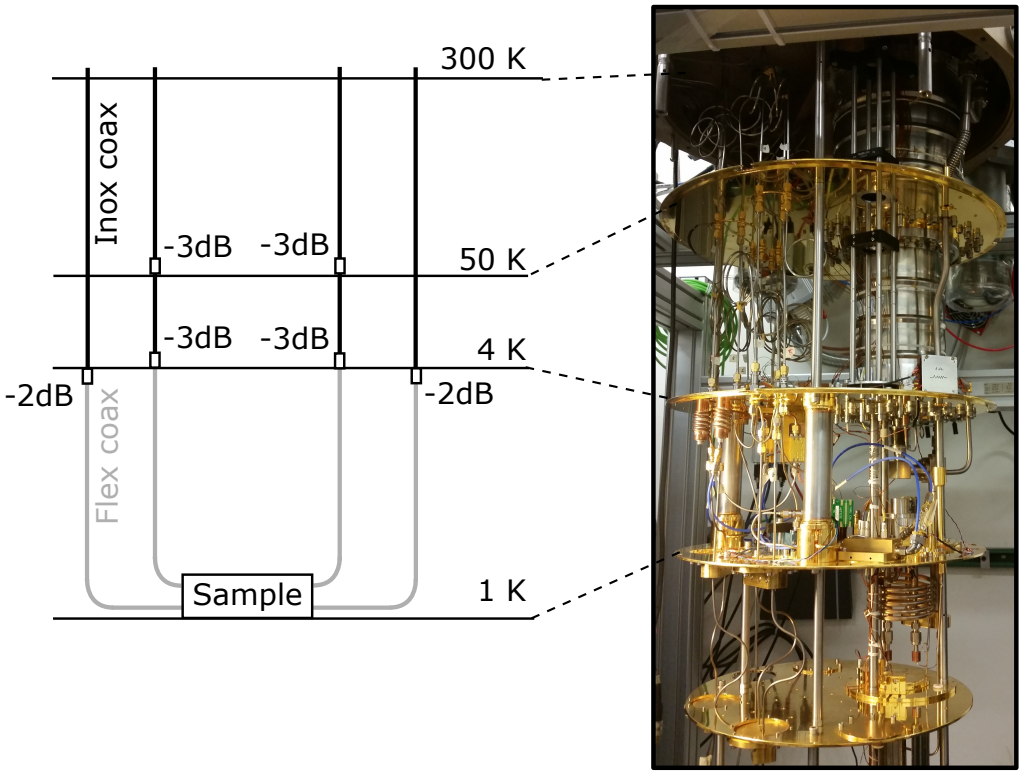

Figure 3.7: Microwave **SetupA**. The sample is clamped the 1 K stage and is connected to four transmission lines. The cables from room temperature to the 4 K stage are inox cables. The sample is connected to these cables with flexible copper coaxial cables.

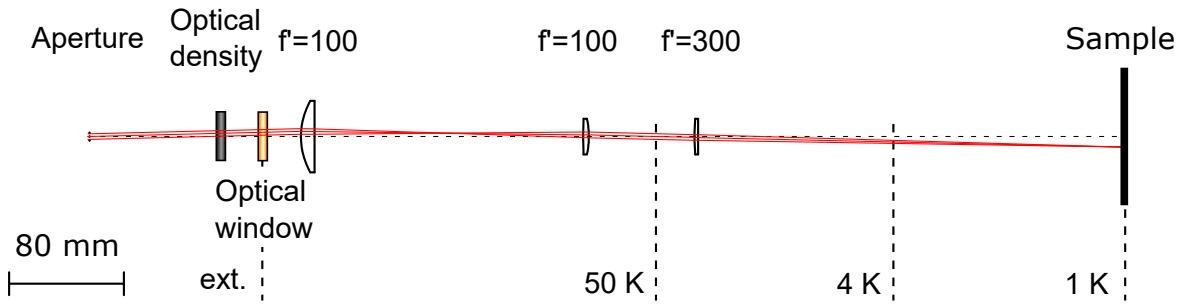

Figure 3.8: Schematic of the optical **setup B**.

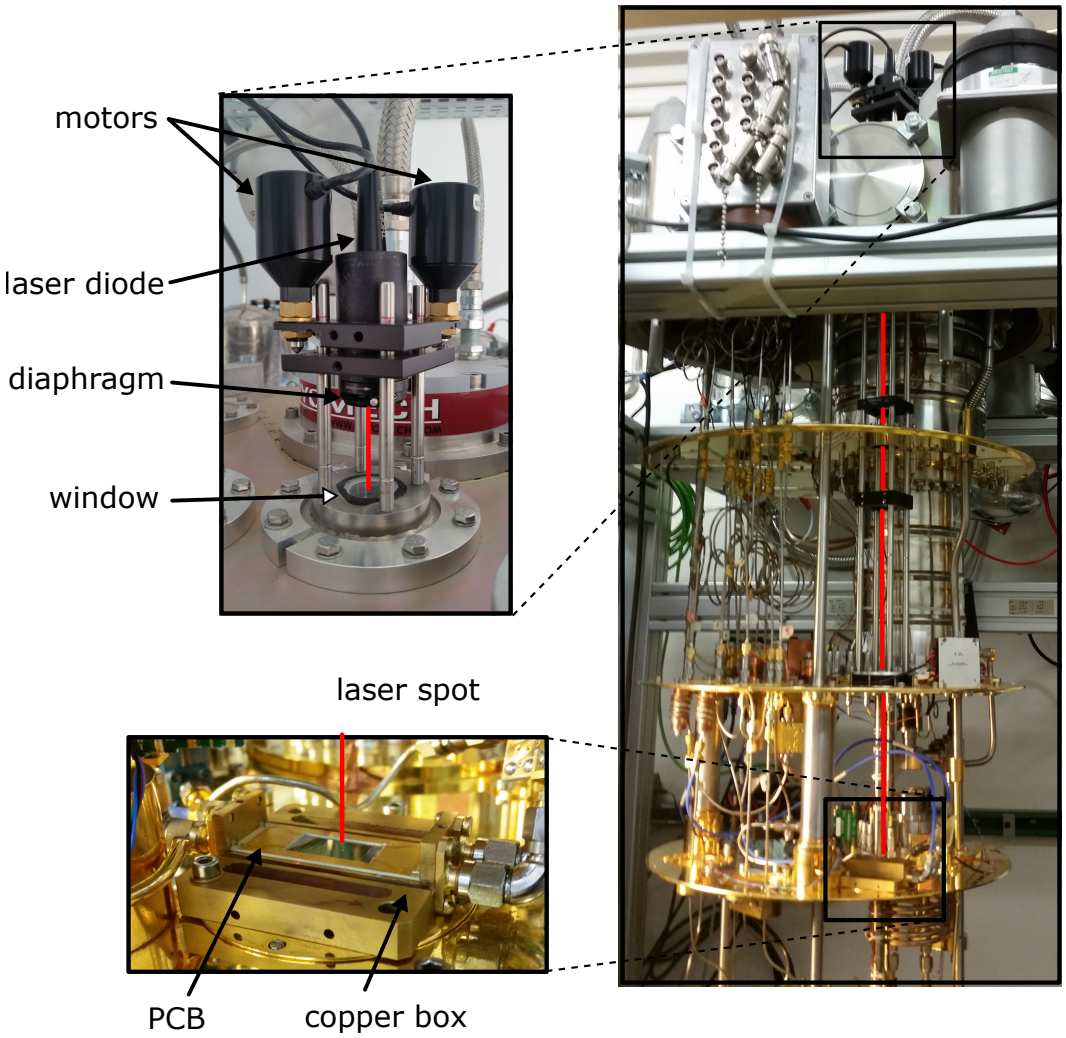

Figure 3.9: Picture of the optical **setup B** in the dilution fridge.

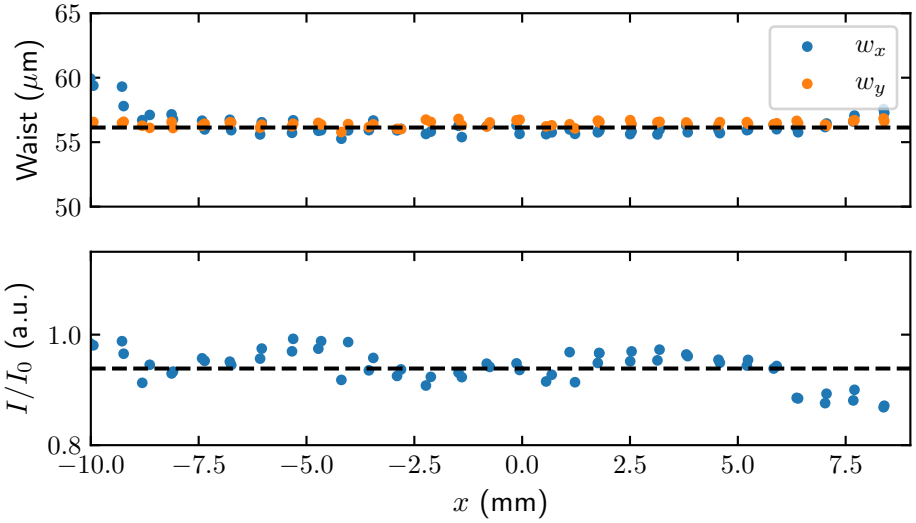

Figure 3.10: Waist and intensity variations for **Setup B**.

as in the experiment. Figure 3.11 shows the drift of the laser spot with time. The reference positions are taken at the end of the first measurement (the portion of curve at zero). This measurement shows that after a long period without moving, the motor absolute position is not accurate during a period of about 1000 moves (33 min). The drift stabilizes to a value of 11 µm with respect to a reference position. This drift is one order smaller than the size of resonators (400 µm) and should be negligible as long as the motors are not stopped for too long.

Microwave setup

The microwave setup used in this experiment is shown in figure 3.12. There are four probing points on the sample, which makes six possible transmission measurements. We connect the two ports connected to the domain wall to two cryogenic amplifiers so that we can measure edge states with a good signal/noise ratio. Two broadband (DC - 8 GHz) non-reflective GaAs SPDT switches (HMC270AMS8GE) are inserted in the setup so that we can calibrate the transmission along the domain wall. We also insert two directional couplers in order to measure the reflection spectra.

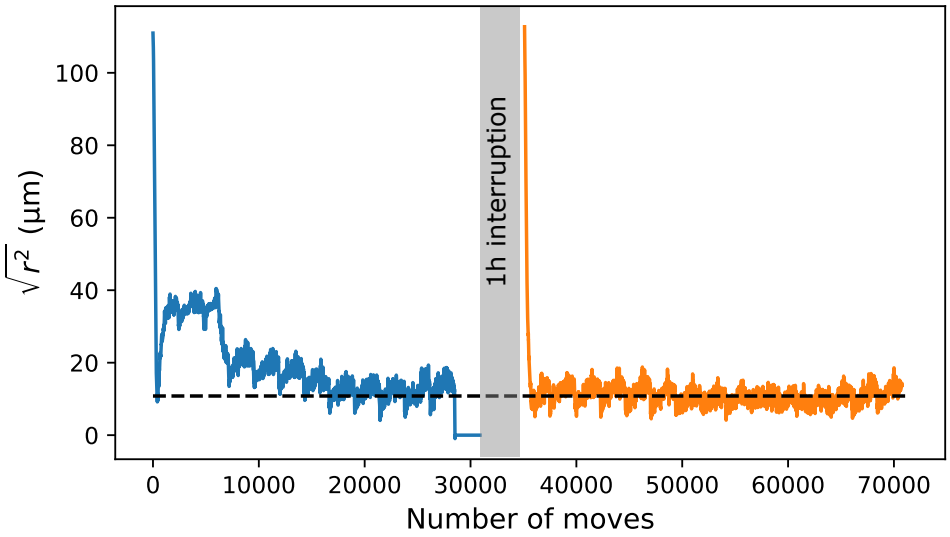

Figure 3.11: Drift of the laser spot position. The two colors represent two sets of data. The first one in blue starts after a full night without using the motor. The second set (in orange) is done 1 h after the end of the first set.

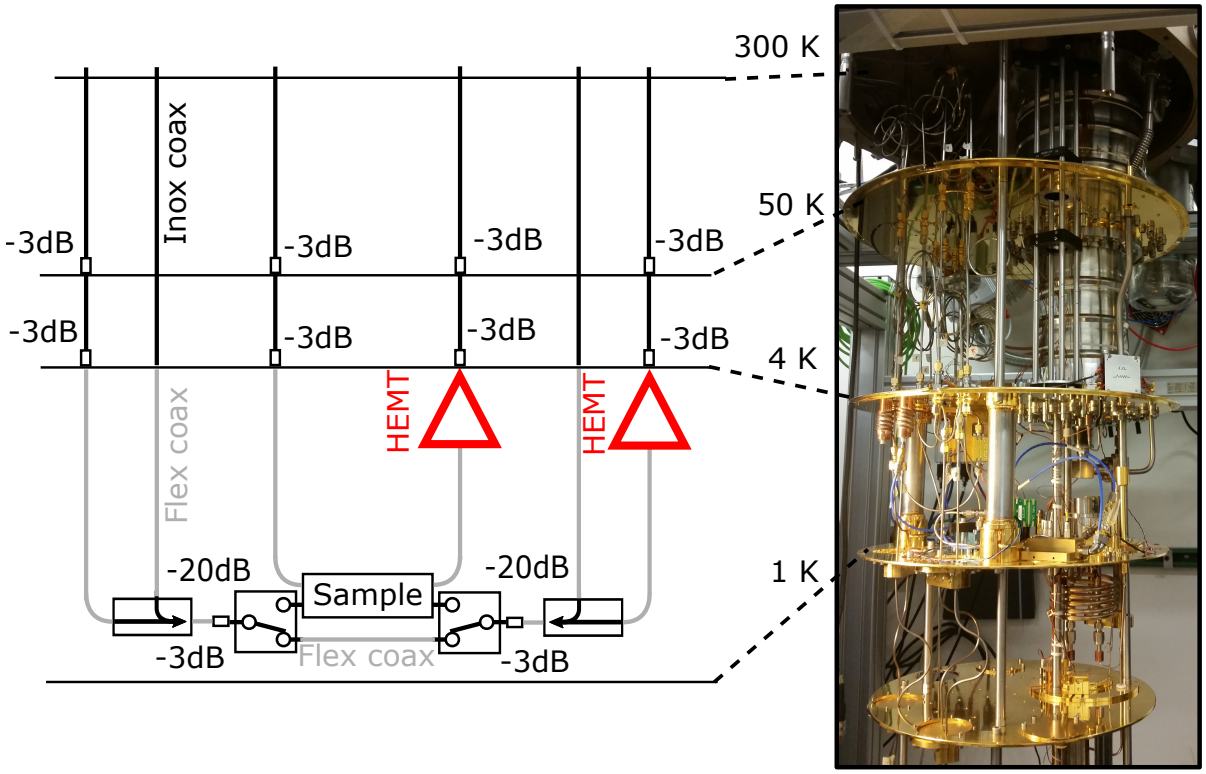

Figure 3.12: Microwave **SetupB**. Rectangles with arrows represent directional couplers from Krytar. The two switches between the sample are two broadband (DC - 8 GHz) non-reflective GaAs SPDT switches (HMC270AMS8GE). The two cryogenic amplifiers are Low Noise Factory LNF-LNC4-8C models with a noise temperature of 2 K in the 4 GHz to 8 GHz range. The sample holder and the two directional couplers are fixed to the 1 K stage of the dilution fridge.

3.3 Characterisation of the photoresponse

In this section, we characterize the photoresponse of our samples to laser light. We first show some experimental proofs for the presence of two level systems (TLS) on samples with silicon substrate. The presence of TLS is important to understand the microwave response of these samples to light. We then show how continuous and pulsed laser excitation modify in a different way the linewidth and the resonance frequency of the lattice modes as a function of laser intensity.

3.3.1 Evidences for the presence of TLS

Figure 3.13 shows the evolution of a resonance peak for the two samples **ZigzagSi** and **ZigzagSa**, which have silicon and sapphire as substrates respectively. In the case of sapphire, the resonance frequency and the quality factor increase as the temperature decreases. This is the expected behavior for superconducting resonators. The Mattis-Bardeen formula predicts that the kinetic inductance of a superconducting wire increases with decreasing temperature while the real part of the conductance decreases. In the case of the silicon wafer sample, we observe the same behavior until T reaches 3 K. Below this value the resonance frequency decreases with temperature. At the same time the quality factor keeps increasing. This behavior is usually attributed to the presence of TLS [37, 79, 80].

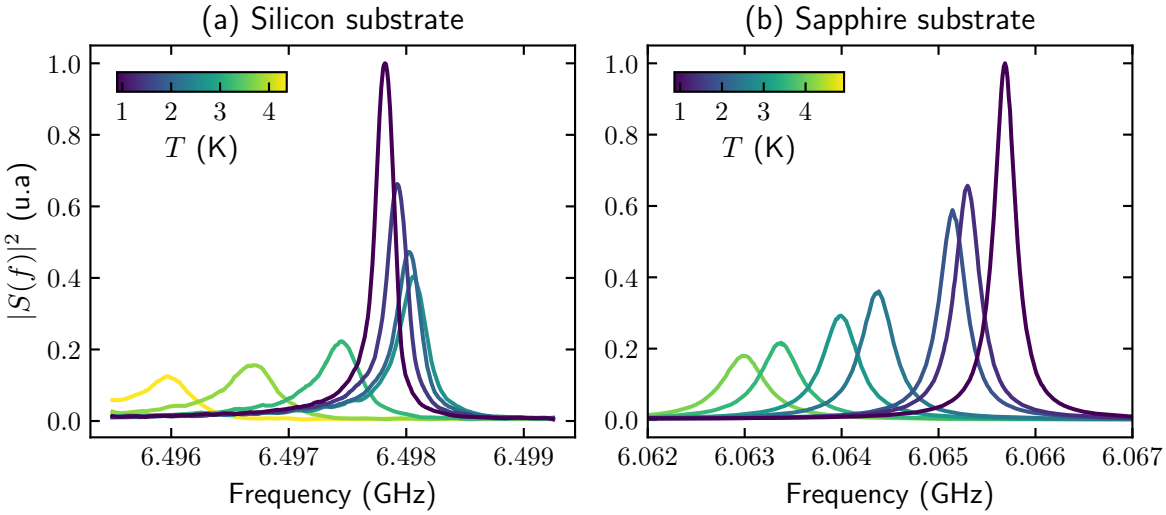

Figure 3.13: Evolution of the resonance of one mode with temperature for the **ZigzagSi** sample and the **ZigzagSa**. In both cases, the quality factor increases as the temperature decreases. But, the evolution of the resonance frequency is different for each sample. We attribute this to the presence of TLS on the silicon sample.

The presence of TLS on the silicon sample is confirmed by the evolution of the resonance as a function of microwave power as shown in figure 3.14. Increasing the power first saturates the TLS, which results in an increase of the quality factor and of the resonance frequency. At low temperature, we also observe that the quality factor passes by a maximum and decreases

again at large microwave power. For both temperatures we observe that the resonance curves become asymmetric which is characteristic of a non-linear effect. We attribute this non-linearity to the TLS but more studies would be necessary to validate this hypothesis.

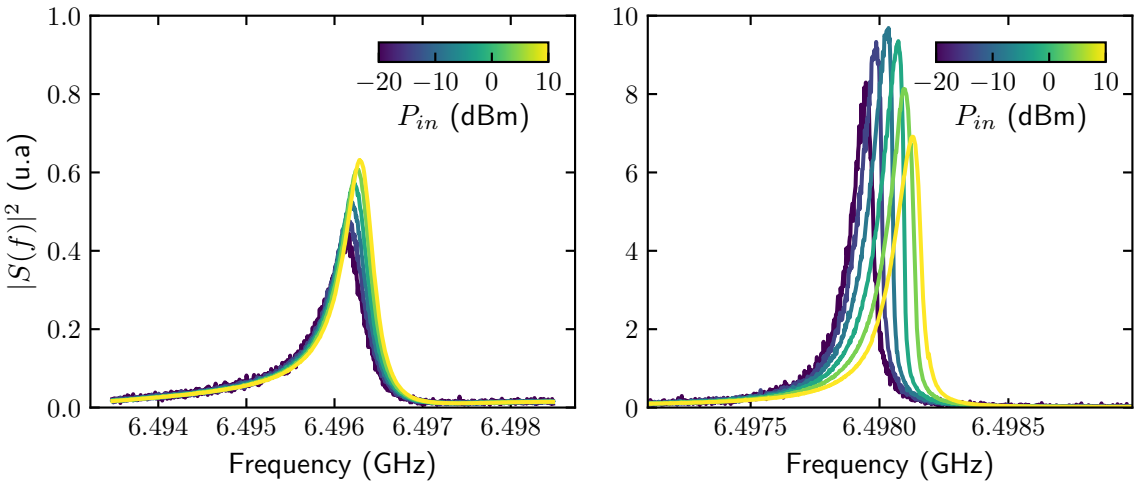

Figure 3.14: Transmission measurement of a mode at 6.498 GHz of the **zigzagSi** sample on silicon with **setup B**. The left curves are taken at 4 K and the right ones at 900 mK.

3.3.2 Continuous laser excitation

We have noticed that some silicon samples present a large photoresponse with a very slow time-scale on the order of a few seconds. This slow dynamic may be due to the presence of TLS or to the slow relaxation of charge carriers in the silicon at low temperature. Figure 3.15 shows the evolution of a resonance of the sample **ZigzagSi** for various laser intensities. We see that the effect of an increasing continuous laser intensity is similar to the one of increasing microwave power. The resonance frequency increases with intensity while the quality factor first increases, passes by a maximum and then decreases.

3.3.3 Pulsed laser excitation

In order to separate the effect of the rapid and slow photoresponses, we pulse the laser as shown in figure 3.16. The mean laser intensity is kept constant and we measure the evolution of the resonance as a function of the intensity at the maximum of the pulse. The results are shown in figure figure 3.17. We observe a different behavior than for continuous excitation. Here, the resonance frequency is not affected by the laser and the quality factor is monotonously decreasing with the laser intensity. The bandwidth of the laser diode power supply is limited to 20 kHz, with this bandwidth we were not able to see any time dependence in the photoresponse.

Figure 3.18 shows the evolution of γ_l for two resonances with fixed laser position. We observe that both curves are proportional to each other, and that they have a linear behavior

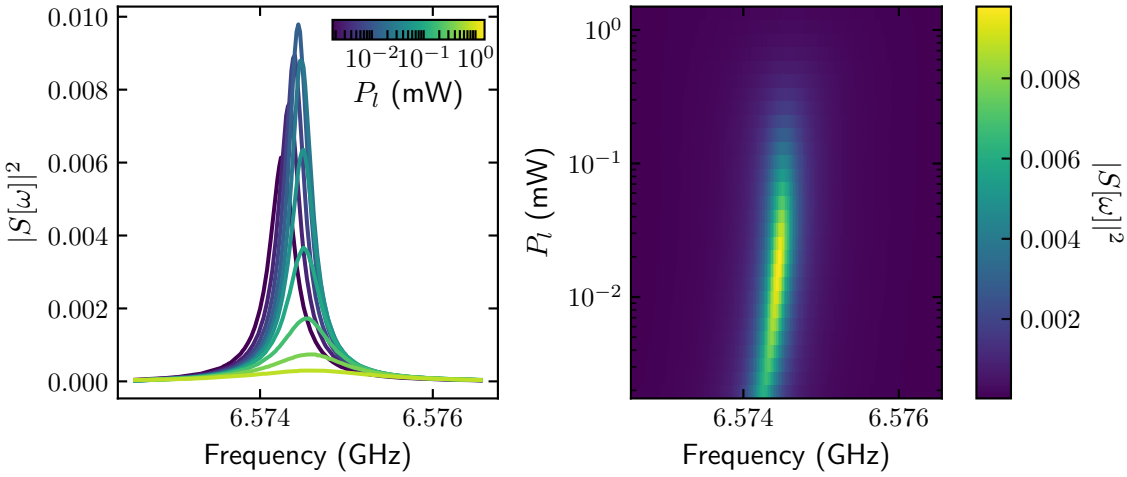

Figure 3.15: Effect of increasing continuous laser intensity on the transmission of a bulk mode of the sample **ZigzagSi**. The laser spot is localized on one bulk resonator.

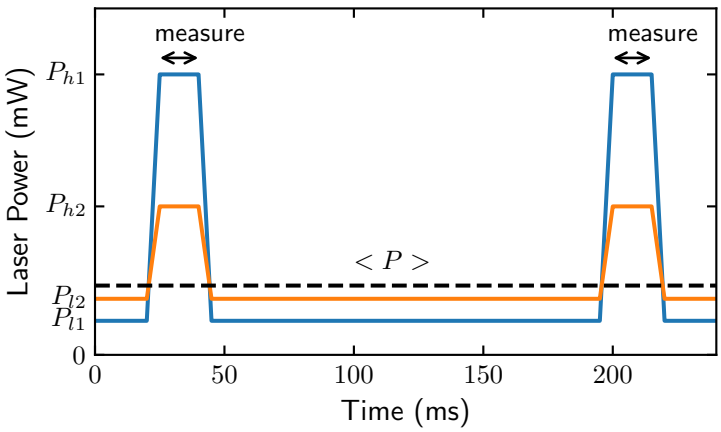

Figure 3.16: Pulse shape for the modulation of the power intensity. For a given laser power P_h, the mean value of the mean value of the power $\langle P \rangle$ is kept constant by adjusting the low value power P_l. The transmission measurement is done while the laser is set at $P = P_h$.

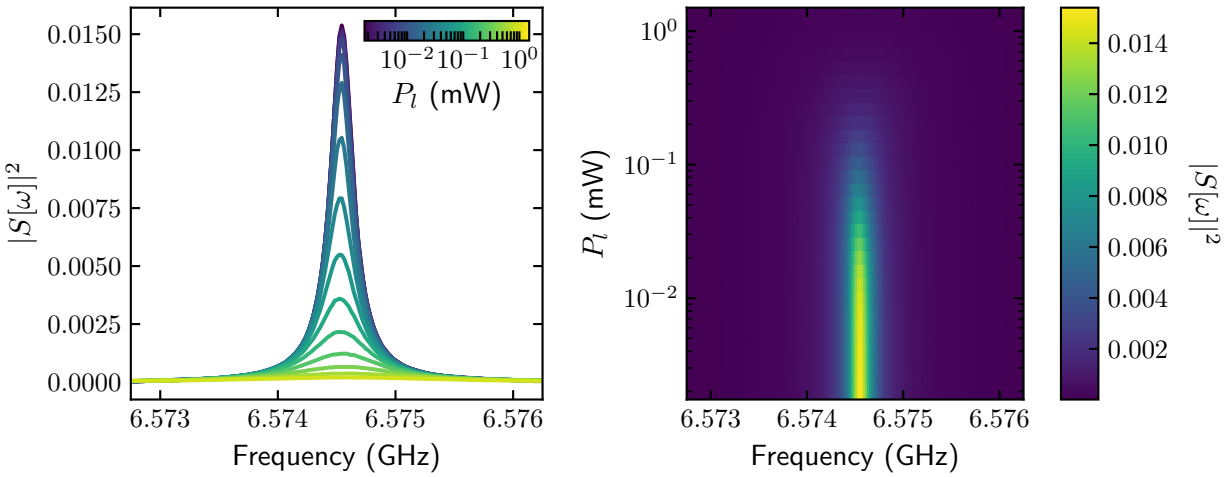

Figure 3.17: Effect of increasing pulsed laser intensity on the transmission of a bulk mode of the sample **ZigzagSi**. The laser spot is localized at the same spot as in figure 3.15. For each curve the laser power is kept constant.

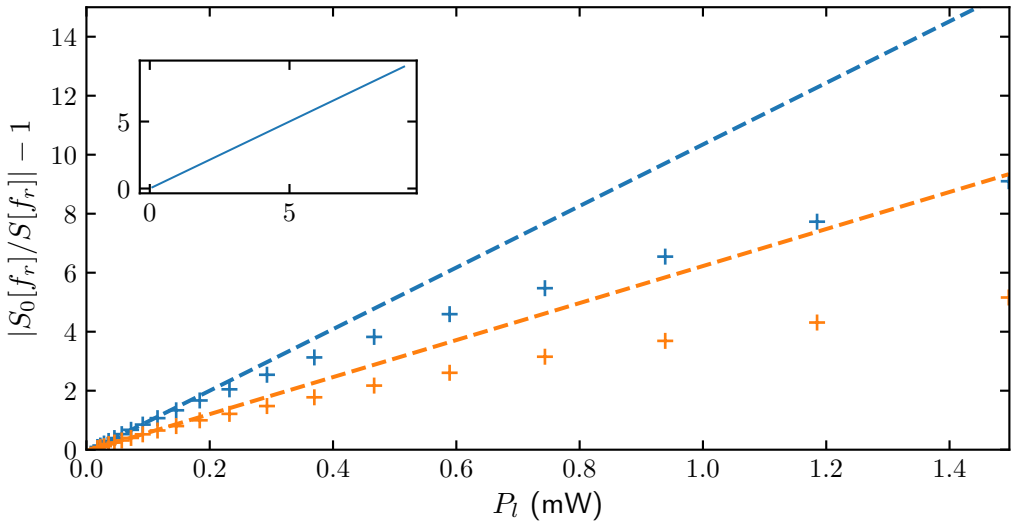

Figure 3.18: Evolution of the laser induced loss rate as a function of the laser power P_l. The loss rate is deduced from the variation of the inverse transmission at resonance. We observe a linear behavior for laser power below 200 µW. The blue curve corresponds to the data shown in figure 3.17 and the orange curve to another resonance peak keeping the laser at the same spot. The insert figure shows the proportionality between the two measurements.

for $P_l < 0.2\,\mathrm{mW}$. This suggests that the non-linear behavior is due to a non-linear variation of ρ_l as a function of P_l in equation (3.1.6) rather than a non-linear response to the weight $|\Psi(\mathbf{r}_i)|^2$. We anyway use a laser power below $0.2\,\mathrm{mW}$ during mode imaging.

3.4 Measurement protocols

In the previous section, we have shown that, for a given mode, a rapidly varying light intensity translates into a variation of the loss rate, which is proportional to the weight of the mode on the illuminated site. In order to measure the weights over all the lattice sites, we use two methods: We either scan the position of the laser continuously with a fixed frequency of the microwave excitation, or we move the laser from site to site and acquire a microwave spectrum for each laser position.

3.4.1 Continuous scanning

During such a measurement, the VNA is set at a fixed frequency of a resonance mode f_0 and the motors continuously scan the laser spot across the sample line by line. The laser is kept at a fixed intensity or is modulated to improve the signal to noise ratio. The variation of γ_l is deduced form the variation of S_{12} as a function of position. During the scan, the laser spot moves at approximately $1\,\mathrm{mm}\cdot\mathrm{s}^{-1}$, the illumination time of a single site is about 0.3 s, which is fast compared to the slow dynamics. Figure 3.19 shows a mode image obtained on the **HoneycombSi** sample with fixed laser intensity. A full image requires about 30 min of acquisition.

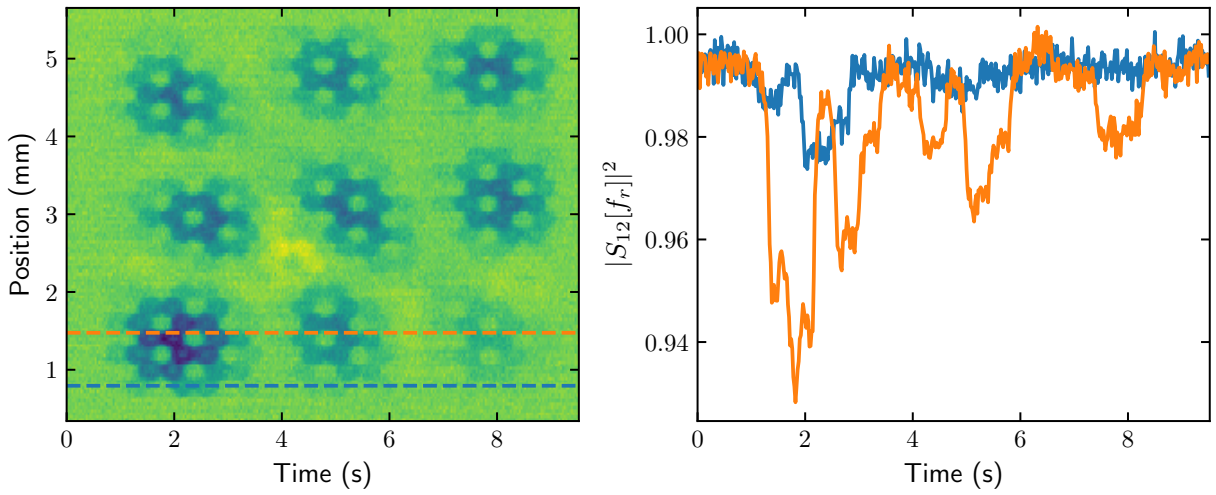

Figure 3.19: Continuous scanning at constant laser intensity of a mode of the sample **HoneycombSi**. This measurement was performed with the **setup A**. The plot on the right shows the measured transmission of the resonance corresponding to the dashed lines of the left figure.

Modulated laser intensity

For the measurement of the Semenoff samples, we modulate the laser intensity at $f_m \approx 5\,\mathrm{kHz}$ to improve the signal to noise ratio. The photoresponse is measured using the VNA set to a bandwidth of $\mathrm{BW} = 20\,\mathrm{kHz} = 4f_m$. The modulation frequency is adjusted to precisely

match this condition. The VNA time trace is digitally demodulated as shown in figure 3.20.

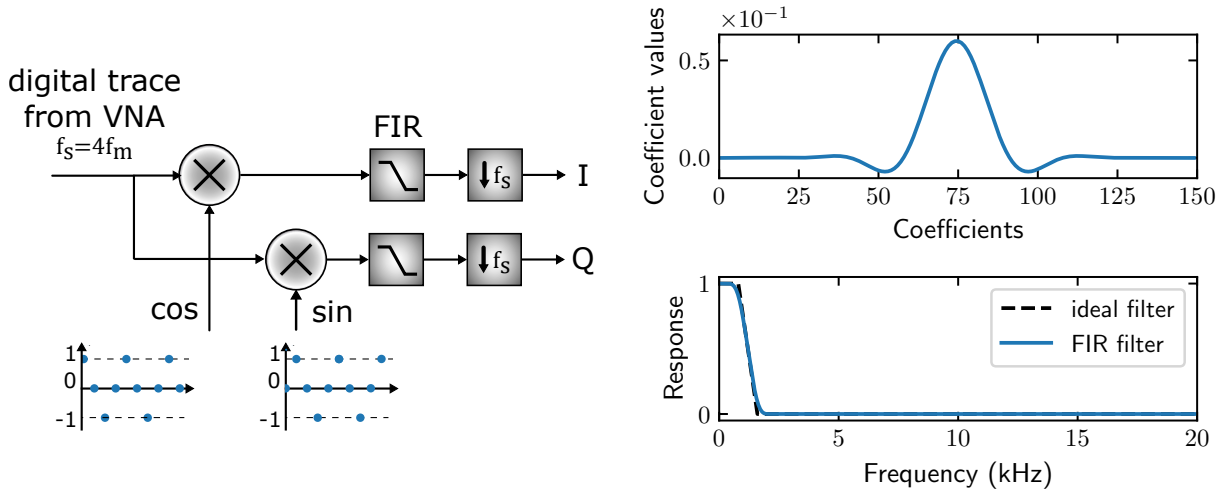

Figure 3.20: Digital IQ used to demodulate the signal acquired from the VNA. The VNA trace is first multiplied by two arrays which correspond to cos and sin functions sampled at four times their period. The two quadratures are then filtered with a low pass FIR filter (150 coefficients) with a cutoff frequency of 800 Hz. We show on the right panel the filter coefficients and its frequency response in amplitude.

3.4.2 Raster acquisition

The acquisition time of the continuous scanning method is too long to get the spatial distribution of a large number of lattice modes. Instead of continuously scanning the position of the laser, we identify the positions of the sites as shown in figure 3.22. We then choose a set of positions corresponding to a few measurement points per site (between 1 and 6). For each position we acquire a transmission spectrum from which we obtain the variation of S_{12} for many modes at the same time. For the **HoneycombSi** sample, this method was used with constant laser intensity. For the **ZigzagSi** and **ArmchairSi**, we modulated the laser intensity and demodulated each spectrum with the same method as explained above.

3.5 Failure of mode imaging on Sapphire

Figure 3.23 shows some of our attempts to image some modes with continuous laser scanning and modulated laser intensity. The different images correspond to different optical densities. We have observed that the images are blurred and that the signal to noise ratio is much worth than for silicon samples. We have not fully understood the reasons for this behavior. We suspect that one problem may come from multiple reflections of the laser inside the substrate.

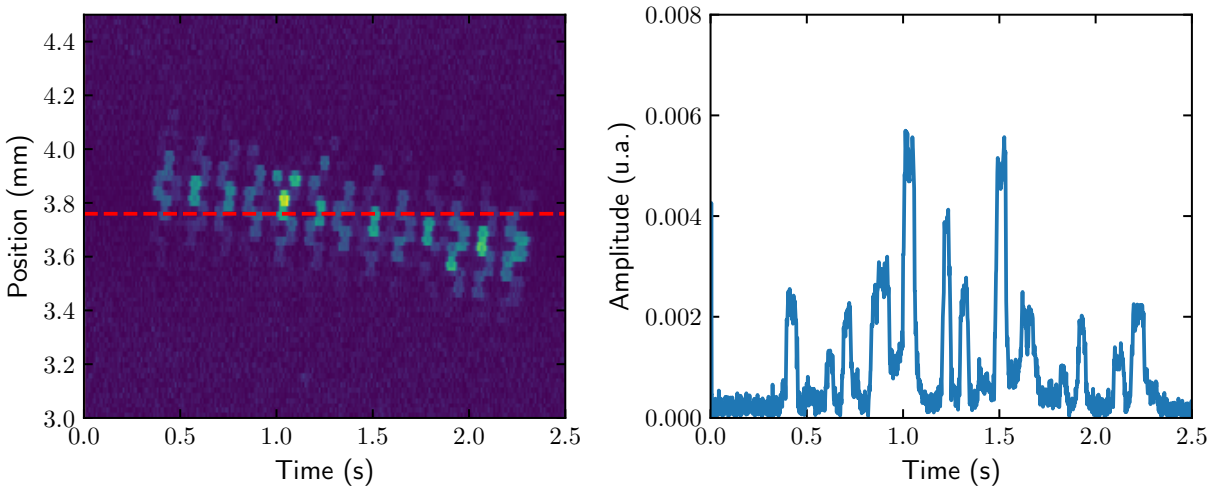

Figure 3.21: Continous scanning of an edge state of **ZigzagSI** performed with the **setup B** and modulation. The plot on the right shows the measured photoresponse along the dashed line. The signal amplitude is given by $\sqrt{|Q|^2 + |I|^2}$.

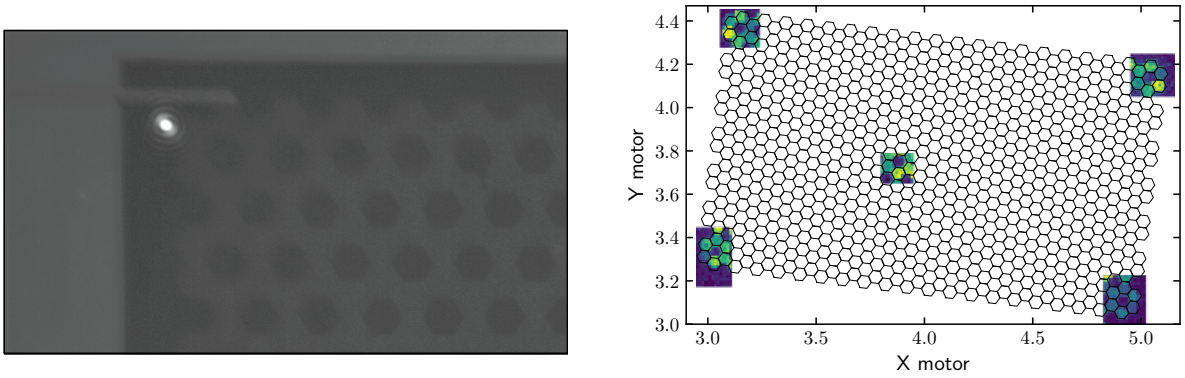

Figure 3.22: Obtaining the positions of the resonators across the lattice. For the **Setup A** on the left, the sample and the laser spot can be directly observed. For the **Setup B**, on the right, we take a fine image near the corners of the sample and in the center to calibrate the lattice positions.

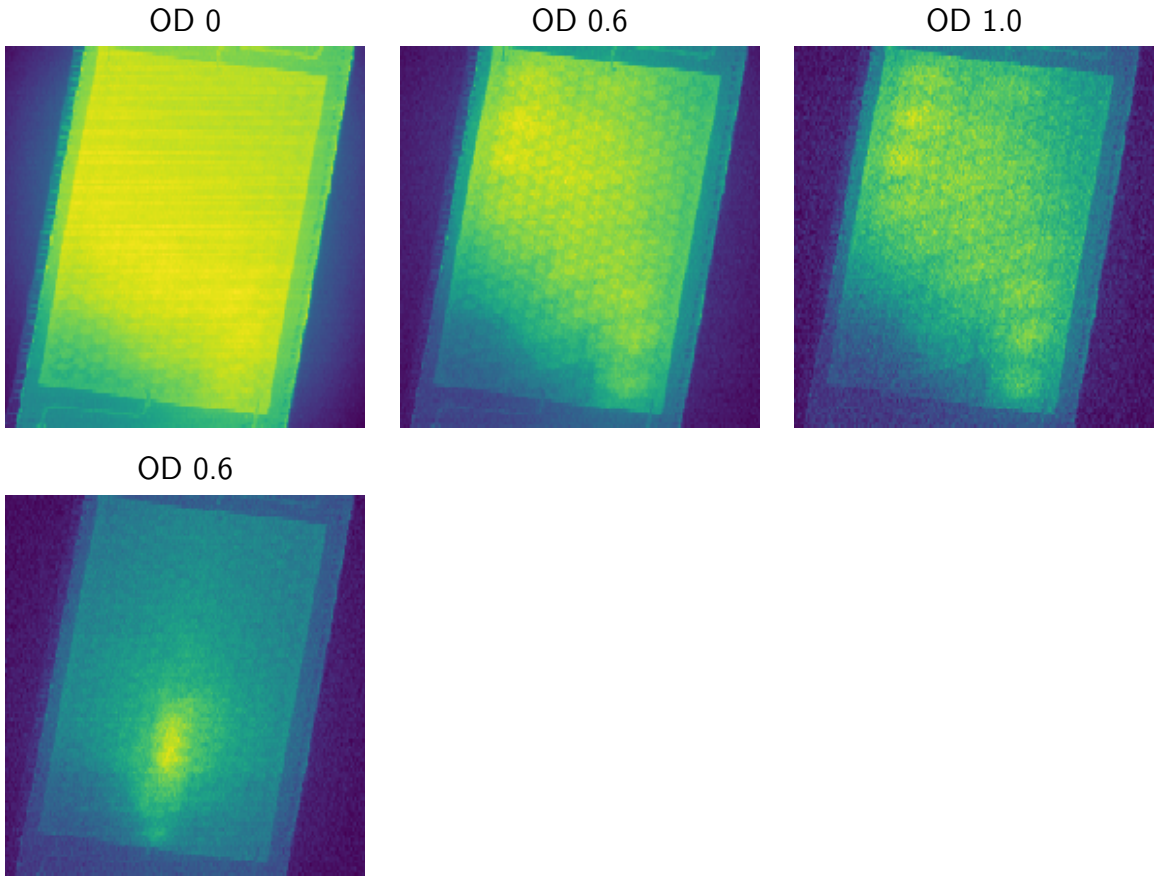

Figure 3.23: Images of two modes of a lattice on a Sapphire substrate. The top row shows the same mode imaged at different laser intensities. The bottom row shows a single image of a Semenoff edge state.

Chapter 4

Honeycomb lattice of superconducting resonators

Contents

In this chapter, we present the experimental results obtained with a honeycomb lattice of superconducting resonators. We first explain the design of the sample and then show the measured transmission spectra. We then present the results of the mode imaging using the technique detailed in chapter 3. We show how we retrieve the wavevector of the imaged modes although we only have access to the modulous of their wavefunctions across the lattice. This allows us to obtain an experimental band structure that we compare to the different models developed in chapter 2. The last section of this chapter is devoted to the characterization of the zigzag and bearded edge states that we could image. In particular, we compare their band structure and penetration lengths to the predictions obtained in section 1.2.

4.1 Design of the sample

Our lattice is made of hexagonal spirals with a typical size of 300 µm as shown in figure 4.1. The spiral length was tuned in order to have a fundamental mode of the resonator around 6 GHz. More details about the resonator properties can be found in chapter 2.

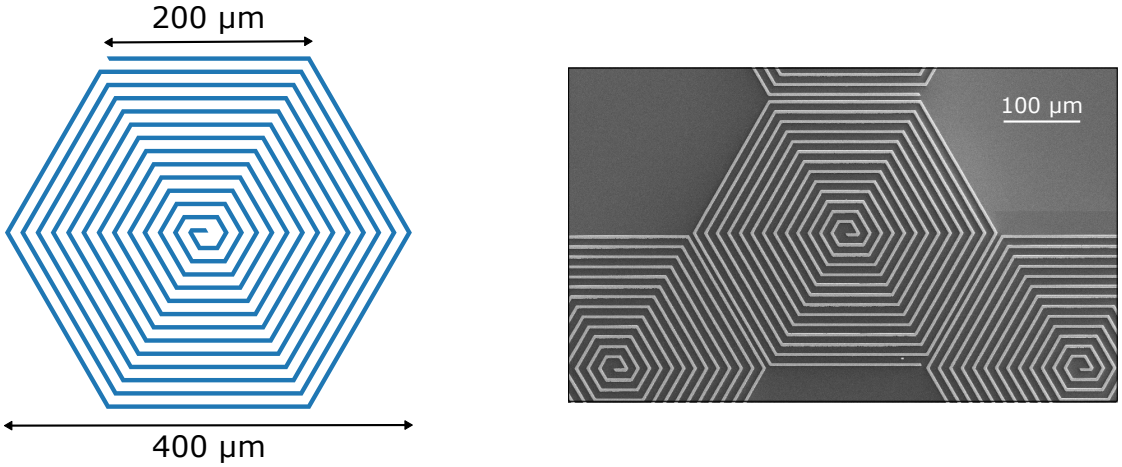

Figure 4.1: On the left, design of the spiral used for the sites of the lattice. The spiral is a 8.6 mm long wire with a width of 4.33 µm and a gap between two adjacent turns of 8.66 µm. On the right, a SEM picture of a central region of a sample realizing a honeycomb lattice.

4.1.1 Nearest-neighbor coupling

As seen in 4.1, the gap between two sites is smaller than the gap between two turns of the spiral. We made this choice to maximize the NN hopping strength in order to minimize the effect of disorder. But this complicates the modeling of the lattice because the orbital of an isolated spiral is not a good approximation to the orbital of a lattice site. The evolution of the NN coupling energy t_1 between two resonators is shown in the right curve of figure 4.2 for each of the three direction $t_{1\alpha}$, $t_{1\beta}$, $t_{1\gamma}$. The spiral breaks the invariance by rotation of $\pi/3$ around its center leading to a small anisotropy between the three directions. The NN coupling is calculated by simulating a circuit of two coupled resonators and looking at the half splitting between the two resonances. For an equal distance between spirals in each direction $d_\alpha = d_\beta = d_\gamma = 5\,\mu\text{m}$, we obtain the coupling values given in table 4.1.

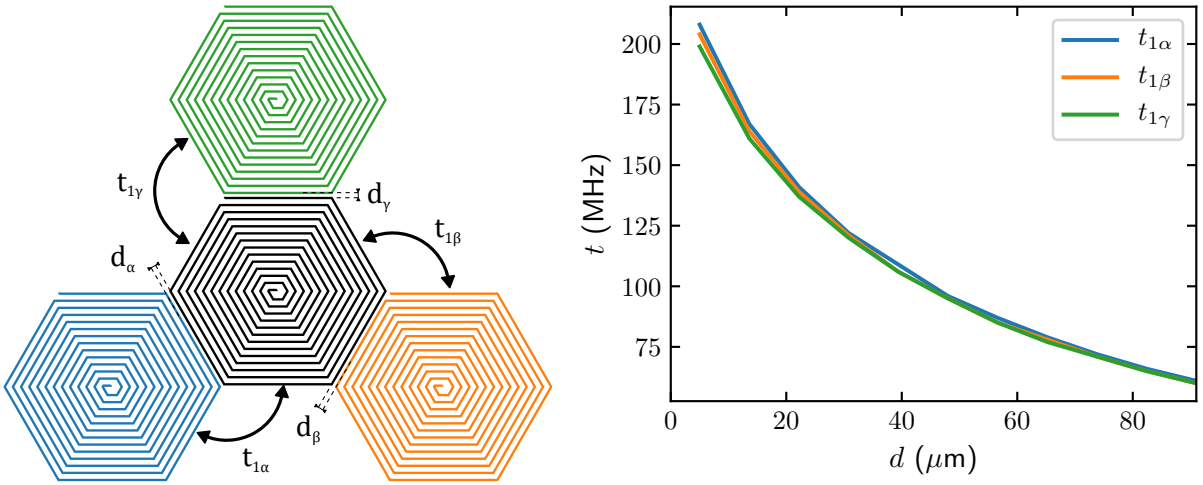

Figure 4.2: On the left, the definition of the three NN couplings between the spiral resonators. On the right, the evolution of theses couplings as a function of the distance between the resonators. One can observe a small anisotropy of the coupling at small distances.

	f_0 (GHz)	$t_{1\alpha}$ (MHz)	$t_{1\beta}$ (MHz)	$t_{1\gamma}$ (MHz)
Silicon	5.934	208	204	199

Table 4.1: Coupling between adjacent sites obtained for $d_1 = d_2 = d_3 = 5\,\mu\text{m}$

4.1.2 Free boundaries and coupling to probe lines

The full design of the sample is shown in figure 4.3, it contains 324 sites. The actual samples are micro-fabricated through photo-lithography and reactive ion etching of a sputtered Nb layer as detailed in Appendix A. In chapter 1, we have seen that the honeycomb lattice presents edge states on bearded and zigzag edges. Our design combines the three possible types of boundaries to test these predictions. As can be seen in figure 4.3, the upper boundary is a bearded edge, the bottom one is a zigzag edge and the two side ones are armchair edges. Four probing lines are coupled to B sites located at each of the four corners of the lattice. We have chosen B sites to ensure that we couple to the edge states as these modes are localized on the B sublattice (see section 1.2). Figure 4.4 shows SEM pictures of the coupling regions.

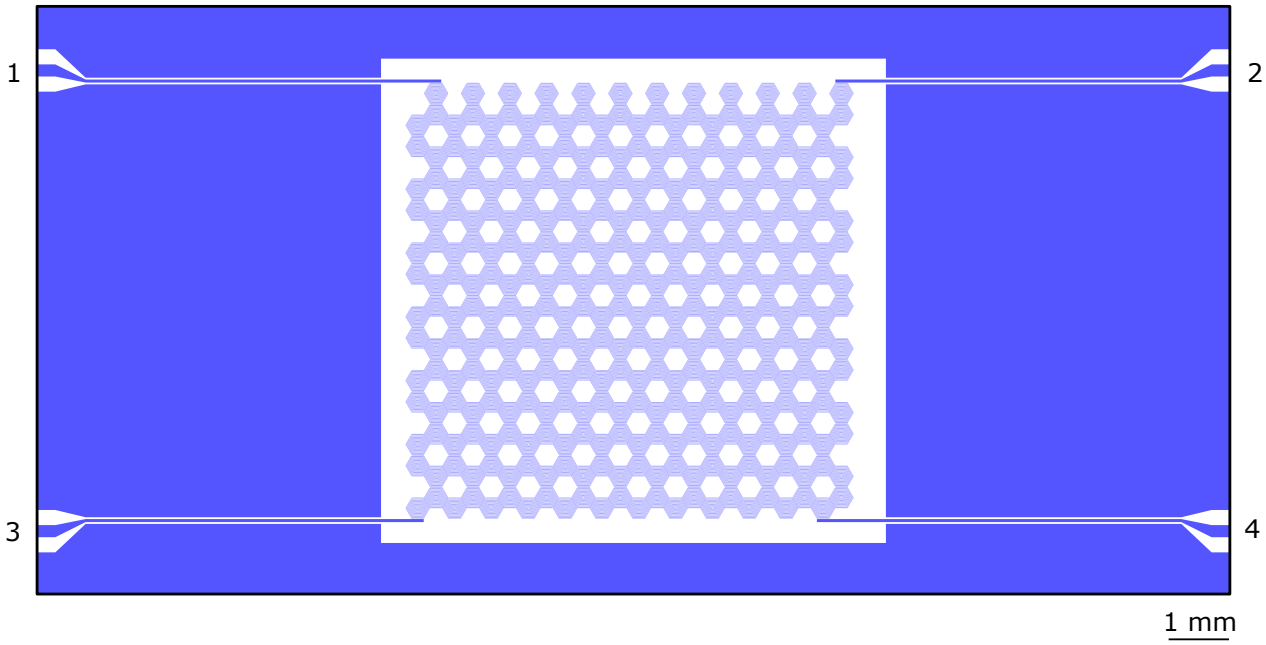

Figure 4.3: Mask design to micro-fabricate a honeycomb lattice by lithography. Each of the 324 sites is a spiral resonator. The lattice presents different edges: armchair on the sides, zigzag at the bottom and bearded on the top. The lattice is coupled to coplanar waveguides (numerated 1 to 4) through the four corner sites of the lattice. The lattice covers an area of $7.2\,\mathrm{mm} \times 7.2\,\mathrm{mm}$.

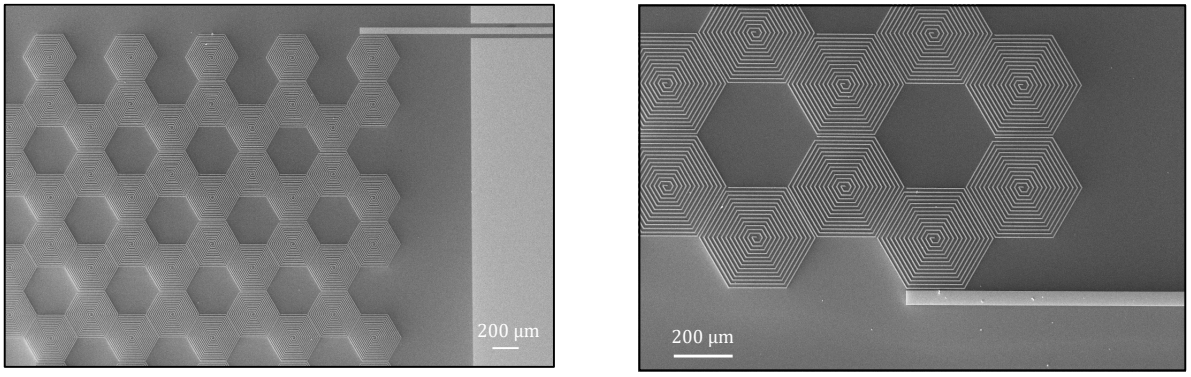

Figure 4.4: SEM picture of a honeycomb lattice sample. The right figure shows the bearded edge and how the probe transmission line is coupled to the corner spiral. The second figure shows the coupling to one zigzag edge.

	f_0 (GHz)	t_1 (MHz)	t_2 (MHz)	t_3 (MHz)
Silicon	5.984	205	−28	12

Table 4.2: Coupling parameters obtained from the DOS for the **HoneycombSi** sample. The resulting DOS is plotted in figure 4.6.

4.2 Transmission measurements

In the following, we present the results obtained with a sample fabricated on a silicon substrate. This sample, labeled **HoneycombSi**, was chosen for the small number of visible defects at the end of the fabrication process. The sample was mounted in our dilution fridge equipped with the microwave and optical **setup A** described in chapter 3.

The most straightforward characterization of the sample is obtained by acquiring transmission spectra between the different ports connected to the sample. The results are shown in figure 4.5, the measurement is performed with a resolution bandwidth 1 kHz. We distinguish two bands: a lower from 5.54 GHz to 5.84 GHz and an upper band from 5.90 GHz to 6.79 GHz. The transmission also presents peaks due to edge states around 5.95 GHz, which are most clearly visible on the transmission along the bearded edge. These peaks also appear in some diagonal transmissions and on the spectrum corresponding to the transmission along the armchair edge.

4.2.1 Density of states

We construct the Density of States (DOS) by counting the number of peaks in a frequency window of 15 MHz. To do so, we sum all the transmission presented in figure 4.5 and use a standard peak detection routine to find the peaks. This routine consists in finding the local maxima of the transmission and keeping only the maxima separated from each other by at least 500 kHz. The summation over all transmission spectra avoids counting the same peak many times. The resulting DOS is shown in figure 4.6. As detailed in chapter 1, we identify five points of interest in the DOS, from which we deduce the values of the parameters entering the tight-binding model:

$$f_0 = \frac{1}{6}\left(f_{\min} + f_{\max} + 4f_D\right) \tag{4.2.1}$$

$$t_1 = \frac{1}{8}\left(f_{\max} - f_{\min} + f_l^+ - f_l^-\right) \tag{4.2.2}$$

$$t_2 = \frac{1}{9}\left(f_D - \frac{f_{\max} + f_{\min}}{2}\right) \tag{4.2.3}$$

$$t_3 = \frac{1}{24}\left(f_{\max} - f_{\min} - 3f_l^+ + 3f_l^-\right) \tag{4.2.4}$$

The deduced values are summarized in table 4.2. The 2nd NN coupling t_2 is about 15 % of t_1.

4.2.2 Comparison to Green function calculations

Using the tight-binding model parameters obtained above, we can estimate the expected transmission for our sample and compare it to our data. We calculate the Green function

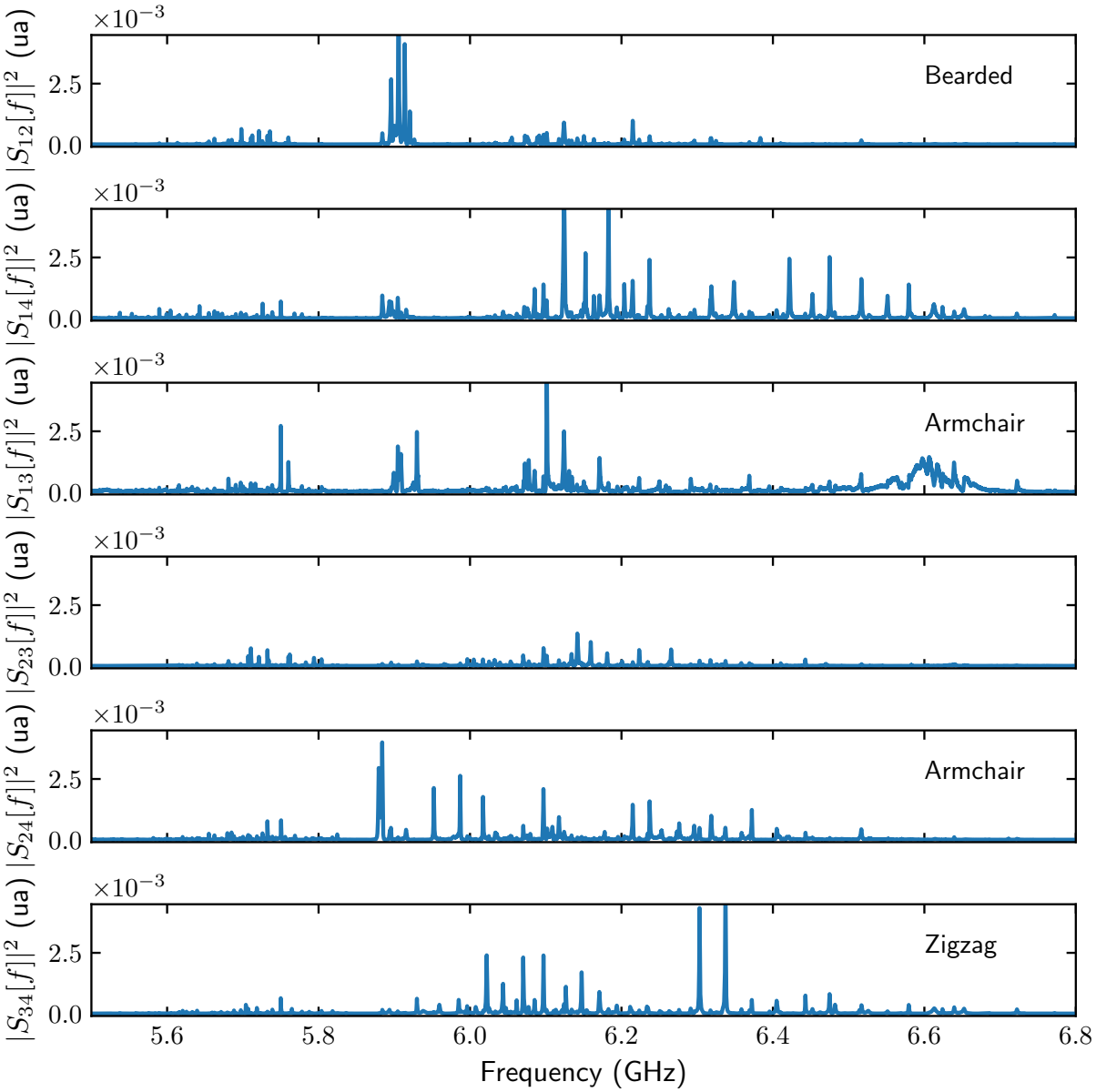

Figure 4.5: Transmission measurements for the sample **HoneycombSi**. The type of edge is indicated in the upper right corner. For the bearded edge, we clearly see peaks around 5.95 GHz that correspond to edge states. For the others transmissions, we distinguish two bands. The lower band presents less peaks than the upper band and seem less coupled. The zigzag edge does not have peaks in the gap between the two bands.

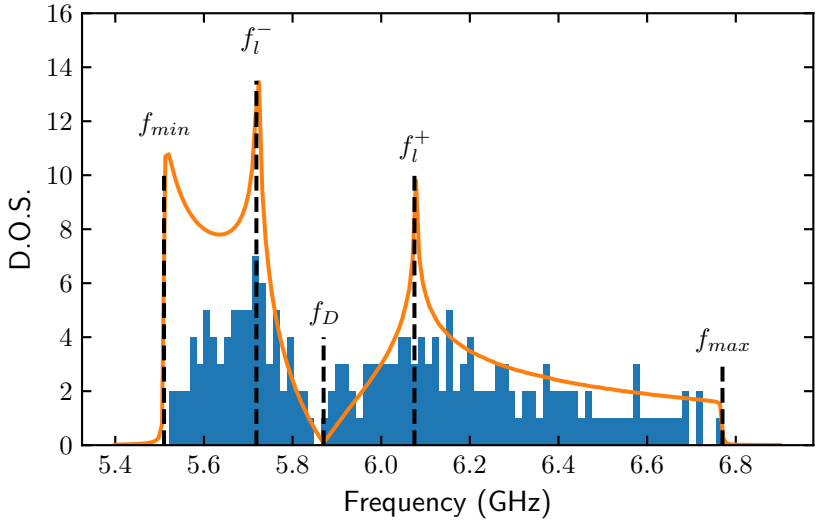

Figure 4.6: Measured DOS of the **HoneycombSi**. The blue histogram counts the peaks identified from the sum of all the transmission measurements shown in figure 4.5. The orange line represents the DOS of the tight-binding model extracted by the point of interest method. The difference between the data and the model is due to the fact that many modes are not visible in the transmission spectra.

between the sites i and j using

$$G_{ij}[f] \simeq \sum_{\mu} \frac{w_{i\mu} w_{j\mu}}{f - f_\mu + j\gamma} \tag{4.2.5}$$

where the sum runs over all the eigenmodes μ of the lattice. As shown in figure 4.7, this qualitatively reproduce the measured spectra. We count 7 edge state peaks between the two bands for the bearded edge and 3 for the zigzag one. This ratio of approximately 2 between the number of edge states along the two different edges is due to the fact that, in the Fourier space, bearded edge states occupy a range of wavevectors two times larger than zigzag edge states.

4.3 Measured band structure

In order to gain more insight about the modes observed in the transmission spectra, we use the mode imaging technique described in chapter 3. Figures 4.8 and 4.9 shows 24 modes measured with continuous scan and fixed laser intensity. The raw images correspond to the variation of $|S_{12}|^2$ as a function of position. For a given mode, we obtain the weight $|\Psi(\mathbf{r})|^2$ on site i by averaging the image over the area of the site. We have also measured 110 more bulk modes using the raster scan method. Eight of them are shown in figure 4.10. We then use the following sign retrieval algorithm to obtain $\Psi(\mathbf{r})$.

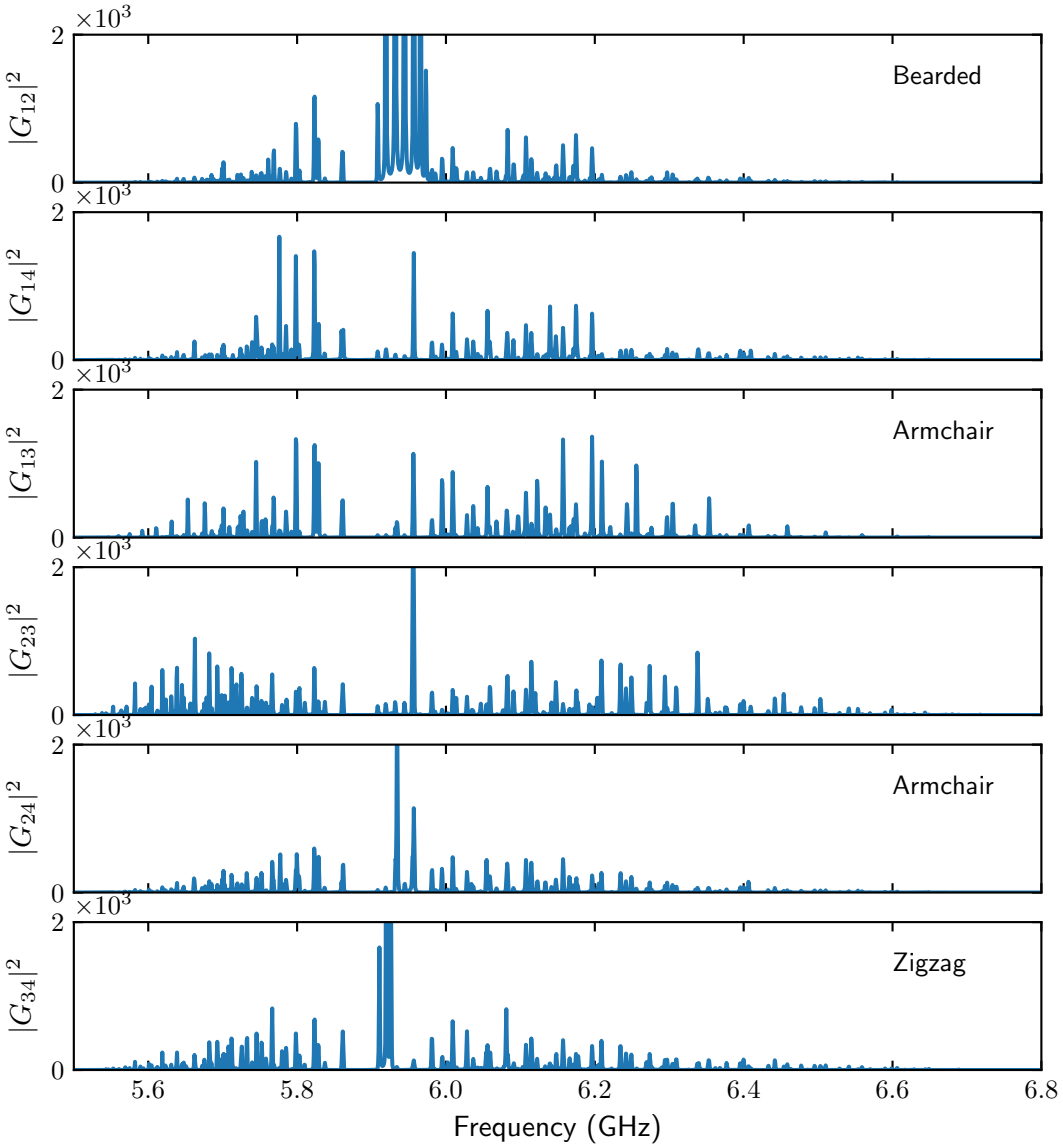

Figure 4.7: Green function calculated from a tight-binding model of the sample. This figure must be compared to figure 4.5. The tight-binding parameters correspond to the ones indicated in table 4.2.

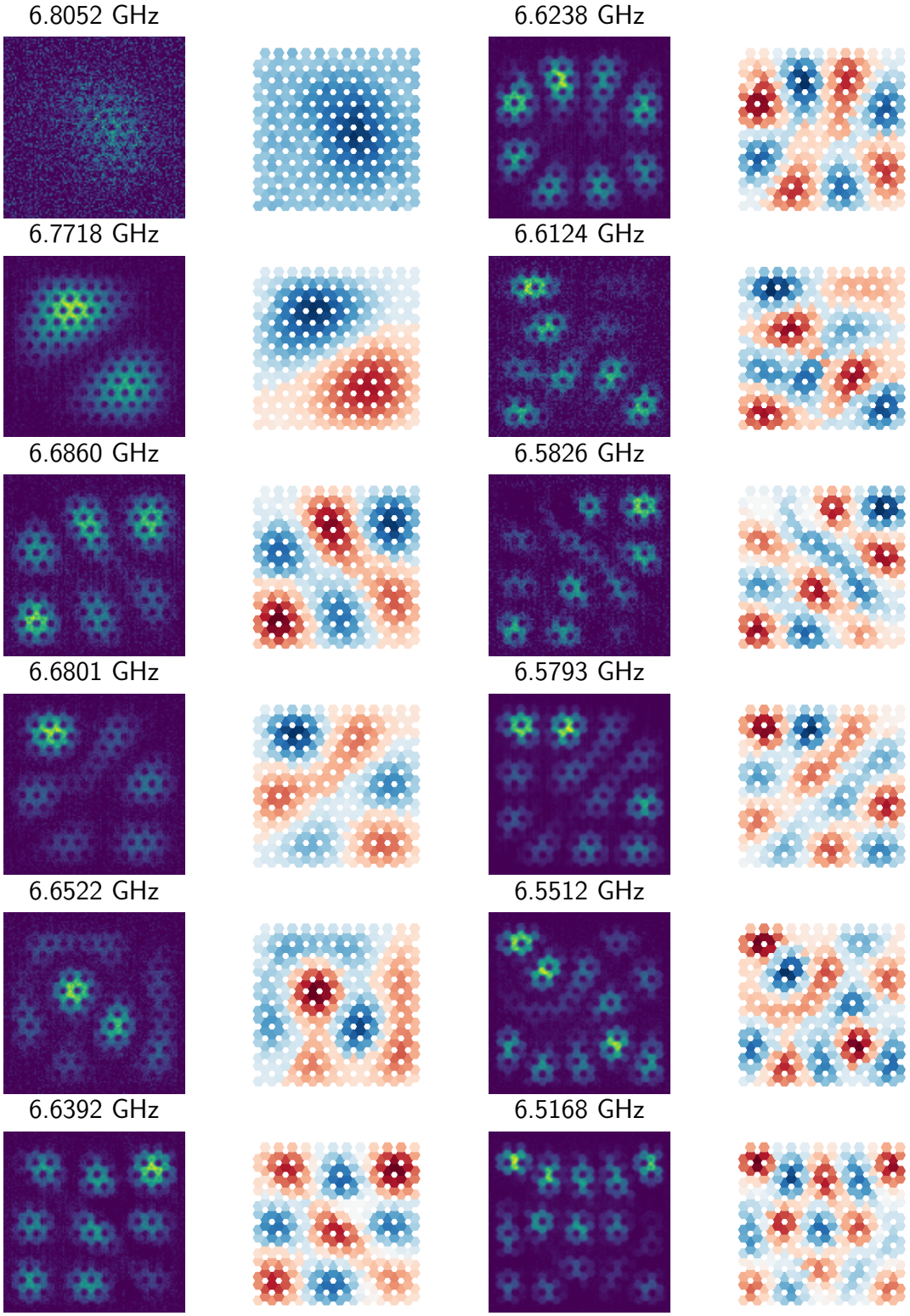

Figure 4.8: Images of the highest frequency modes obtained by continuously scanning the laser position across the sample. For each mode, the raw data which is proportional to $|\Psi(\mathbf{r})|^2$ is shown on the left. On the right, the mode $\Psi(\mathbf{r})$ is represented with the retrieved sign

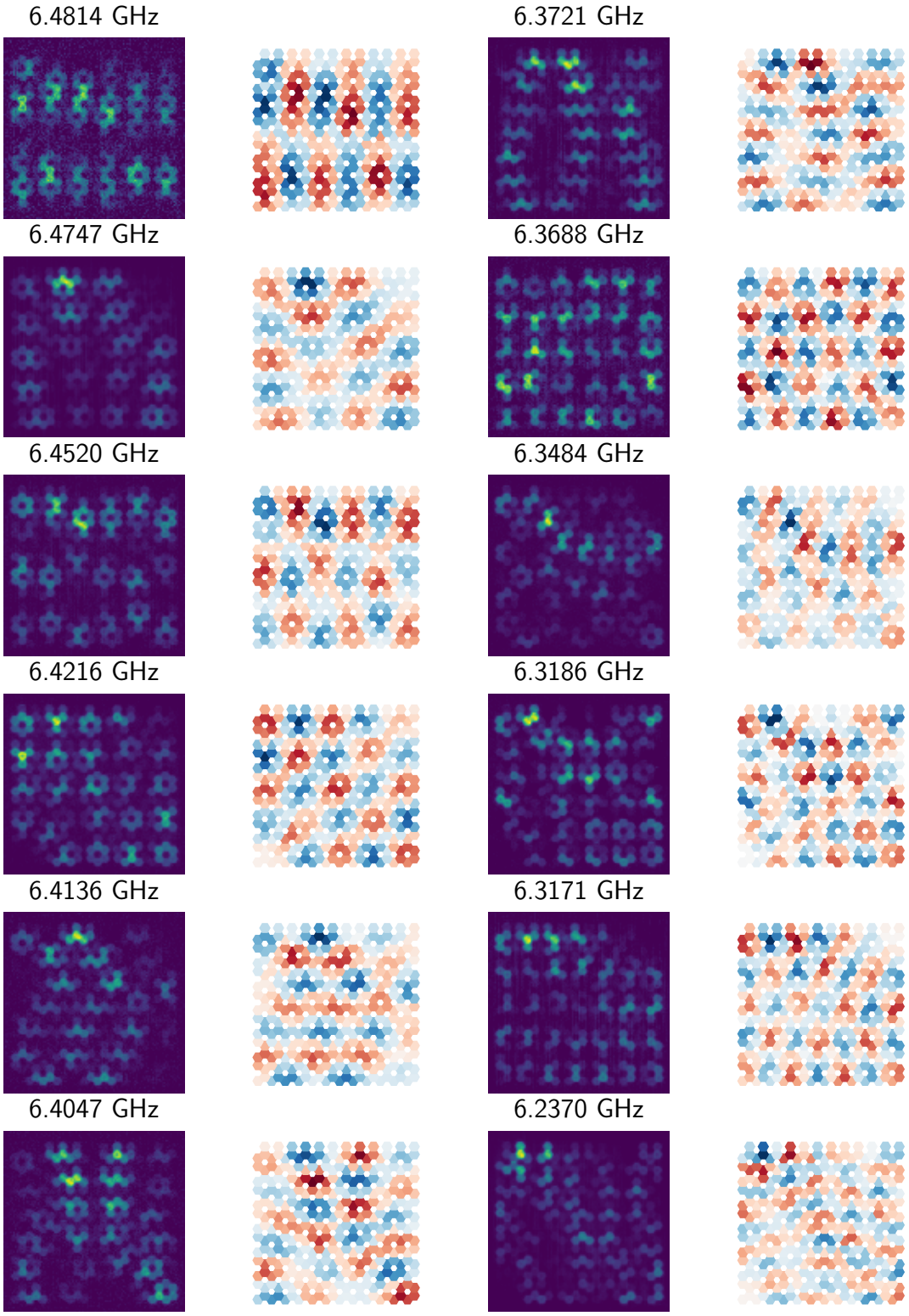

Figure 4.9: Following of figure 4.8

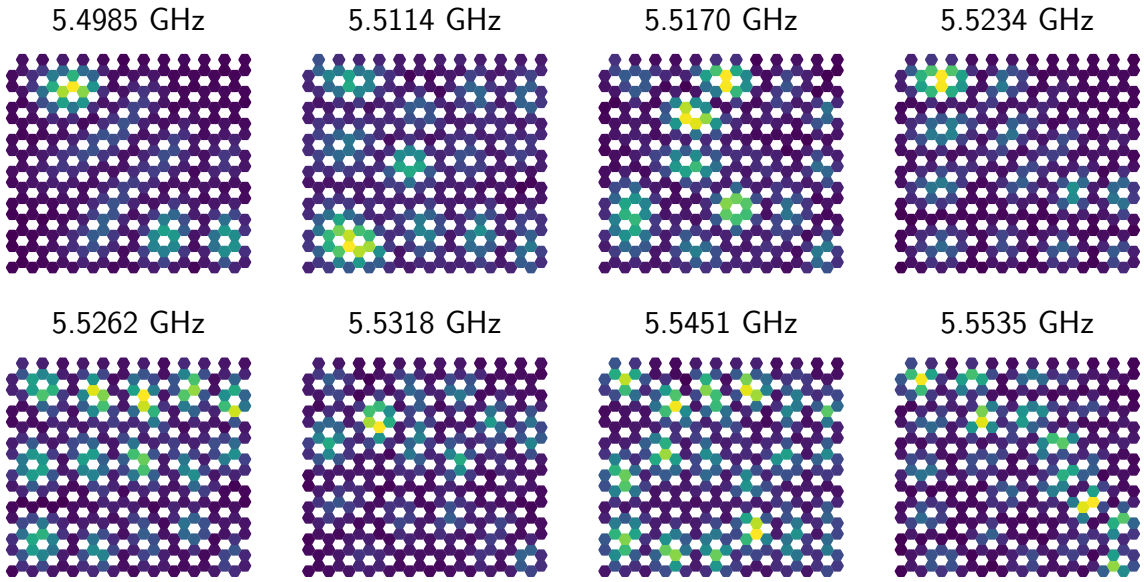

Figure 4.10: Images of the lowest energy modes obtained with the raster scan method.

4.3.1 Sign retrieval algorithm

In order to retrieve the sign of a mode, we have to make some assumptions about the model that gives rise to this mode. Here, we suppose that the measured $\Psi(\mathbf{r})$ are close to the modes of an ideal honeycomb lattice. More precisely, we search for the vector β such that $|\sum_{\alpha=1}^{M} \beta^\alpha \phi_\alpha(\mathbf{r})|^2$ reproduces the measured $|\Psi(\mathbf{r})|^2$, where $\phi_\alpha(\mathbf{r})$ are the eigenmodes of the honeycomb lattice having the same geometry as the sample but with only NN coupling. Numerically, we have to minimize the following quantity:

$$L(\beta) = \sum_{\mathbf{r}} \left(|\Psi(\mathbf{r})|^2 - \left| \sum_{\alpha=1}^{M} \beta_\alpha \phi_\alpha(\mathbf{r}) \right|^2 \right)^2 \tag{4.3.1}$$

This function can be rewritten as

$$L(\boldsymbol{\beta}) = \sum_{\mathbf{r}} \left| \sum_{\alpha=1}^{M} \beta_\alpha \phi_\alpha(\mathbf{r}) \right|^4 - 2 \sum_{\mathbf{r}} |\Psi(\mathbf{r})|^2 \left| \sum_{\alpha=1}^{M} \beta_\alpha \phi_\alpha(\mathbf{r}) \right|^2 + \sum_{\mathbf{r}} |\Psi(\mathbf{r})|^4 \tag{4.3.2}$$

The last term is a constant and can be dropped out. For a fully delocalized mode, $\phi_\alpha(\mathbf{r}) \propto 1/\sqrt{N}$ and the first sum is approximately N times smaller than the second one. We therefore start by maximizing the opposite of the second term that corresponds to a quadratic form:

$$\sum_{\mathbf{r}} |\Psi(\mathbf{r})|^2 \left| \sum_{\alpha=1}^{M} \beta_\alpha \phi_\alpha(\mathbf{r}) \right|^2 = \sum_{\gamma=1}^{M} \sum_{\alpha=1}^{M} \left(\sum_{\mathbf{r}} \phi_\gamma(\mathbf{r}) |\Psi(\mathbf{r})|^2 \phi_\alpha(\mathbf{r}) \right) \beta_\gamma \beta_\alpha \tag{4.3.3}$$

Maximizing this quadratic form under the constraint $|\boldsymbol{\beta}| = 1$ can be done exactly by taking the eigenvector associated to the largest eigenvalue. This gives us a starting value

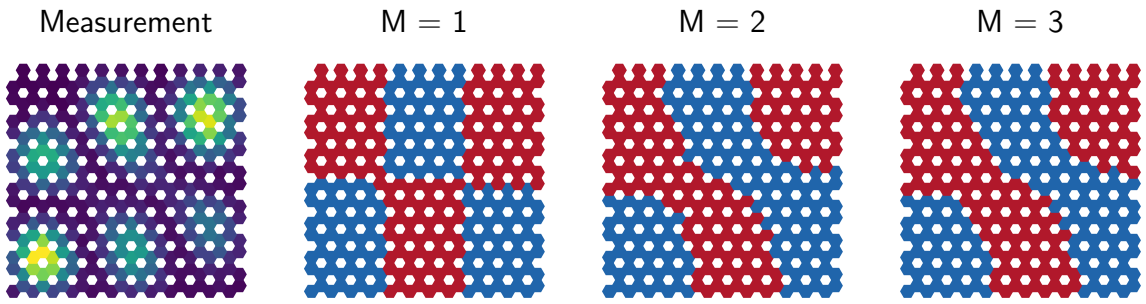

Figure 4.11: Convergence of the sign retrieval algorithm. The left plot is the measured mode. The three other images show the sign calculated by the algorithm for different values of M.

of β from which we minimize $L(\beta)$ through an iterative procedure. We define $\tilde{\Psi}(\mathbf{r}) = \sqrt{|\Psi(\mathbf{r})|^2} \times \text{sign}(\sum_\alpha^M \beta_\alpha \phi_\alpha(\mathbf{r}))$ and look for β that minimizes the least square problem $||\tilde{\Psi}(\mathbf{r}) - \sum_\alpha^M \beta_\alpha \phi_\alpha(\mathbf{r})||^2$. We reiterate the procedure until the vector β converges to a fixed point. The obtained vector β depends on the choice of basis modes $\phi_\alpha(\mathbf{r})$. We then iterate over all the sets of M basis modes with adjacent energies and keep the one that minimizes $L(\beta)$. We have tested the procedure for different values of M, we observe that the deduced sign does not change for $M > 3$ (see figure 4.11). The experimentally measured mode is finally given by

$$\Psi(\mathbf{r}) = \sqrt{|\Psi(\mathbf{r})|^2} \times \text{sign}(\sum_\alpha^M \beta_\alpha \phi_\alpha(\mathbf{r})) \tag{4.3.4}$$

4.3.2 Band structure of the bulk

From the measured signed mode $\Psi(\mathbf{r}) = \begin{bmatrix}\phi_1(\mathbf{r}) & \phi_2(\mathbf{r})\end{bmatrix}$, we can now compute the mode amplitude in Fourier space:

$$\Psi(\mathbf{k}) = \sum_{\mathbf{r}} e^{i\mathbf{kr}} \begin{bmatrix}\phi_1(\mathbf{r}) \\ \phi_2(\mathbf{r})\end{bmatrix}, \tag{4.3.5}$$

Figures 4.12 and 4.13 shows the Fourier transform $||\Psi(\mathbf{k})||^2$ of the modes plotted in figures 4.8 and 4.9. To attribute a wavevector to a mode, we look for the value of $|\mathbf{k}|$ that maximizes $||\Psi(\mathbf{k})||^2$ in the first Brillouin zone.

We finally obtain the relation dispersion of the modes as a function of the norm of the wavevector $|\mathbf{k}|$ as shown in figure 4.14. This plot comes from the mapping of 138 modes out of the 324 expected ones with 93 modes in the upper band and 45 in the lower band. We compare this measured band structure with three models: the effective tight-binding deduced from the DOS (see above), and the two ab-initio models developed in chapter 2: the **admittance model** and the **CMT model**.

For the **admittance model**, the curve is the direct result from EM calculation without any additional offset. For the **CMT model**, we have adjusted the bare frequency f_0 in order

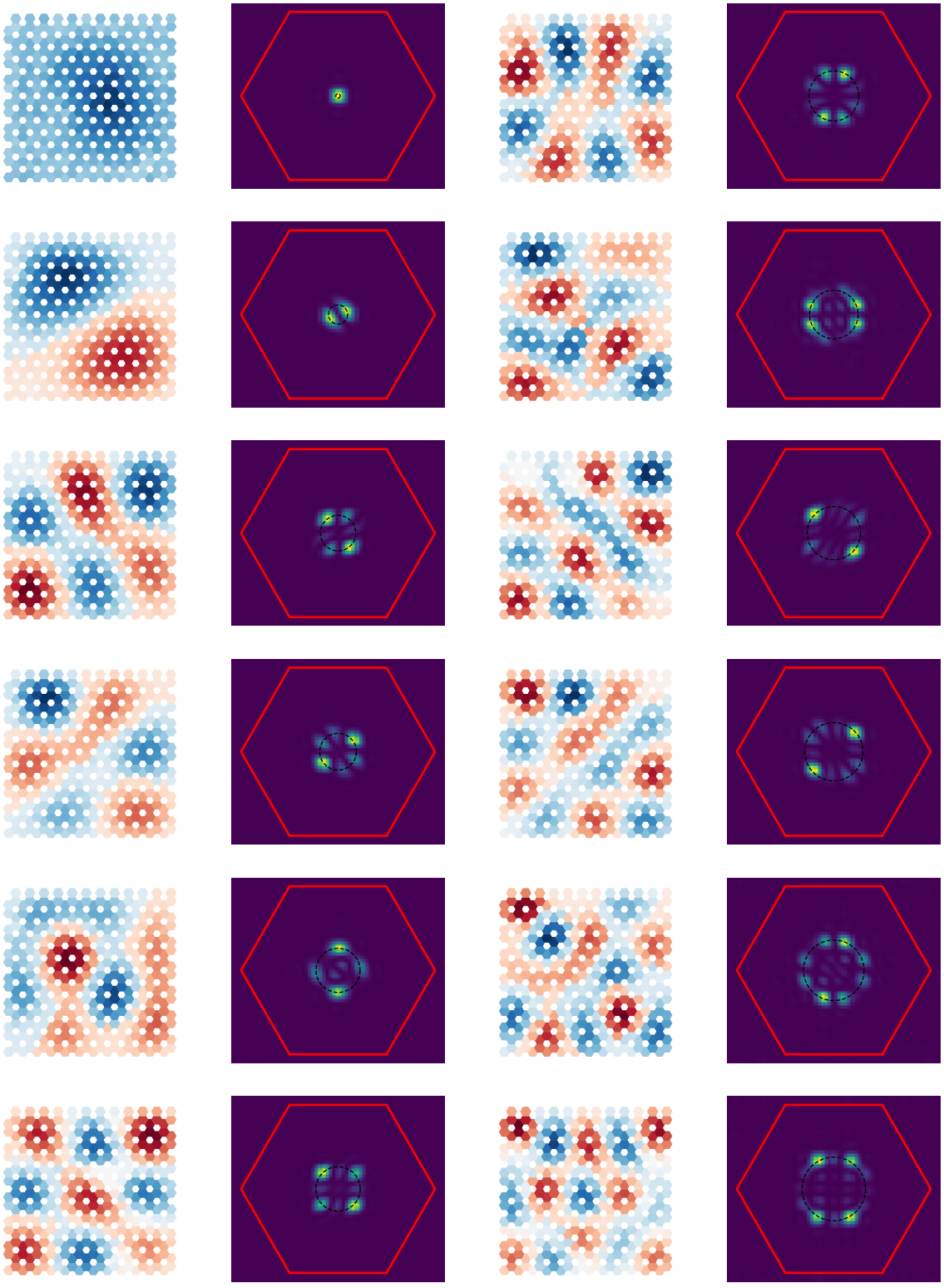

Figure 4.12: Fourier transform of the modes shown in figure 4.8. For each mode, the signed mode $\Psi(\mathbf{r})$ is shown on the left. On the right, the mode Fourier transform $||\Psi(\mathbf{k})||^2$ is represented. The red line delimits the first Brillouin zone and the dashed circle indicates the value of $|\mathbf{k}|$ where the maximum of the Fourier transform is located.

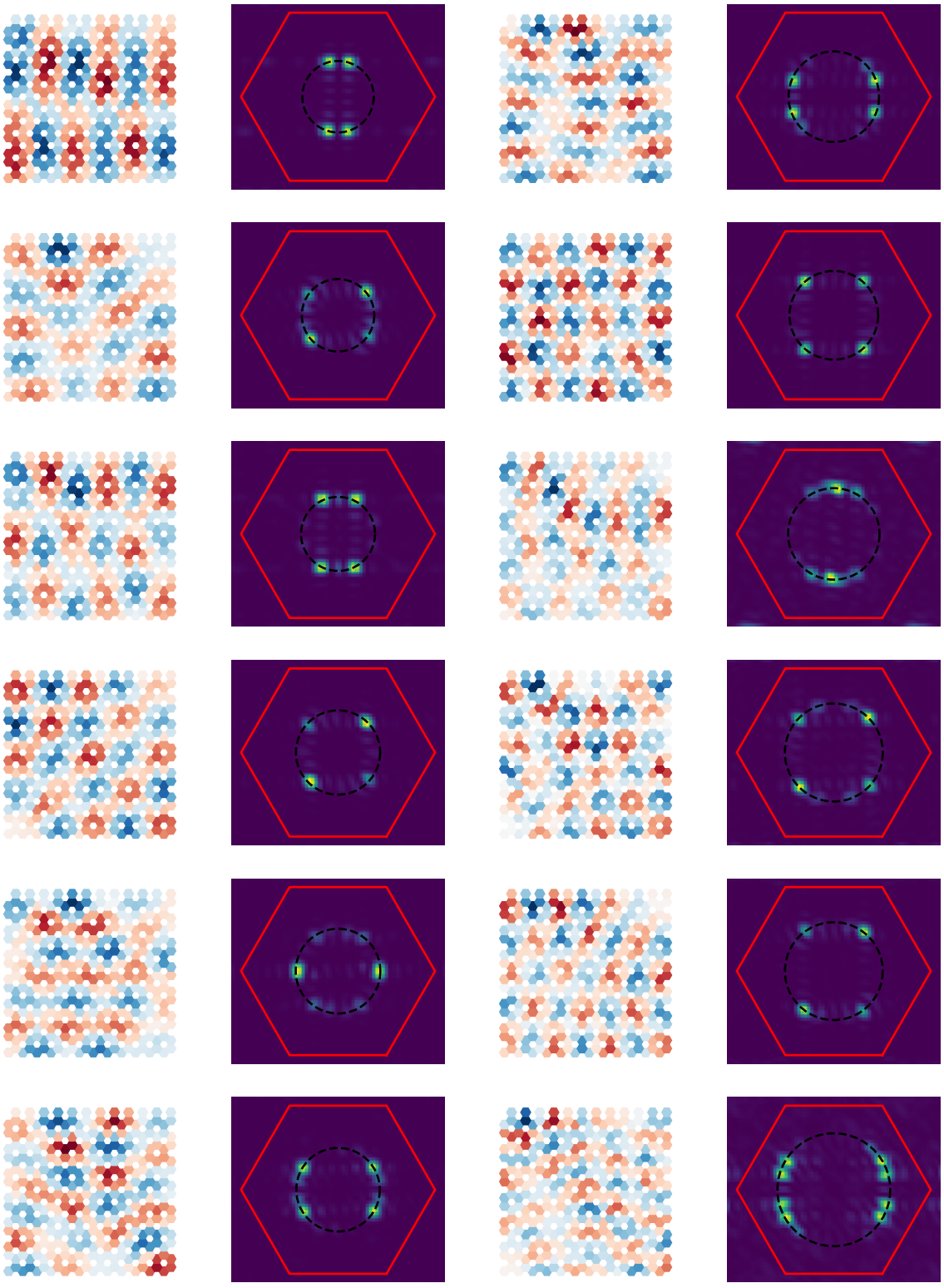

Figure 4.13: Fourier transform of of the modes shown in figure 4.9. See figure 4.12.

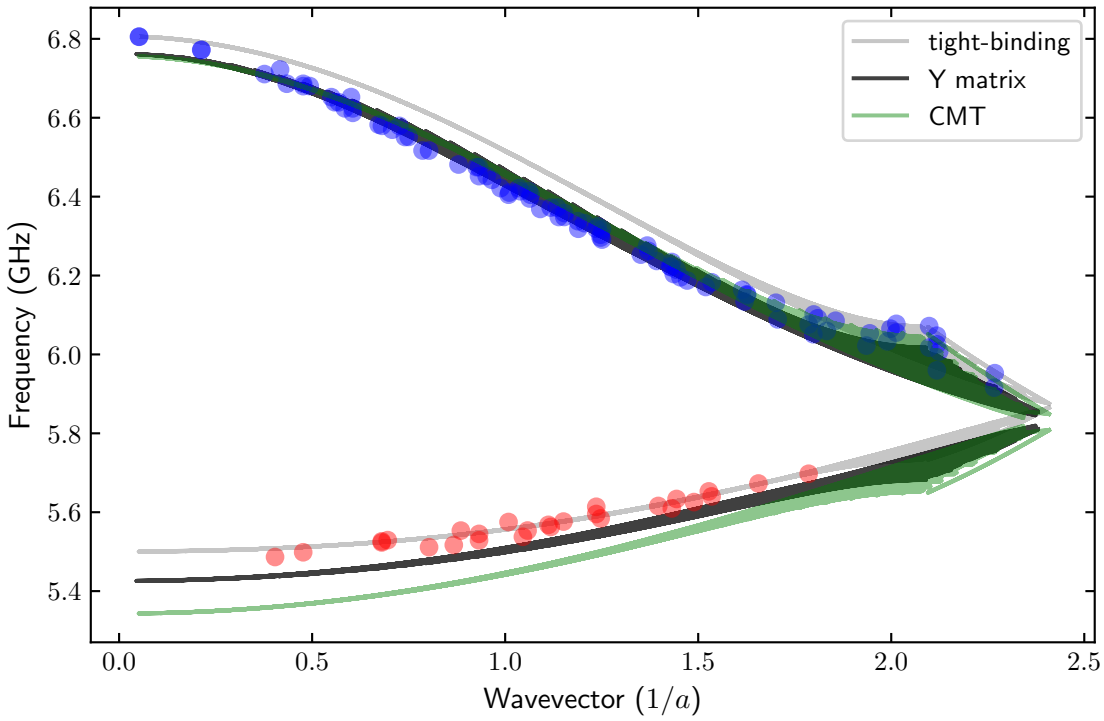

Figure 4.14: Band dispersion obtained from the measurements shown in figures 4.8 and 4.9 and other not shown measurements. This band structure displays 138 modes out of the 324 expected mode of the lattice. The solid curves are three different models of infinite lattice: in gray the **admittance model**, in green the **CMT** model and in black the tight binding obtained from the DOS.

to take into account the layer of silicon oxyde on top of the substrate. As shown in chapter 2, we do not expect the CMT model to be quantitatively exact because the distance between the sites is too small for the model to be valid. The admittance model is also not in perfect agreement with the data. We do not have any explanation for the systematic shift of the lower band compared to the expected dispersion relation.

4.4 Characterization of the edge states

In the transmission spectra, we have identified peaks that we attributed to edge states. In this section, we present the images of these modes from which we deduce their band structure and penetration lengths.

4.4.1 Edge state wave functions

Figure 4.15 shows the mode intensities for the 9 edge states that we have identified. Their frequencies lie between 5.87 GHz to 5.94 GHz, close to the Dirac point frequency estimated at 5.92 GHz. All the modes only occupy the sublattice that is next to the boundary as expected for such states (see section 1.2).

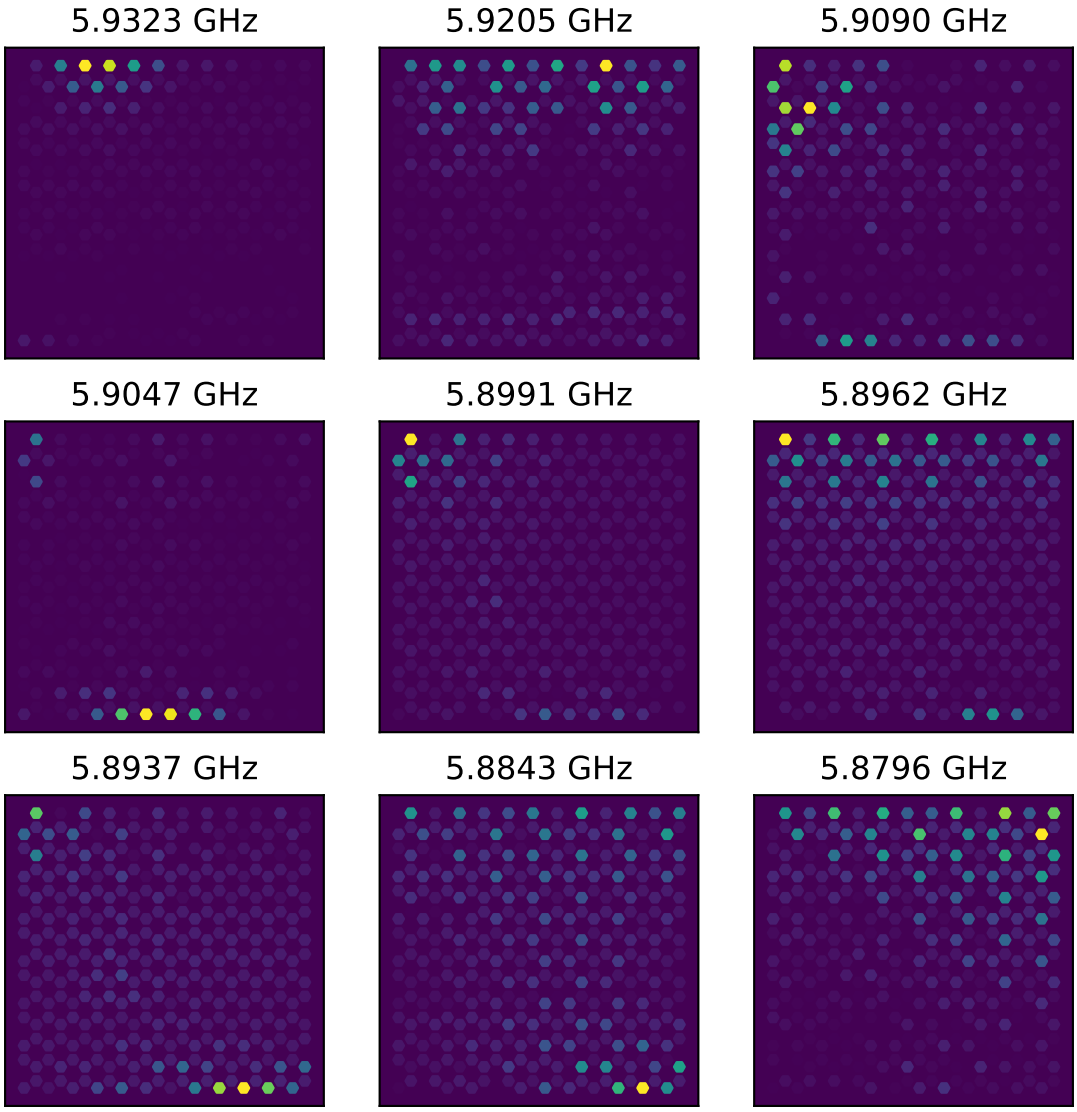

Figure 4.15: Measured edge state intensities $|\Psi(\mathbf{r})|^2$.

4.4.2 Measured band structure

In order to reconstruct the band structure of these modes, we cannot use the method described for the bulk modes as these modes are not localized over the whole lattice and the sign algorithm fails. We extract their wavevectors directly from the Fourier transform of the mode intensity $|\Psi(\mathbf{r})|^2$. We look for the maximum of the Fourier transform which yields a wavevector that is twice the wavevector of the mode. The resulting band structure is presented in figure 4.16.

We compare this measured band structure to the calculated one for an infinite ribbon having the same height than our sample and the same type of top and bottom edges. The tight-binding parameters are taken from table 4.2, we also allow for a shift of the resonance frequency of the sites located on the edges.

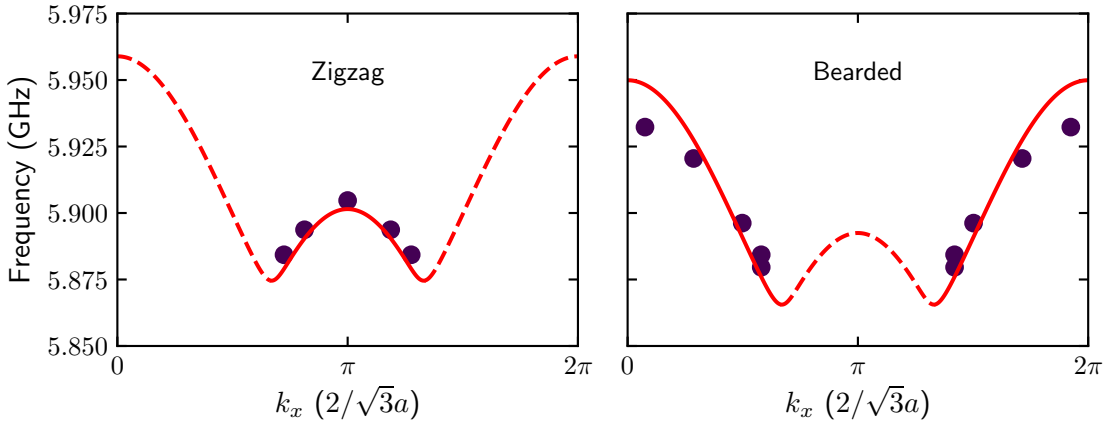

Figure 4.16: Reconstructed band structure of the zigzag and bearded edge states. The dots indicate measured points. The red line is the prediction of a tight-biding model for an infinite ribbon having the same height, top and bottom edges than the sample. The tight-binding parameters correspond to the ones that were deduced from the measured DOS. We shift the resonance frequency of the sites on the edge by -9 MHz to reproduce our data. This shift is comparable to the value of -10 MHz that is predicted from Sonnet simulations.

4.4.3 Measured penetration length

The decay of the edge states are shown in figure 4.17. Each curve is the average of the mode intensity along the direction perpendicular to the boundary. We see that some edge states have weight on both sides of the sample. We fit these curves to a decaying exponential. The resulting penetration lengths $\xi(k_x)$ are shown in figure 4.18 and compared to the predictions of the tight-binding model described above.

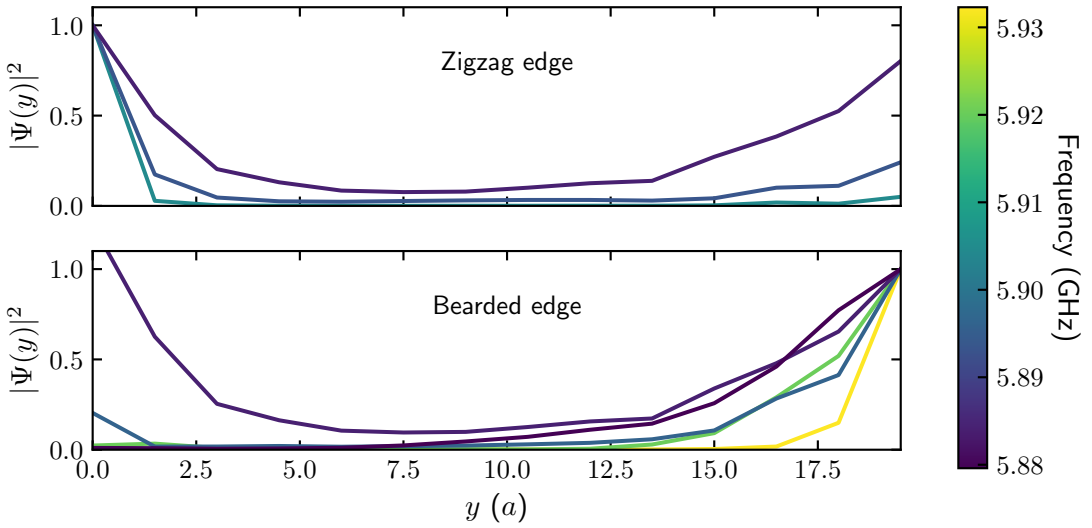

Figure 4.17: Decay of edge state intensities $|\Psi(\mathbf{r})|^2$. Each profile is normalized so that the intensity is one at $y = 0$. Here, we only take into account the weight on the B sublattice.

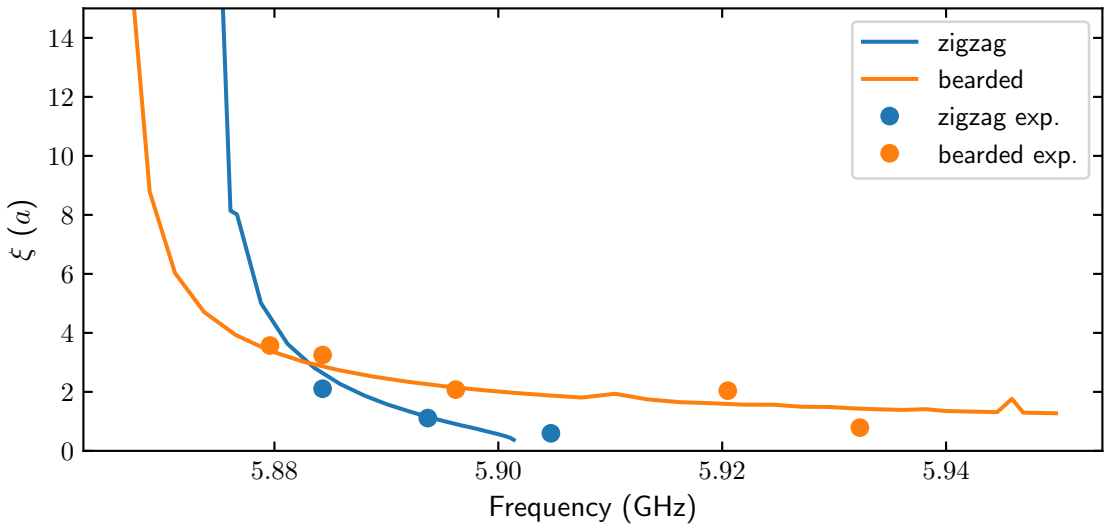

Figure 4.18: Evolution of the localization length of the edge states for the bearded and the zigzag boundaries. The measured lengths (dots) are compared to the predictions of the same tight-binding model than used in figure 4.16.

Conclusion

We have shown in this chapter that superconducting circuits offer an interesting platform to simulate lattices system. We were able to reproduce several properties of the honeycomb lattice with our sample. We have been able to reveal the wavefunction of many lattice modes, from which we could reconstruct the band structure of the honeycomb lattice. This band structure is quantitatively explained by the *ab initio* admittance model developed in chapter 2. Finally, we have been able to observe the edge modes of the honeycomb lattice and show that they appear, as predicted, on the zigzag edge and not on the armchair edges. For theses zigzag/bearded edge states, we have been able to reconstruct their band structures and we measured their penetration lengths.

Chapter 5

Simulation of Semenoff insulators with superconducting resonators

Contents

In the first chapter, we have described the edge states arising when two Semenoff insulators with opposite mass are set aside [55]. Theses edge states with atom thick domain wall are difficult to observe in solid-state 2D material as it requires high tunability over the lattices parameters. In artificial system, this constraint is lifted as it is straightforward to tune individually each site and each coupling by design. This tunability have allowed Noh et al. [81] to observe Semenoff edge states in evanescently coupled waveguide arrays. In this chapter, we present the realization and the observation of Semenoff edge states in a superconducting lattice. In the first part of this chapter, we describe the design of the two types of samples that we considered. Three samples have been measured for this thesis: two zigzag domain walls on a silicon substrate and a sapphire substrate that we will now on name **ZigzagSi** and **ZigzagSa** respectively and one armchair domain wall on a silicon substrate **ArmchairSi**. Similarly to the chapter on the experimental realization of the honeycomb lattice, we then first present transmission measurements for the three samples. The point of interest method is used to fit the DOS and get the tight-binding parameters. The mode imaging allows us to reconstruct the band structure and to compare it to different models. Combining optical observation and mode imaging, we have also been able to observe site defects and the associated localized states [82]. The last section of this chapter is devoted to the observation and the characterization of the Semenoff edge states. With the mode imaging, we are able to extract both their band structure $\omega(k)$ and their penetration length $\xi(k)$. This information is then compared to the theoretical expectation for different models: infinite slabs and finite size tight-binding simulations.

5.1 Superconducting circuit design

In this section, we first give the target model using the analysis done in the first chapter. We then present how we implement the different parameters of this model: the Semenoff mass μ and the hopping term t_1. Finally, we discuss the two Semenoff designs used in this experiment.

5.1.1 Target parameters

Some complications in the admittance model and the CMT model of the **HoneycombSi** sample come from the strong nearest neighbor coupling. To avoid such complication, we reduced the NN coupling to $t_1 = 120\,\text{MHz}$ which corresponds to a gap between two adjacent spiral of about 35 µm. For this experiment, we also decided to implement a larger lattice than the honeycomb lattice sample. The Semenoff lattices we propose have a size of 13.6 mm by 8 mm. The optical and microwave **setup B** described in chapter 3 was specifically designed for this purpose. The domain wall is implemented in the longest direction in order to maximize the number of edge states and thus having a better resolution in the band structure. To observe a clear signature of edge modes, the penetration length ξ has to be smaller than the half width of the sample. Using the low energy model derived in section 1.4 this imposes:

$$\xi_0 = \frac{3ta}{4\mu} < \frac{w}{2} \quad \text{or} \quad \mu > \frac{3a}{2w}t \tag{5.1.1}$$

with the step of the lattice $a \simeq 400\,\mu\text{m}$. The Semenoff mass has to be bigger than 9 MHz in order to have a penetration length smaller than the half-width. The Semenoff mass should

not be too large as the low energy picture breaks down for too high values of μ. In order to have a penetration length significantly smaller than the half-width, we target $\mu = 60\,\text{MHz}$. With this value, the edge states are well defined with a penetration length $\xi_0 = 600\,\mu\text{m}$. Finally, in order to address the edge modes we couple the two extremal sites of the domain wall to two probing transmission lines. The target parameters are summarized in table 5.1. The following of this section is dedicated to the implementation of theses parameters in a lattice of spiral resonators.

	f_0 (GHz)	μ (MHz)	t_1 (MHz)	v_F (a.MHz)	ξ_0 (a)
Target	6.0	60	120	180	1.5

Table 5.1: Targeted parameters for the Semenoff domain lattices. The Fermi velocity and the penetration length are calculated from the low energy model section 1.4.

5.1.2 Tuning of the on-site energy

The Semenoff mass μ is given by the detuning between the two sublattices. One of the site

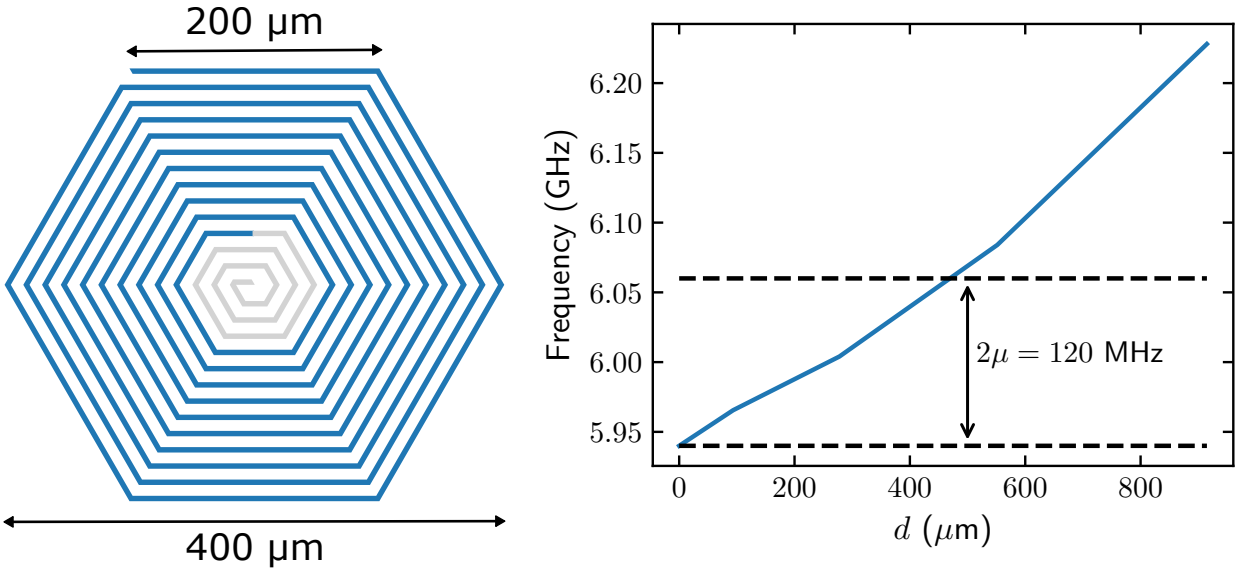

Figure 5.1: On the left, the spiral resonator design. The grey part represents the part that is removed in order to tune its frequency. The left panel present the evolution of the resonance frequency as the spiral is shortened. In order to have a μ of about 60 MHz, the spiral has to be shortened by 500 µm or 3 turns.

of the Semenoff insulator is the spiral resonator used for the honeycomb lattice described in section 2.1. The other one is the same spiral with a reduced length as shown in figure 5.1. To keep the same space occupation for each spiral, we reduce the length starting from the center of the spiral. The right panel in figure 5.1 shows the evolution of the first resonance frequency as the spiral is shortened. To implement a μ of 60 MHz, a length of 500 µm must be removed.

5.1.3 Nearest neighbor coupling

As shown in chapter 4, the coupling between two spiral resonators depends on the orientation of the link. This is due to the fact that spirals do not have the honeycomb lattice symmetry. When designing this sample, we have adjusted the distance between the sites depending on the link direction as shown in figure 5.2. The three distances are adjusted such that the hopping calculated with the method described in section 2.1 is 120 MHz for all three directions as shown in figure 5.2: $d_1 = d_3 = 30\,\mu\text{m}$ and $d_2 = 35\,\mu\text{m}$.

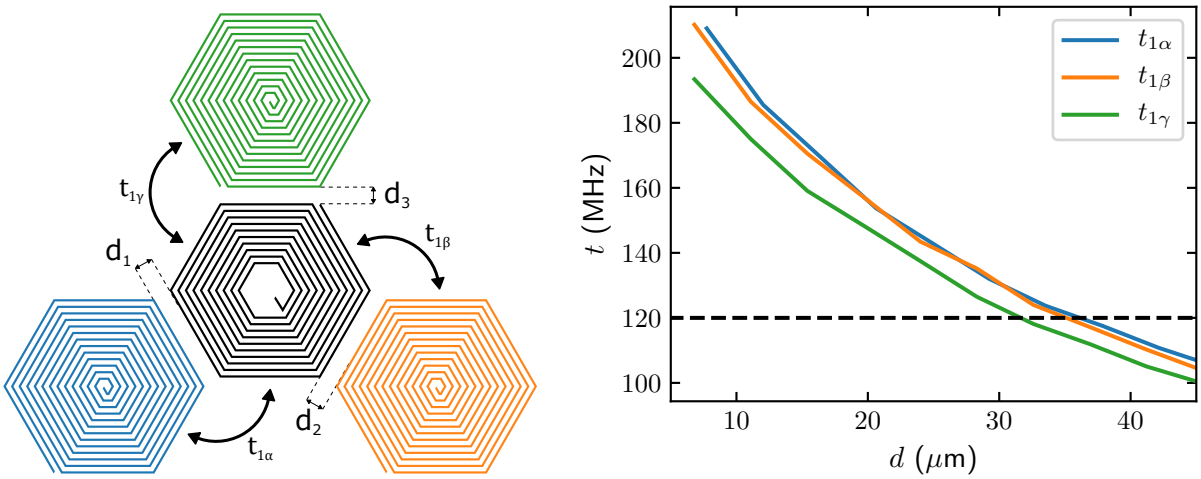

Figure 5.2: On the left, the geometry of the coupling between an A site and a B site. Due to the anisotropic design of the spiral, the hopping energies $t_{1\alpha}$, $t_{1\beta}$ and $t_{1\gamma}$ are not necessarily the same for a given distance. On the right, the hopping energy as a function of the distance. The hopping $t_{1\gamma}$ is smaller than $t_{1\alpha}$ and $t_{1\beta}$. The dashed line indicates the targeted hopping energy.

5.1.4 Complete sample design

In chapter 1, we have derived analytic results for two domain wall geometries: zigzag and armchair domain walls. The figure 5.3 presents these two configurations with spiral resonators. Due to the anistropy described in the last section, we cannot simply translate the spiral from on side to the other of the domain wall. A mirror image would not work either as the spirals on opposite side of the domain wall would have opposite winding orientations, leading to a very different NN coupling at the domain wall. To prevent this change of orientation and keep the anisotropy, the spiral are rotated by π from one side to the other as can be seen in figure 5.3. The length of the sample allows us to have 21 cells along the domain wall in the zigzag case, 24 in the armchair case. For this finite geometry, there should exist about the same number of modes in the edge state branch.

Maximizing the number of spirals in one sample is obtained for a rectangular shape of the lattice. However, the honeycomb lattice gives rise to zigzag edge states for zigzag boundaries (see section 1.2). For some design, zigzag edge states and Semenoff edge states would share the same sites, giving rise to a mixing of these states. This situation can happen at the two ends of the domain wall as depicted in figure 5.4. In order to prevent this, we have shaped

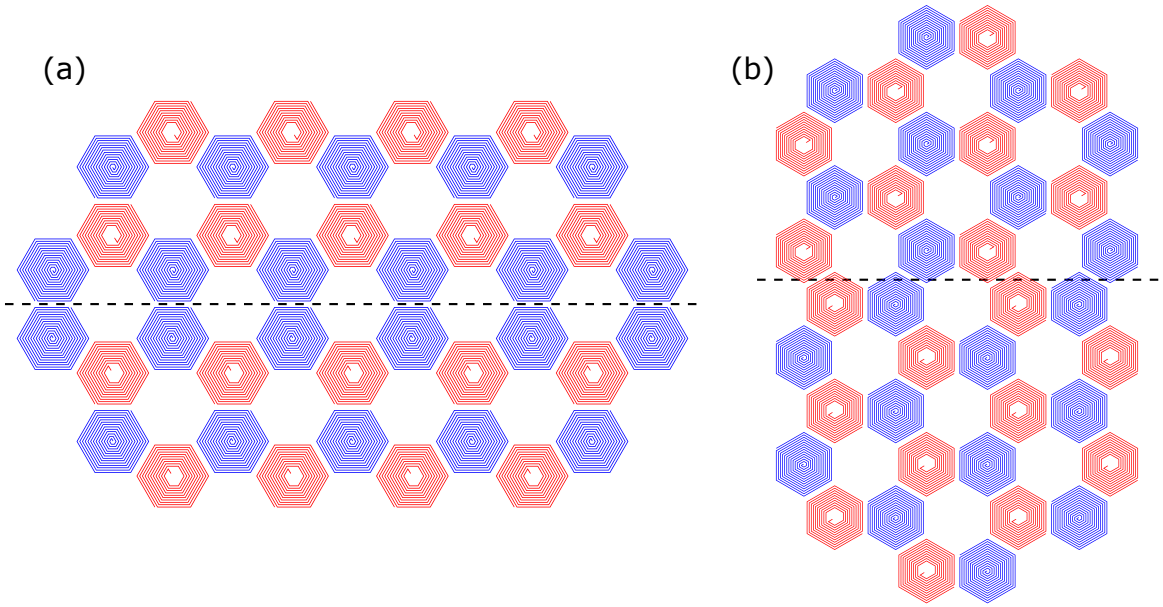

Figure 5.3: Designed domain wall (a) zigzag (b) armchair. The A sites are in blue and the B sites in red. The dashed line indicates the domain wall. The zigzag domain wall is constituted of A sites only whereas the armchair domain wall is made out of A and B sites.

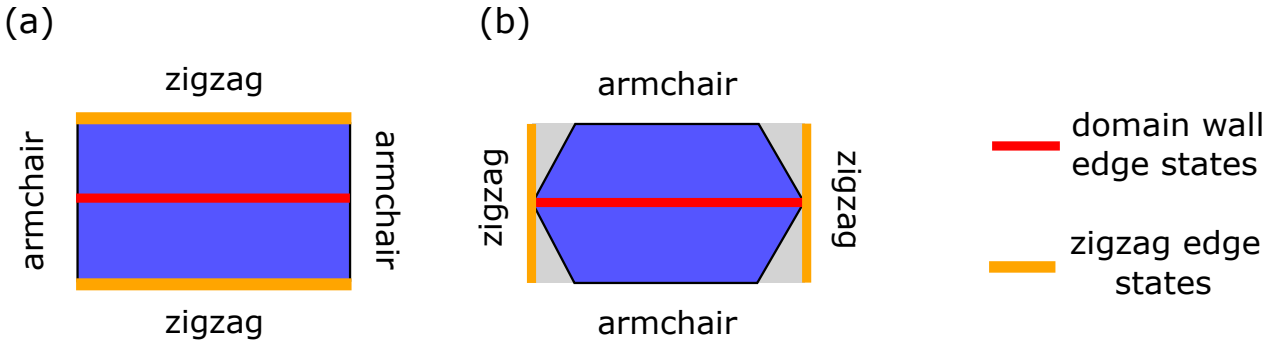

Figure 5.4: Schematics of the designed samples. The zigzag edge states are represented in orange and the Semenoff edge states are represented in red. For the zigzag domain wall (a) the two edges do not meet whereas in the armchair domain wall case (b), the Semenoff edge states mix with the zigzag edge states for a rectangular shape. The blue shape shows the designed shape without zigzag edge states mixing with the Semenoff edge states.

the edges of the sample with the armchair domain wall to have armchair edges. The final design is presented in figure 5.5 with 574 sites for the zigzag domain wall sample and 480 sites for the armchair domain wall.

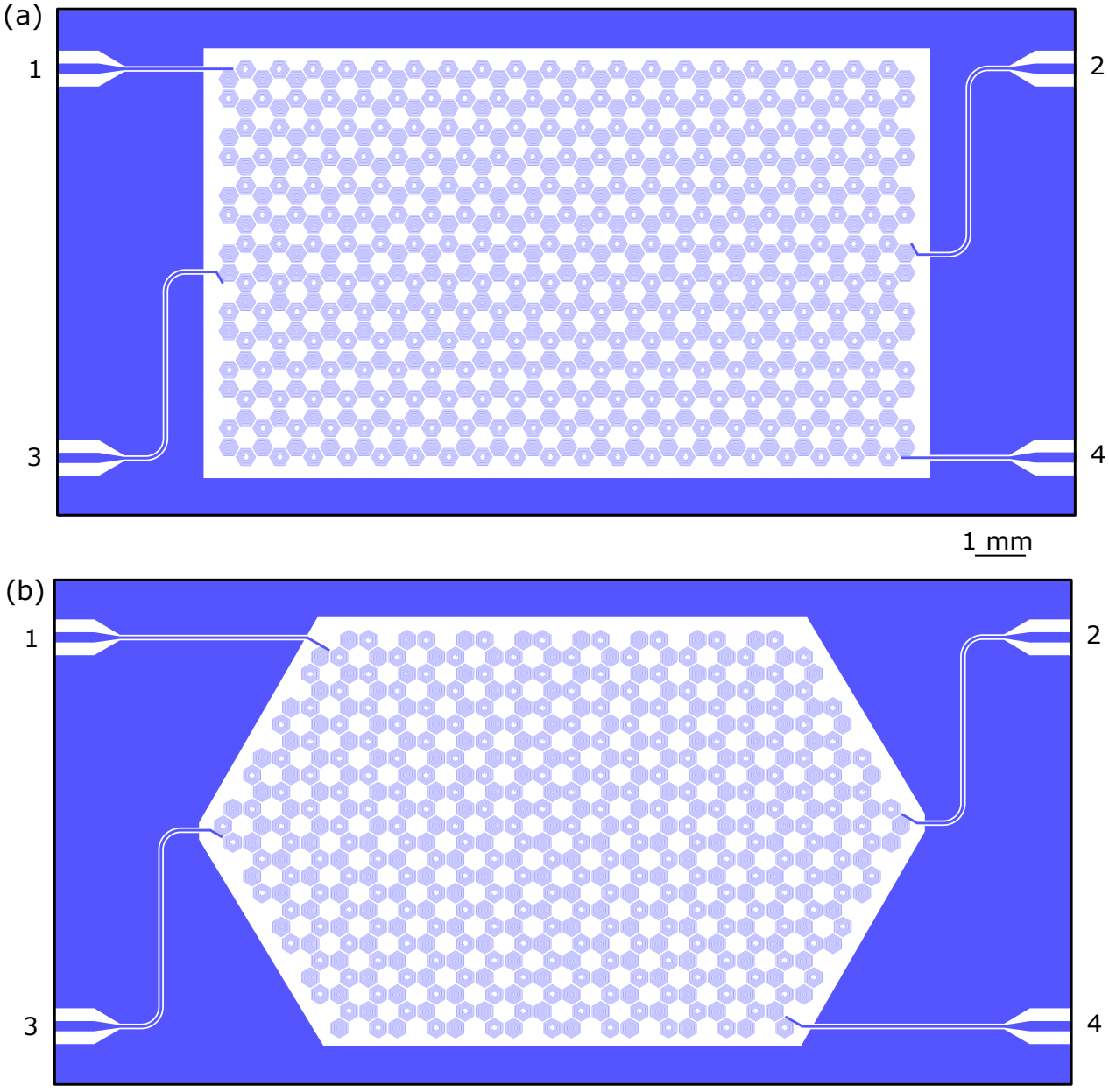

Figure 5.5: Mask design to observe the Semenoff edge states between two Semenoff insulators. (a) Zigzag domain wall and (b) Armchair domain wall. Two probing lines are coupled to the ends of the domain wall. The two other are coupled to a corner site of the lattice. The zigzag (resp. armchair) is composed of 574 (480 resp.) spiral resonators.

5.2 Transmission measurement

The lattices presented in figure 5.5 have been fabricated like the **HoneycombSi** sample with the process described in Appendix A. Out of several samples, we have measured 3 distinctive ones: **ZigzagSi**, **ZigzagSa** and **ArmchairSi** where zigzag/armchair stands for the design and Si/Sa for the substrate Silicon/Sapphire. In this section, we present the characterization of this three samples using the **setup B** described in chapter 3.

The transmission measurements are shown in figure 5.6. These measurements have been taken with the microwave **setup B** in a 1 GHz band between 5.7 GHz and 6.7 GHz with a resolution bandwidth of 1 kHz. Figure 5.6 presents the two main transmissions: the bulk transmission and the domain wall transmission. In the bulk transmission, two bands appear separated by a gap of $2\mu \simeq 120$ MHz depicted by a light gray area. For the domain wall transmission, this region presents peaks related to the edge states. Like the **HoneycombSi** sample, the two bands are asymmetric with the lower band having a smaller span that the upper band. For the sample **ArmchairSi**, we can also notice that the lower band presents less peaks and lower intensity than the upper band.

5.3 Density of states and band structure of bulk states

We have counted the number of peaks for each sample with the same method as for the **HoneycombSi** sample described in section 4.2. The resulting DOS is shown in figure 5.7. For the zigzag design, we identify $\simeq 80\%$ of the expected number of peaks. Whereas for the armchair case, this number is reduced to $\simeq 65\%$. The figure 5.7 (b) shows most missing peaks lie in the lower band. This indicates that modes in the lower band are less coupled to the transmission lines than the ones in the upper band. The DOS fitted using the points of interest is plotted as a solid line. The expression of the tight-binding parameters as a function of the point of interest frequencies are:

$$f_0 = \frac{1}{6}\left(f_{\min} + f_{\max} + 2f_D^- + 2f_D^+\right) \tag{5.3.1}$$

$$\mu = \frac{1}{2}\left(f_D^+ - f_D^-\right) \tag{5.3.2}$$

$$t_1 = \frac{1}{8}\left(\sqrt{(f_{\max} - f_{\min})^2 - 4\mu^2} + \sqrt{(f_l^+ - f_l^-)^2 - 4\mu^2}\right) \tag{5.3.3}$$

$$t_2 = \frac{1}{9}\left(\frac{f_D^+ + f_D^-}{2} - \frac{f_{\max} + f_{\min}}{2}\right) \tag{5.3.4}$$

$$t_3 = \frac{1}{24}\left(\sqrt{(f_{\max} - f_{\min})^2 - 4\mu^2} - 3\sqrt{(f_l^+ - f_l^-)^2 - 4\mu^2}\right) \tag{5.3.5}$$

The parameters obtained by fitting the DOS are summarized in table 5.2. They show a good agreement with the coupling parameters obtained from the admittance matrix and CMT calculations and are close to the target parameters given in table 5.1.

5.3.1 Bulk mode images

The mode imaging of the sample **ZigzagSi** and **ArmchairSi** is done with the optical **setup B** described in chapter 3. The measurements are done with an alignment around the four

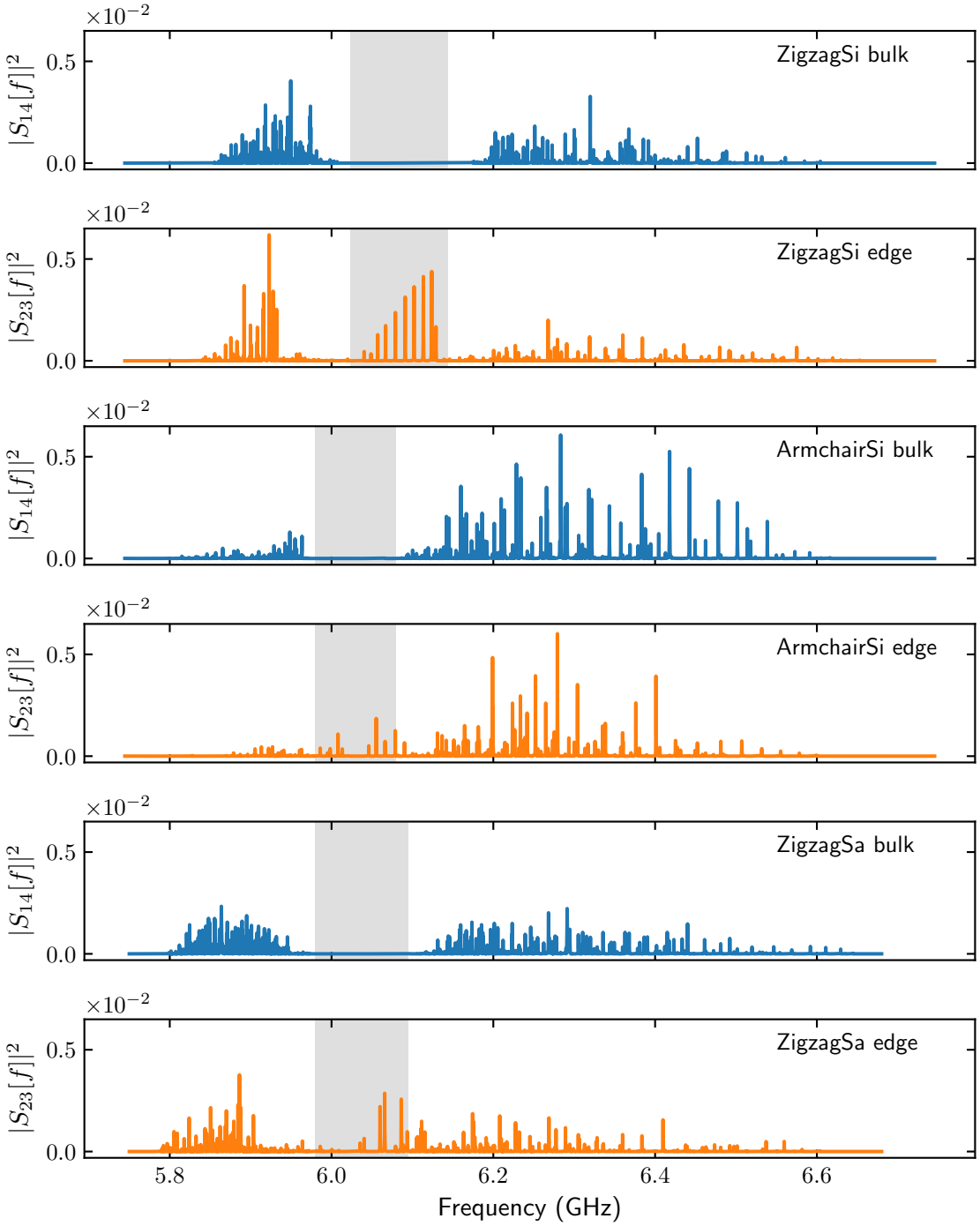

Figure 5.6: Transmission measurements for the three Semenoff samples. The grey area represents the gap of the system. For all three samples, modes appears in the domain wall transmission compared to the bulk transmission. Both transmissions are renormalized by the attenuation and the amplification of the probing line.

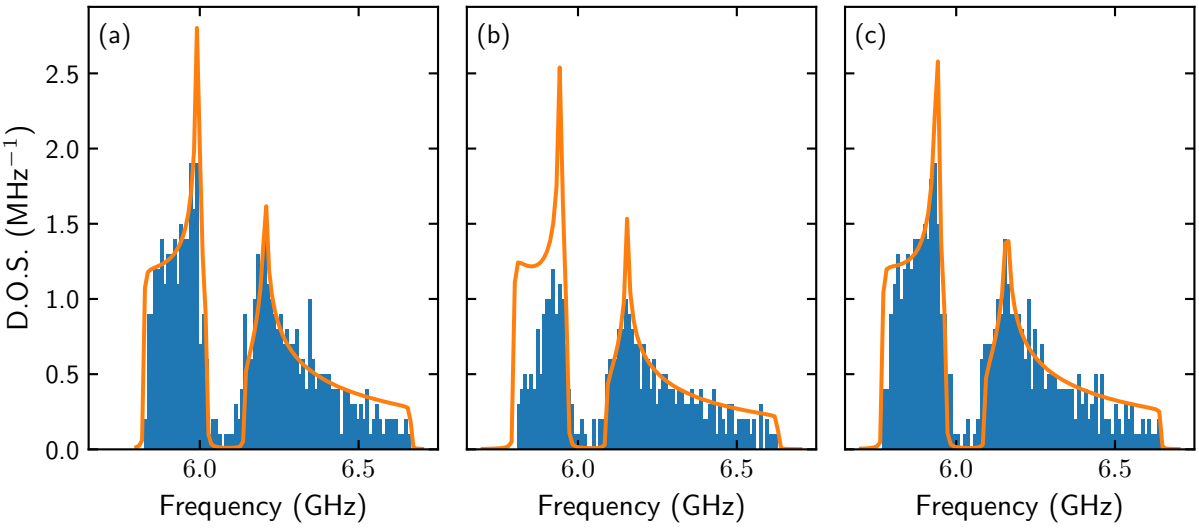

Figure 5.7: DOS for (a) **ZigzagSi**, (b) **AmrchairSi** and (c) **ZigzagSa**. The blue histogram counts the number of detected peaks in bins of 10 MHz. The orange solid line shows the lattice DOS of an infinite Semenoff insulators that has the same frequency positions for the points of interest than the measured DOS. The curve is renormalized such that integration over the full bandwidth gives the number of resonators (574 for zigzag, 480 for armchair).

	f_0 (GHz)	μ (MHz)	t_1 (MHz)	t_2 (MHz)	t_3 (MHz)
Si zigzag	6.136	58	126	−18	12
Si armchair	6.091	60	124	−20	13
Sapphire zigzag	6.089	60	132	−20	13
Admittance model	5.98	60	120	−18	10

Table 5.2: Coupling parameters obtained by extracting the frequencies of a the points of interest in the DOS.

corners and a central region of the lattice. The sampling of the lattice is realized by taking 6 points per resonators and 6 points per empty cell between the resonators. A few modes of the upper bands are shown in figures 5.8 and 5.9 for **ZigzagSi** and **ArmchairSi**. The sign is retrieved using the same technique described in section 4.2 with a linear combination of 3 theoretical modes obtained from a tight-binding simulation on finite size lattice with the parameters obtained in table 5.2.

5.3.2 Band structure of the bulk

The mode imaging allows us to associate a wavevector $\boldsymbol{k}$ to each peak observed in the transmission by doing a Fourier transform as described in section 4.2. The band structure is represented in figure 5.10 using the norm of the obtained wavevector $|\mathbf{k}|$. The result is compared to several models. The black solid line is the band structure obtained for an infinite lattice with the parameters determined in table 5.2. The gray line is obtained through admittance matrix simulation with two ports per resonator. We can see that the tight-binding model is close to the experimental data. However, the upper band does not match exactly.

The two *ab initio* models reproduce very well the experimental data. The admittance model is plotted as is for the **ArmchairSi** sample and with an offset for the **ZigzagSi** sample. For the CMT models, the frequency of the bare resonators were adjusted to match the observed gap for both samples. To complete the band structure analysis, we also consider the x and y components of the measured wavevectors to estimate the band structure as a function of k_x and k_y. Figure 5.11 shows the interpolated band structure of the **ZigzagSi** and the **ArmchairSi** samples in the 2D Brillouin zone. The interpolation is done using a simple linear interpolation between the data points.

5.4 Zigzag edge states

The **ZigzagSi** sample has two zigzag boundaries that can host zigzag edge states. As the probing line are coupled to the corner of the lattice, we have been able to measure some of them. They are shown in figure 5.12. As expected, these modes occupy only one sublattice.

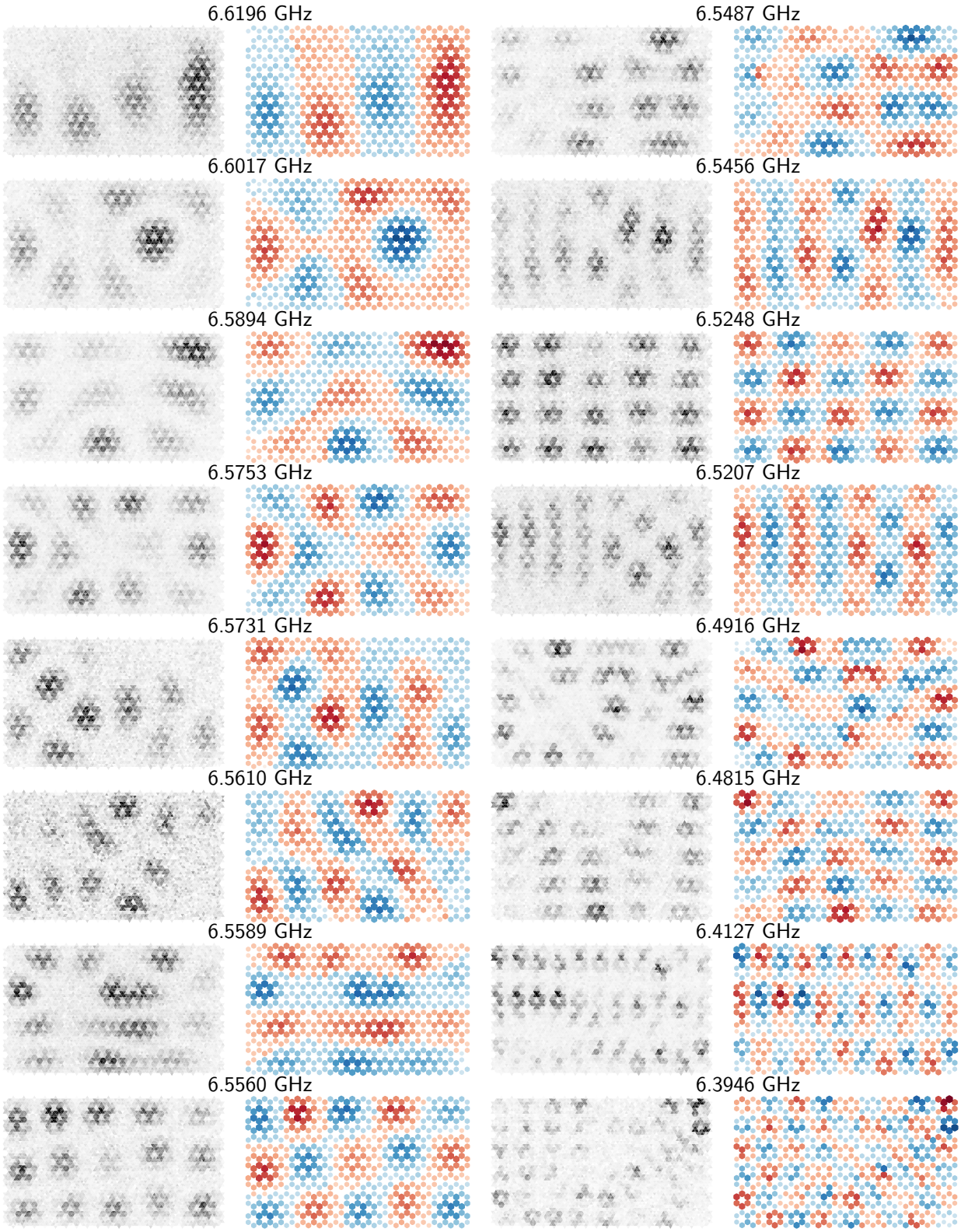

Figure 5.8: Images of modes in the upper band of the **ZigzagSi** sample. Besides each measured mode image is the reconstructed mode with the sign obtained by the method described in section 4.2.

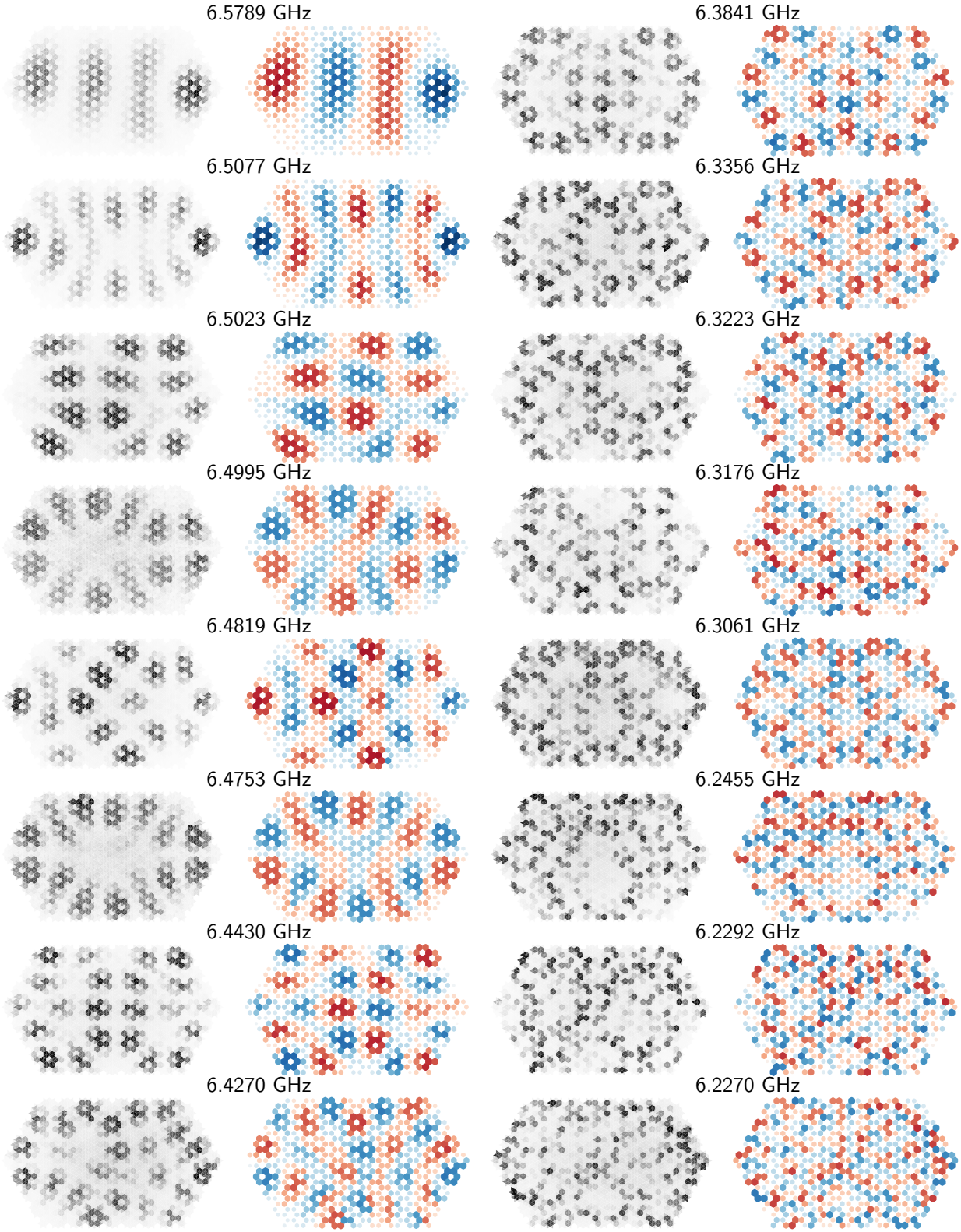

Figure 5.9: Spatial dependence of modes in the upper band of the **ArmchairSi** sample. See figure 5.8

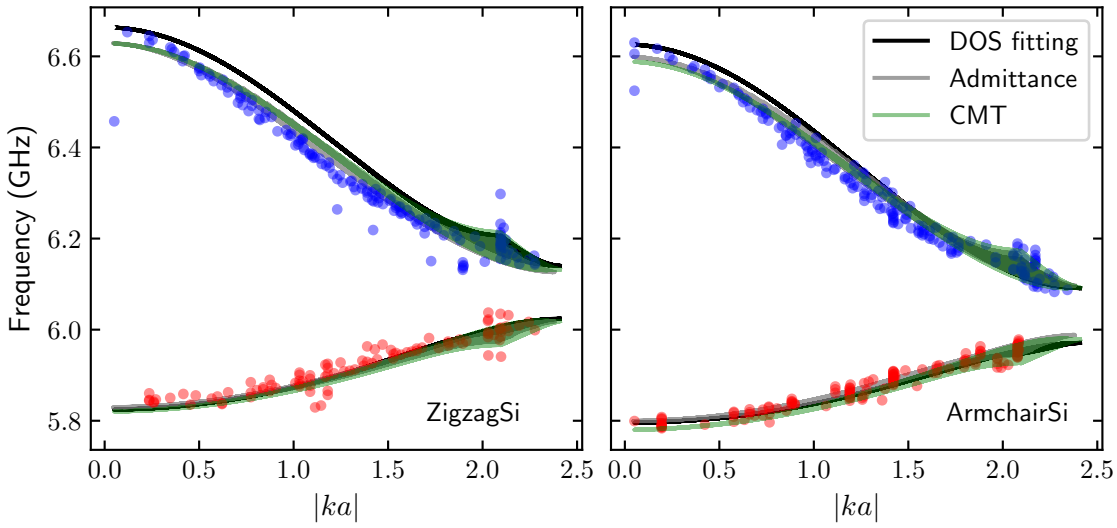

Figure 5.10: Bulk band structure of the Semenoff samples. The plot shows the band structure as a function of the norm of the wavevectors $|\mathbf{k}|$. The black line is the band structure calculated from the parameters obtained in table 5.2. The gray line is the band structure calculated from the admittance model. The green curve is calculated with the CMT model.

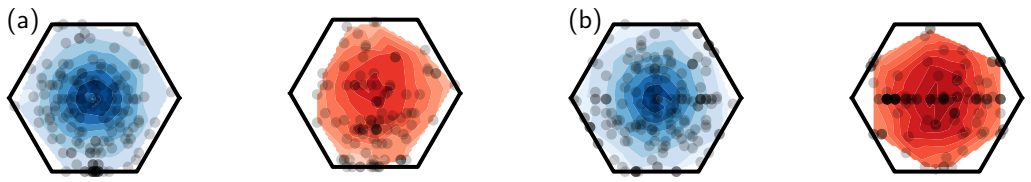

Figure 5.11: Interpolated band structure of the (a) **ZigzagSi** and (b) **AmrchairSi** sample. The blue surface represents the upper band and the red surface the lower band. Each dot represent a mode obtained by the mode imaging. We see that the upper band is well sampled whereas the lower band is more sparsely sampled.

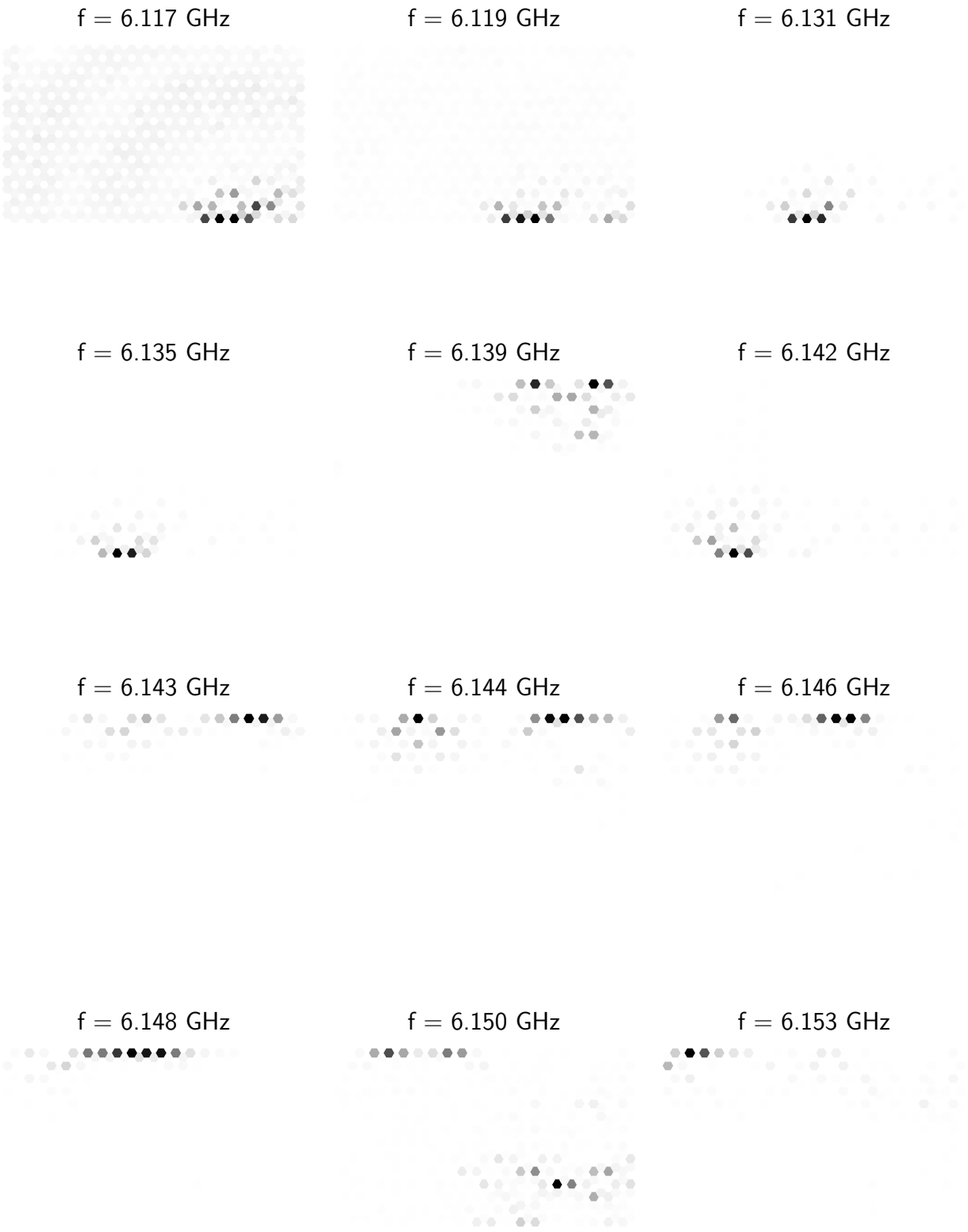

Figure 5.12: Observed zigzag edge states of the sample **ZigzagSi**. As expected, these edge states occupy only one sublattice (here A).

5.5 Characterization of the Semenoff edge states

We now focus on the measurement of the Semenoff edge states and their characterization. We first analyze the transmission spectrum along the domain wall. We then use the mode imaging to reconstruct their spatial distribution to confirm their localization near the domain wall. The mode imaging also allows us to reconstruct their band structure as well as their penetration length. We compare them with the theoretical models developed in chapter 1 using the parameters of table 5.2 and we additionally compare them to finite size tight-binding calculations.

5.5.1 Edge state transmission

In the transmission measurement plotted in figure 5.6 we have seen that peaks appear in the gap of the Semenoff insulator when probing the transmission along the domain wall. A closer look to these spectra reveal several peaks represented in figure 5.13. The **ZigzagSi** presents regularly spaced peaks with monotonic amplitude. To understand this result, the theoretical transmission using the parameters of table 5.2 is shown in figure 5.13.

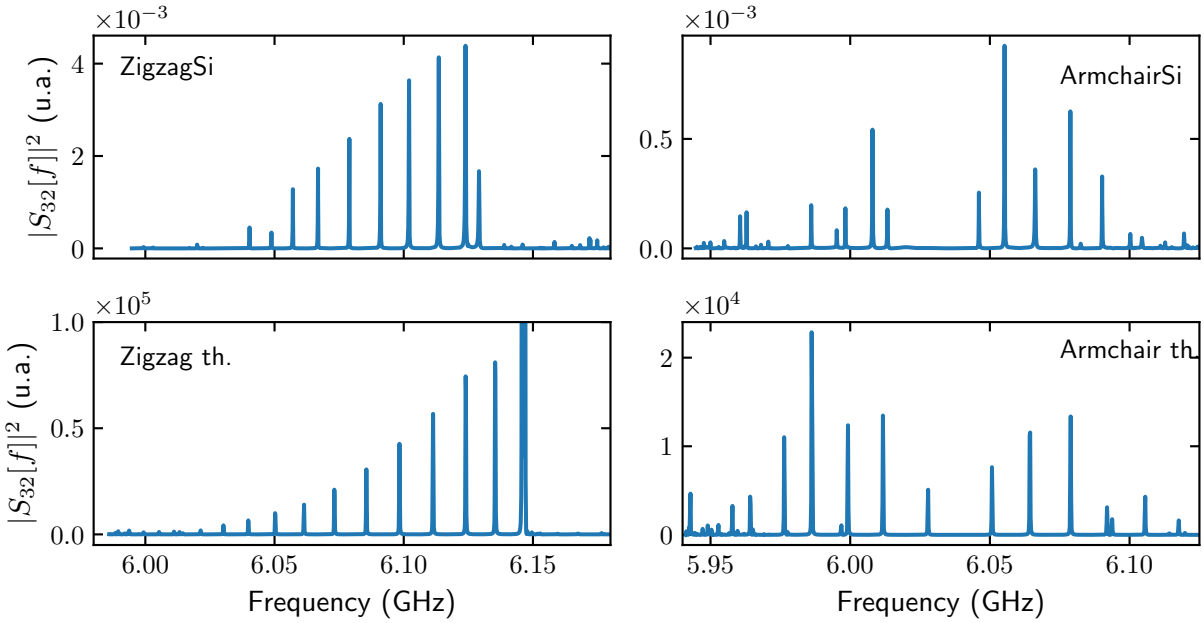

Figure 5.13: The first row shows the measured transmissions of the edge states. The second row shows the Green function from one side of the domain wall to the other calculated with the finite size tight-binding model. The Green functions reproduce the observed transmission in the zigzag case. In the armchair case, the model does not seem to capture well the edge state amplitudes.

5.5.2 Measured band structure

Mode images are shown in figures 5.14 and 5.15 for both the **ZigzagSi** and **ArmchairSi** samples. Their measurement is done by using the continuous scan described in section 3.4. In both cases, the edge states are localized near the domain wall and present periodicity along the domain wall. For the zigzag case, the penetration length of the state strongly depends on the energy of the observed mode whereas for the armchair states, the penetration length is rather the same for all observed modes. In the first few modes at low energy of the zigzag domain wall, we observe some defects that interact with the edge states.

In order to obtain the band structure of the modes, we first integrate the spatial distribution of the mode to obtain a longitudinal profile $|\Psi(x)|^2$ as a function of the coordinate x along the domain wall (see figures 5.14 and 5.15). The dispersion relation of the modes is obtained from a Fourier transform of these longitudinal profiles. For the armchair domain wall, the periodicity is twice the periodicity of the lattice and the primitive cell is a 4 site cell. The band structures are plotted in figure 5.16 with the analytic band structures obtained with the Dirac equation (see section 1.4 and with the infinite NN tight-binding model (see section 1.5). We also show the results of a calculation on a finite size lattice. We do not observe as many modes as expected. One reason may be that the modes with large wavevectors have the largest penetration length and mix more easily with bulk modes, making them harder to identify.

5.5.3 Measured penetration length

In chapter 1, we have seen that a rough estimate of the localization length $\xi(k)$ is given by the ratio of the NN hopping energy to the Semenoff mass, $\xi_0 = \frac{3ta}{4\mu}$. We have also shown that the penetration length depends on the domain wall geometry. For a zigzag domain wall, the penetration length strongly depends on the wave vector k and presents a linear behavior near the Dirac point. But, in the armchair case, the penetration length is almost independent on the wave vector. The figure 5.17 shows the decay of the edge states. As can be seen on this figure, the penetration length of the zigzag sample varies much more than for the armchair sample. The values of ξ deduced from an exponential fit are shown in figure 5.18 as well as the theoretical penetration length for the low energy model (dashed line) and the penetration length predicted by with an infinite tight-binding model (blue solid line).

The experimental values of the penetration length ξ agree well with the theoretical expectations. For the zigzag sample, we see that the finite size of the system bends the curve $\xi(k)$ in agreement with the data. For **AmrchairSi**, there is a clear difference between the infinite model (blue curve) and the finite size model (red curve) due to the shape of the sample near the gap edges. However, we were not able to observe edge states in these frequency ranges.

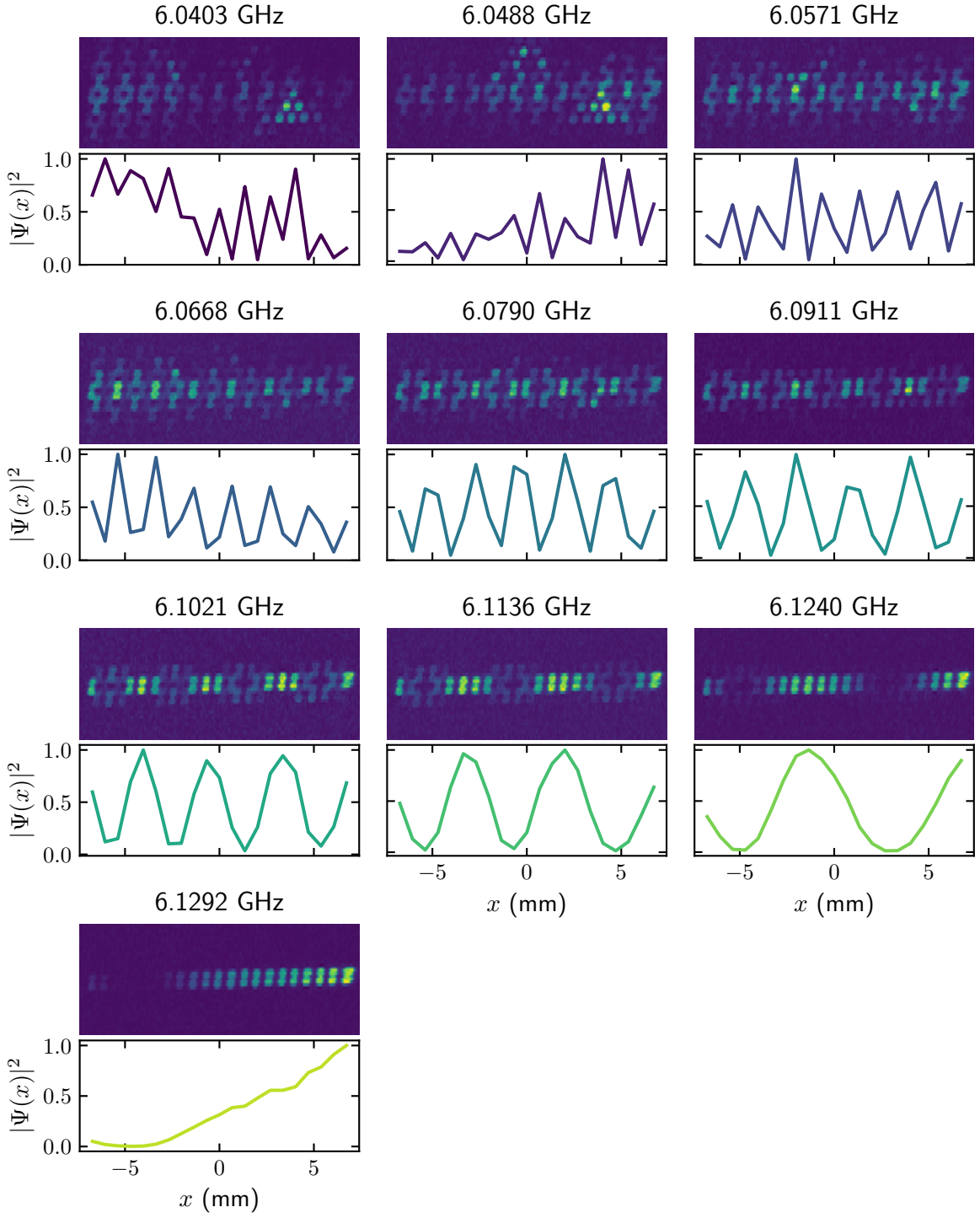

Figure 5.14: Profile of the edge states along the domain wall for **ZigzagSi**. The modes are organized by ascending frequency. The modes present clear periodicity.

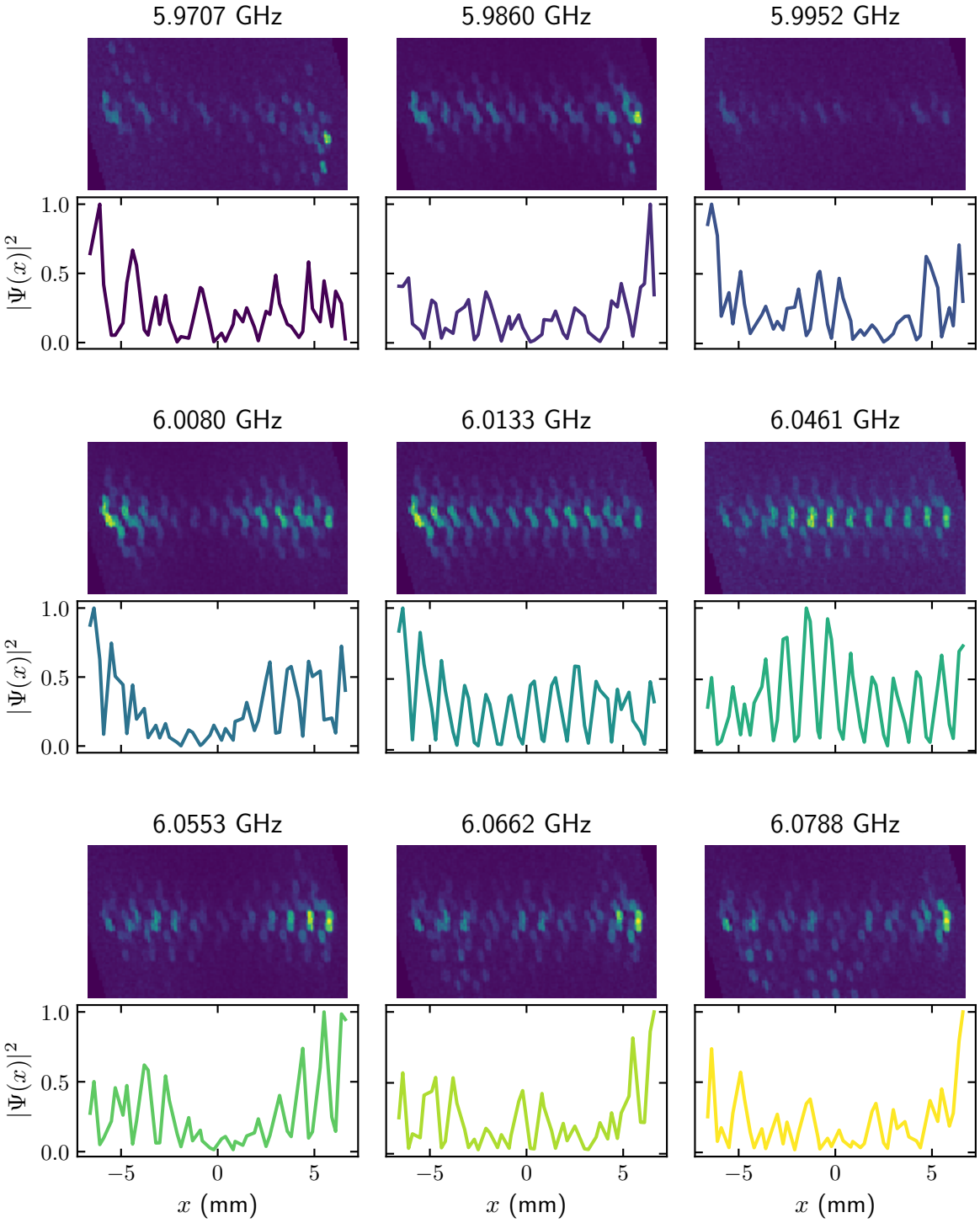

Figure 5.15: Profile of the edge states along the domain wall for **ArmchairSi**. The modes are organized by ascending frequency. For this system, the periodicity of the domain wall is twice the periodicity of the lattice

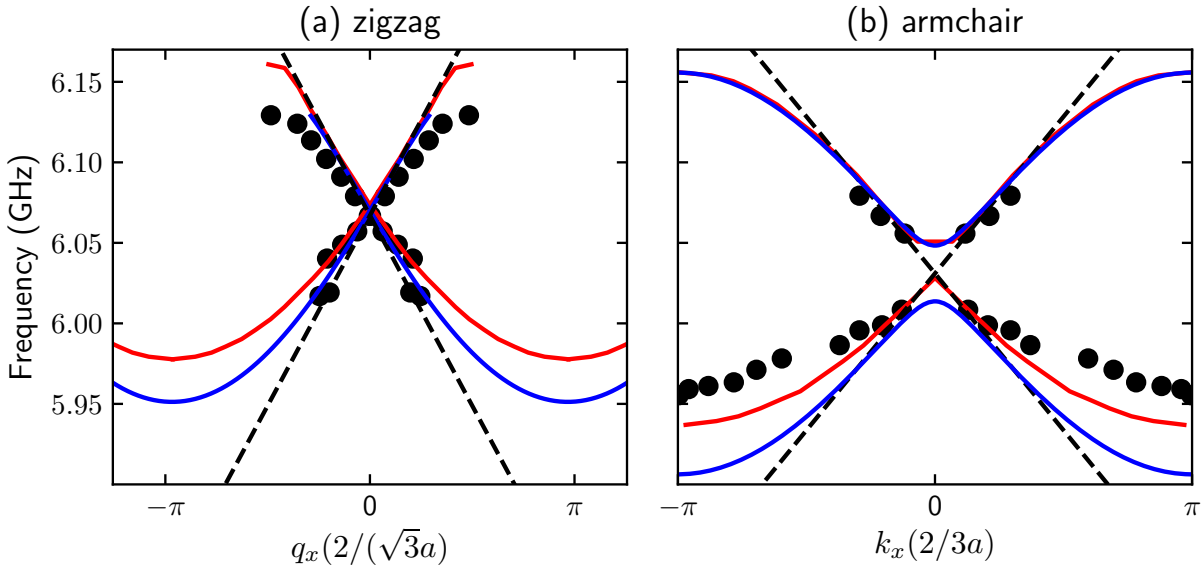

Figure 5.16: Band structure of the edge states. The dots indicate the measured modes. Three models are plotted: the dashed line corresponds to the low energy model (see section 1.4) with a slope given by the Fermi velocity. The blue is the analytic result for an infinite tight-binding (see section 1.5). The red is the result of a tight-binding numerical calculation on a finite lattice with the parameters of table 5.2.

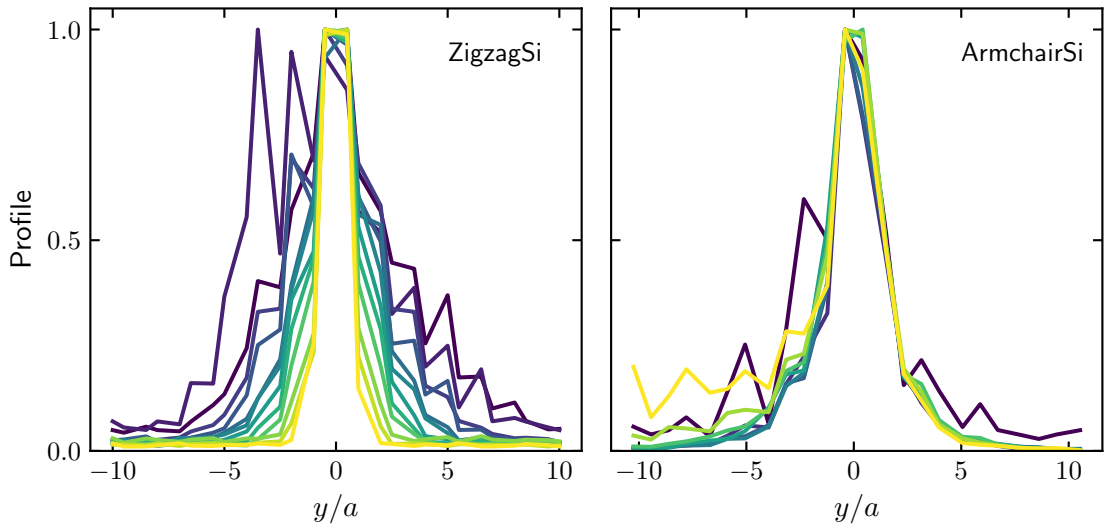

Figure 5.17: Profile of the edge states in the direction orthogonal to the domain wall. The colors correspond to the modes in figures 5.14 and 5.15. For the **ZigzagSi** sample, we see that the decay is different from mode to mode whereas for the **ArmchairSi** sample, the decay is almost the same for all the measured modes. For the **ZigzagSi** sample, one mode has a large weight not centered on the domain wall. This is due to a defect that affects this particular mode.

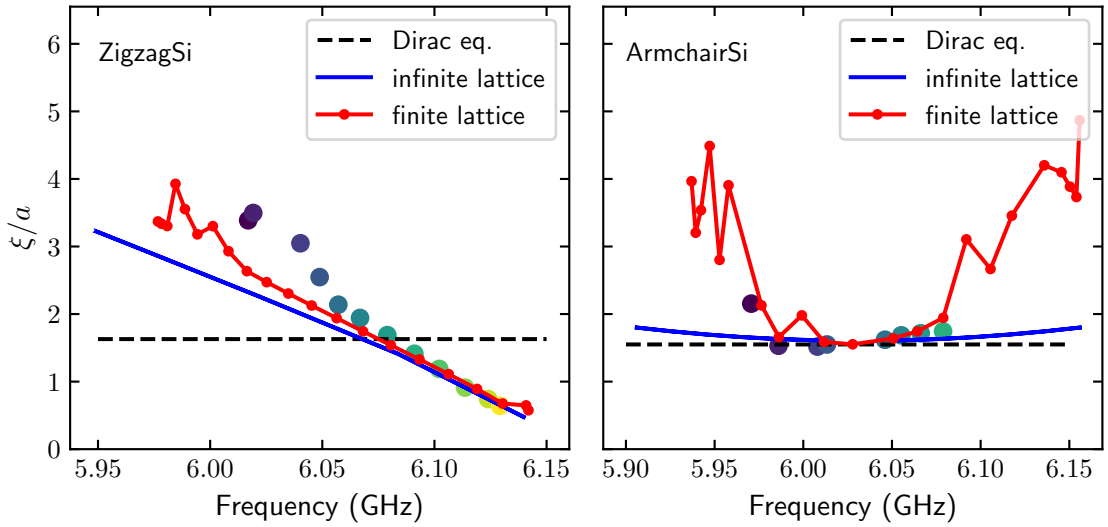

Figure 5.18: Penetration length ξ of the edge states in cell unit. The dot colors correspond to the curves in figure 5.17. Three models are plotted: the dashed line is the low energy model (see section 1.4). The blue is the analytical result for an infinite tight-binding (see section 1.5). The red is the tight-binding numerical calculation done for a finite lattice with the parameters of table 5.2.

5.6 Observation of localized states induced by defects

During the fabrication of the sample, some defects appear in the lattice. The kind of defects that change most the lattice are metallic scraps that fall back on some resonators during the lift-off. This usually creates a short between two meanders of the spiral, decreasing its effective length and thus increasing the resonance frequency. For large shifts, this results in a vacancy in the lattice. The effect of a single vacancy on a honeycomb lattice in the tight-binding approximation was studied by Pereira et al. [82]. They show that such vacancies induce localized states around the defect and that the energy of these defect is close to $E = 0$. Moreover, these states only occupy the sublattice opposite to the defect site.

5.6.1 Identification of the defects

Optical inspection of the sample with a microscope usually reveals a few defects in the lattice. The defects spotted on the sample **ZigzagSi** are shown in figure 5.19. In order to see if we are able to spot these defect with the mode imaging, we look for sites in the lattice that are weakly populated when summing over all modes. The plot on the right of figure 5.19 shows the average mode amplitude of each site over all the measured modes. To make the defect appear more clearly, we have increased the contrast. This map reveal 5 defects in the bulk that are connected to visible defects as shown in the right panel.

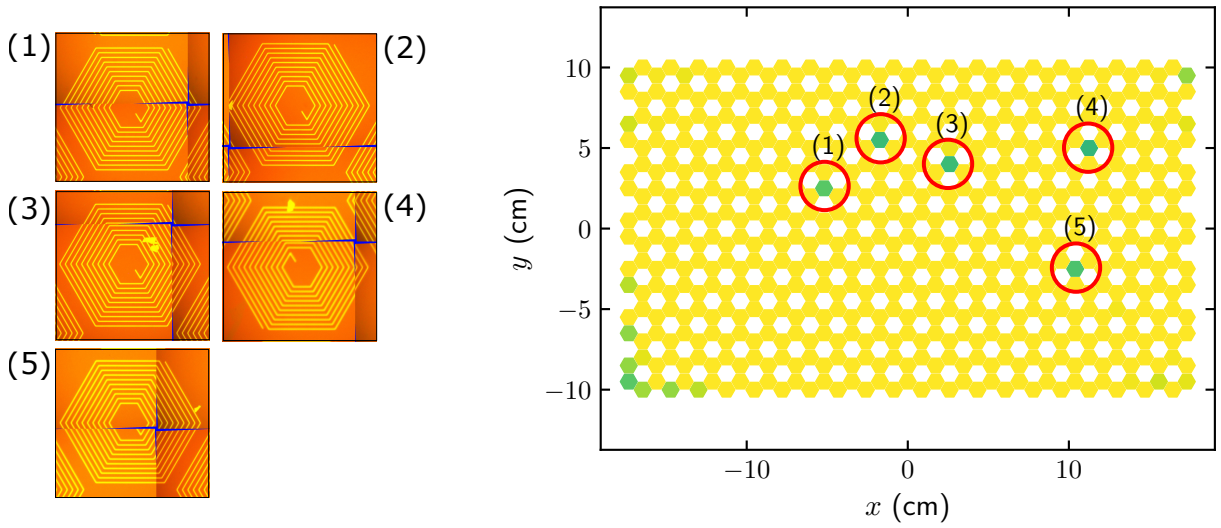

Figure 5.19: The left panel shows the optical image of the defects. The right panel shows the average of the weight of the modes squared with an increased contrast to see the defect.

5.6.2 Localized defect states

Pereira et al. [82] have shown that the localized modes around a defect are zigzag-like states where the mode is localized on the sublattice opposite to the one of the defect. They have found in the infinite lattice approximation that the wave function with a defect on the sublattice B behaves as:

$$\Psi_A(x,y) \simeq \frac{e^{(4\pi i x)/(3\sqrt{3})}}{y+ix} + \frac{e^{2\pi i(y+x/\sqrt{3})/3}}{y-ix} \quad \text{and} \quad \Psi_B(x,y) = 0 \tag{5.6.1}$$

where x and y are the coordinates with respect to the position of the defect. We have run simulations with a single defect to confirm that adding a Semenoff mass and NNN coupling does not change the localization of these states. The results with the parameters of table 5.2 are shown in the last row of figure 5.20 and we indeed observe a localized mode near the defect. Localized states are usually not coupled to the edge. However, due to the finite size of the sample, some of the defect modes are coupled to the probing lines and can be observed. The images of these modes are shown in figure 5.20. They are localized near the defects revealed in figure 5.19. Figure 5.20 shows the decay of theses modes. We see that these localized modes have a typical size of two sites and form a triangular shape around the defect, exactly like predicted by the finite size simulation.

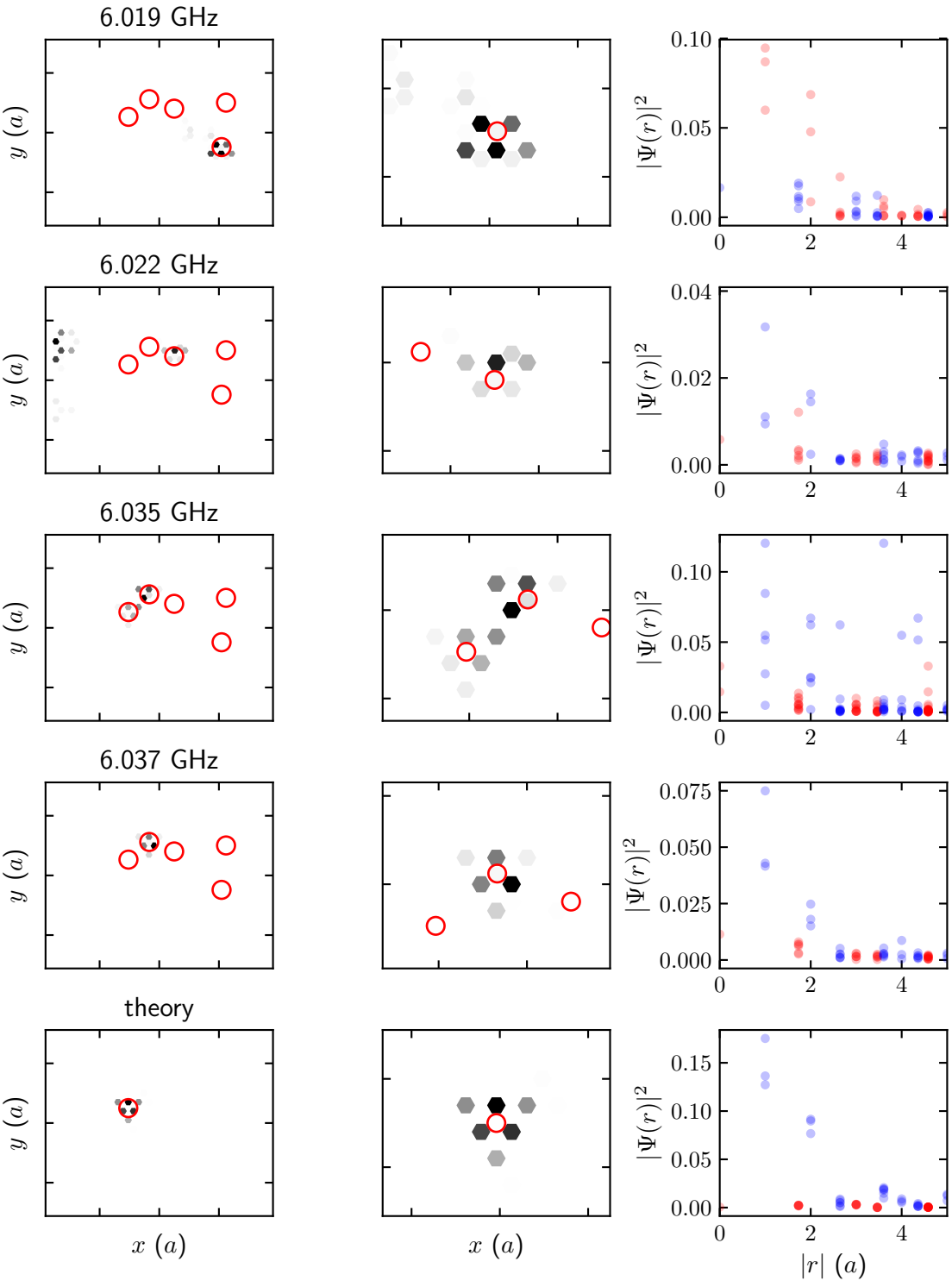

Figure 5.20: Observed defect modes $|\Psi(\mathbf{r})|^2$. The first colon is the full mode, the second colon shows a zoom onto the mode. The last colon shows the wavefunction $|\Psi(\mathbf{r})|^2$ as a function of the distance to the defect observed in figure 5.19. Each color represents a sublattice. The last row presents a theoretical mode calculated from a tight-binding model with one defect.

Conclusion

In this chapter, we have probed the physic of topological edge states in a lattice of superconducting resonators realizing a domain wall between two Semenoff insulators with opposite masses. In addition to show their presence in the gap, we have been able to fully characterize their band structure and their penetration length for two different geometries. The agreement between our measurements and the theory proves our ability to successfully design lattices in order to observe specific topological effects.

Conclusions and perspectives

This thesis work aimed at using superconducting circuits to simulate condensed matters systems. We chose to design and realize a honeycomb lattice and a Semenoff insulator. The main interest of the Semenoff insulator is the existence of a topological charge for each valley. When two Semenoff insulator are put side by side these topological charges insure the existence of edge states in the gap of the insulator. The realization and observation of these two lattices constitute a demonstration of the ability of superconducting circuits to explore specific topological effects. The first point (see chapter 1) of this thesis was to determine the range of parameters allowing to study these effects. Then, to have a faithful description of the superconducting lattices, we have developed in chapter 2 two models that rely on numerical simulation of a single or a few resonators. The first model uses the admittance matrix calculated on a small subregion and periodizes it to obtain the band structure. The second model relies on the coupled mode theory to calculate the band structure. From an experimental point of view, in order to probe the spatial dependence of the mode wavefunctions in the lattice of resonators, we have developed in chapter 3 a mode imaging technique based on the creation of a local loss with a laser. With this technique, we have observed several modes of a honeycomb lattice (chapter 4) and of Semenoff insulators (chapter 5) leading to the reconstruction of the band structure of these lattices. For the three lattices imaged in this thesis, we have a good agreement between the measured band structures and the calculated ones. We also observe the edge states on the zigzag and bearded edge of the honeycomb lattice as well as the Semenoff edge states. For both, we have measured their band structure and their penetration length and we have a good agreement with tight-binding predictions. A question to answer is why the sapphire lattice did not work. At the time of writing of this thesis, we did not have enough time to investigate more thoroughly, but the Sapphire substrate seems to offer different conditions of mode imaging as it is TLS free. Another challenge for the mode imaging is the information on the phase between each site. In our case, the phase is just a sign, but in some situation it can be any angle. There have been implementation of a phase sensitive measurement of superconducting resonators by Karpov et al. [83], however, they rely on an amplitude modulation of the laser at a frequency close to the resonance frequency of the resonators and requires a better modulation setup than we have. As a follow-up of these experiments, several systems with the same spiral resonators can be considered and implemented: a kekulé distortion [70] or pseudo-magnetic field using inhomogeneous coupling [47, 84–86]. In a broader perspective, a topological matter cornerstone is the time reversal symmetry. Breaking this symmetry leads to non-zero Chern numbers and chiral edge states. The superconducting resonators offer a possibility to realize this by using modulated cou-

pling [18, 87] or by using a specific configuration of a Josephson junction [9]. However its implementation on large arrays remains a challenge for superconducting circuits. A second main direction is the use of Josephson junctions or high kinetic inductance materials ([88–90] for their non-linearity in order to enter the strong interaction regime. This interaction term allows to explore the physics of photonic Mott insulators [20] and paves the way to quantum simulation.

Appendices

Appendix A

Sample fabrication

A.1 Fabrication

The superconducting resonators presented on figure 4.4 are made of niobium on a oxide silicon substrate. Niobium is a conventional BCS superconductor largely used for thin films deposit. It has a critical temperature $T_c = 9.2\,\mathrm{K}$ which allow to work easily on the 1 K plate of a dilution fridge or in a pumped Helium fridge. It also yields good quality factors ($Q > 10^5$) for GHz resonators at theses temperature. The niobium film is homogeneously deposited over the whole wafer by sputtering. The pattern is realized with optical lithography with a chrome mask and then etched with Reactive Ion Etching (RIE). Figure A.1 presents a detailed list of the fabrication steps of the fabrication process:

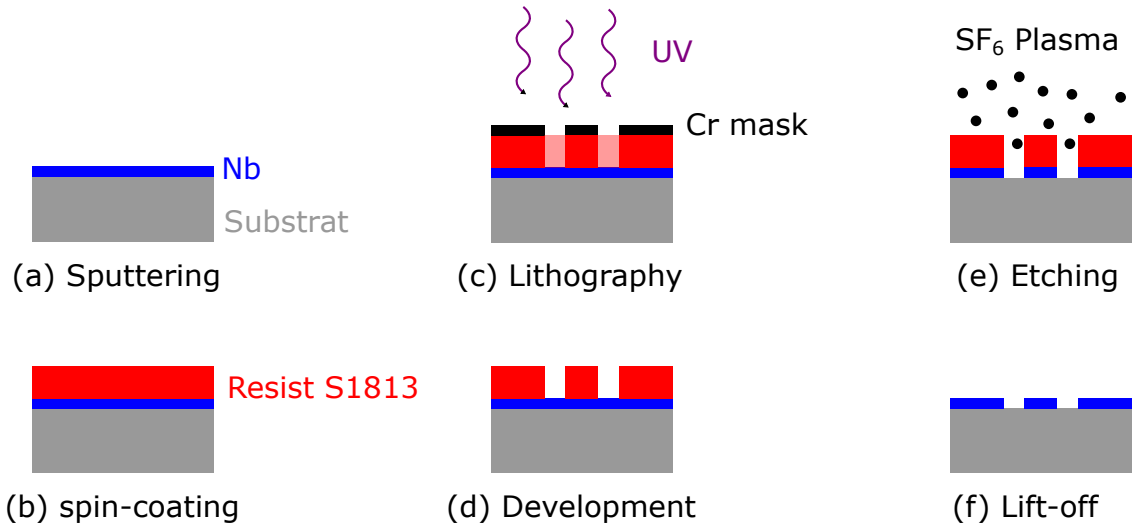

Figure A.1: Fabrication process of the chip. The Nb deposit was done at LPS Orsay in a Plassys sputtering chamber. The optical lithography and the etching is done at C2N Orsay

- Cleaning of the sapphire wafer in piranha acid for 10 min to remove dust. For Silicon wafer, the wafer were sufficiently cleaned to be processed right away.
- (a) Deposit of 250 nm of Nb at a rate of $\sim 1.4\,\mathrm{nm}\cdot\mathrm{s}^{-1}$ by sputtering technique.

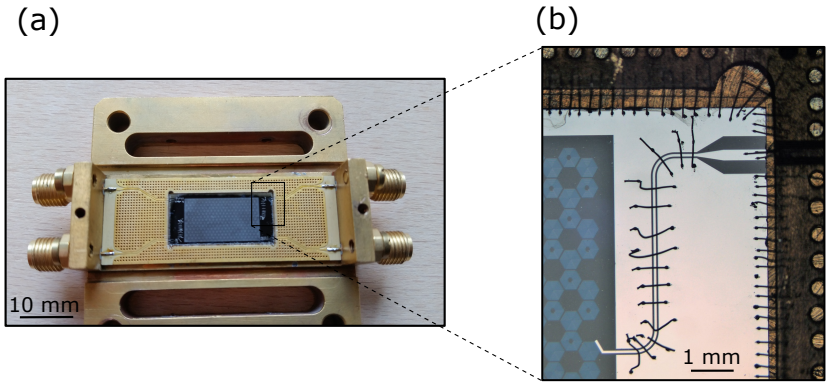

Figure A.2: (a) Sample holder with PCB soldered on top. The sample holder is made out of plain copper. The sample holder has been gold platted in order to avoid oxidization of the copper. (b) Zoom on the wedge bonding of the sample. The edges of the chip are wedge bonded to the ground plane of the PCB. each sides of the CPW transmission line are wedge bonded in order to avoid inhomogeneity in the ground plane.

- (b) Spin-coating of the wafer with the photo-resist Shipley S1813 followed by baking on a hot plate at 110 °C for 1 min.
- (c) Lithography of the pattern with UV exposure through the chrome mask in hard contact on a manual mask aligner (MJB4 - SÜSS MicroTec).
- (d) Development in pure MF319 developer to remove the exposed resist.
- (e) Reactive ion etching using SF_6 plasma. The end of the etching process is determined by optical setup. Typically, the etching last 6 min.
- Dicing of the wafer with a diamond saw.
- Deposition of a Nb back plain.
- (f) Removal of the remaining resist in hot bath (60 °C) of acetone.

The chips are then examined in order to check if the probing transmission lines are well defined and to count the number of defective resonators (usually some non-etched metallic part shortening two lines of a resonators).

A.2 Sample holder

The sample is fixed onto the sample holder with silver glue. The microwave lines and the ground plane are wedge bonded to the PCB figure A.2. Wedge bonding all around the chip and over the CPW lines allow for a good ground definition and remove some parasitic effect due to propagation in the ground plane.

Bibliography

[1] R. P. Feynman, “Simulating physics with computers”, International Journal of Theoretical Physics **21**, 467–488 (1982).

[2] A. Trabesinger, “Quantum simulation”, Nature Physics **8**, 263–263 (2012).

[3] D. C. Tsui, H. L. Stormer, and A. C. Gossard, “Two-Dimensional Magnetotransport in the Extreme Quantum Limit”, Physical Review Letters **48**, 1559–1562 (1982).

[4] R. B. Laughlin, “Anomalous Quantum Hall Effect: An Incompressible Quantum Fluid with Fractionally Charged Excitations”, Physical Review Letters **50**, 1395–1398 (1983).

[5] F. D. M. Haldane, “Model for a Quantum Hall Effect without Landau Levels: Condensed-Matter Realization of the "Parity Anomaly"”, Physical Review Letters **61**, 2015–2018 (1988).

[6] N. Regnault and B. A. Bernevig, “Fractional Chern Insulator”, Physical Review X **1**, 021014 (2011).

[7] S. Schmidt and J. Koch, “Circuit QED lattices: Towards quantum simulation with superconducting circuits: Circuit QED lattices”, Annalen der Physik **525**, 395–412 (2013).

[8] K. Le Hur, L. Henriet, A. Petrescu, K. Plekhanov, G. Roux, and M. Schiró, “Many-body quantum electrodynamics networks: Non-equilibrium condensed matter physics with light”, Comptes Rendus Physique **17**, 808–835 (2016).

[9] J. Koch, A. A. Houck, K. L. Hur, and S. M. Girvin, “Time-reversal-symmetry breaking in circuit-QED-based photon lattices”, Physical Review A - Atomic, Molecular, and Optical Physics **82**, 1–18 (2010).

[10] J. Koch and K. Le Hur, “Superfluid–Mott-insulator transition of light in the Jaynes-Cummings lattice”, Physical Review A **80**, 023811 (2009).

[11] A. Blais, R.-S. Huang, A. Wallraff, S. M. Girvin, and R. J. Schoelkopf, “Cavity quantum electrodynamics for superconducting electrical circuits: An architecture for quantum computation”, Physical Review A **69**, 062320 (2004).

[12] M. H. Devoret, A. Wallraff, and J. M. Martinis, “Superconducting Qubits: A Short Review”, arXiv:cond-mat/0411174 (2004).

[13] J. Koch, T. M. Yu, J. Gambetta, A. A. Houck, D. I. Schuster, J. Majer, A. Blais, M. H. Devoret, S. M. Girvin, and R. J. Schoelkopf, “Charge-insensitive qubit design derived from the Cooper pair box”, Physical Review A **76**, 042319 (2007).

[14] V. E. Manucharyan, J. Koch, L. I. Glazman, and M. H. Devoret, "Fluxonium: Single Cooper-Pair Circuit Free of Charge Offsets", Science **326**, 113–116 (2009).

[15] J. M. Chow, J. M. Gambetta, A. D. Córcoles, S. T. Merkel, J. A. Smolin, C. Rigetti, S. Poletto, G. A. Keefe, M. B. Rothwell, J. R. Rozen, M. B. Ketchen, and M. Steffen, "Universal Quantum Gate Set Approaching Fault-Tolerant Thresholds with Superconducting Qubits", Physical Review Letters **109**, 060501 (2012).

[16] M. H. Devoret and R. J. Schoelkopf, "Superconducting Circuits for Quantum Information: An Outlook", Science **339**, 1169–1174 (2013).

[17] M. Fitzpatrick, N. M. Sundaresan, A. C. Y. Li, J. Koch, and A. A. Houck, "Observation of a Dissipative Phase Transition in a One-Dimensional Circuit QED Lattice", Physical Review X **7**, 011016 (2017).

[18] P. Roushan, C. Neill, A. Megrant, Y. Chen, R. Babbush, R. Barends, B. Campbell, Z. Chen, B. Chiaro, A. Dunsworth, A. Fowler, E. Jeffrey, J. Kelly, E. Lucero, J. Mutus, P. J. J. O'Malley, M. Neeley, C. Quintana, D. Sank, A. Vainsencher, J. Wenner, T. White, E. Kapit, H. Neven, and J. Martinis, "Chiral ground-state currents of interacting photons in a synthetic magnetic field", Nature Physics **13**, 146–151 (2017).

[19] P. Roushan, C. Neill, J. Tangpanitanon, V. M. Bastidas, A. Megrant, R. Barends, Y. Chen, Z. Chen, B. Chiaro, A. Dunsworth, A. Fowler, B. Foxen, M. Giustina, E. Jeffrey, J. Kelly, E. Lucero, J. Mutus, M. Neeley, C. Quintana, D. Sank, A. Vainsencher, J. Wenner, T. White, H. Neven, D. G. Angelakis, and J. Martinis, "Spectroscopic signatures of localization with interacting photons in superconducting qubits", Science **358**, 1175–1179 (2017).

[20] R. Ma, B. Saxberg, C. Owens, N. Leung, Y. Lu, J. Simon, and D. I. Schuster, "A Dissipatively Stabilized Mott Insulator of Photons", arXiv:1807.11342 [cond-mat, physics:quant-ph] (2018).

[21] L. Lu, J. D. Joannopoulos, and M. Solja**v** cić, "Topological photonics", Nature Photonics **8**, 821–829 (2014).

[22] A. B. Khanikaev and G. Shvets, "Two-dimensional topological photonics", Nature Photonics **11**, 763–773 (2017).

[23] T. Ozawa, H. M. Price, A. Amo, N. Goldman, M. Hafezi, L. Lu, M. Rechtsman, D. Schuster, J. Simon, O. Zilberberg, and I. Carusotto, "Topological Photonics", arXiv:1802.04173 [cond-mat, physics:physics, physics:quant-ph] (2018).

[24] M. Kohmoto, "Topological invariant and the quantization of the Hall conductance", Annals of Physics **160**, 343–354 (1985).

[25] C. L. Kane and E. J. Mele, "Quantum Spin Hall Effect in Graphene", Physical Review Letters **95**, 226801 (2005).

[26] C. L. Kane and E. J. Mele, "Z 2 Topological Order and the Quantum Spin Hall Effect", Physical Review Letters **95**, 146802 (2005).

[27] B. A. Bernevig and S.-C. Zhang, "Quantum Spin Hall Effect", Physical Review Letters **96**, 106802 (2006).

[28] B. I. Halperin, "Quantized Hall conductance, current-carrying edge states, and the existence of extended states in a two-dimensional disordered potential", Physical Review B **25**, 2185–2190 (1982).

[29] M. Büttiker, "Absence of backscattering in the quantum Hall effect in multiprobe conductors", Physical Review B **38**, 9375–9389 (1988).

[30] L. Fidkowski, T. S. Jackson, and I. Klich, "Model Characterization of Gapless Edge Modes of Topological Insulators Using Intermediate Brillouin-Zone Functions", Physical Review Letters **107**, 036601 (2011).

[31] R. S. K. Mong and V. Shivamoggi, "Edge states and the bulk-boundary correspondence in Dirac Hamiltonians", Physical Review B **83**, 125109 (2011).

[32] T. Fukui, K. Shiozaki, T. Fujiwara, and S. Fujimoto, "Bulk-Edge Correspondence for Chern Topological Phases: A Viewpoint from a Generalized Index Theorem", Journal of the Physical Society of Japan **81**, 114602 (2012).

[33] A. B. Khanikaev, S. Hossein Mousavi, W.-K. Tse, M. Kargarian, A. H. MacDonald, and G. Shvets, "Photonic topological insulators", Nature Materials **12**, 233–239 (2013).

[34] M. C. Rechtsman, J. M. Zeuner, Y. Plotnik, Y. Lumer, D. Podolsky, F. Dreisow, S. Nolte, M. Segev, and A. Szameit, "Photonic Floquet topological insulators", Nature **496**, 196–200 (2013).

[35] M. Hafezi, E. Demler, M. Lukin, and J. Taylor, "Robust optical delay lines via topological protection", Nature Physics **7**, 907–912 (2011).

[36] M. Hafezi, S. Mittal, J. Fan, A. Migdall, and J. M. Taylor, "Imaging topological edge states in silicon photonics", Nature Photonics **7**, 1001–1005 (2013).

[37] H. Wang, M. Hofheinz, J. Wenner, M. Ansmann, R. C. Bialczak, M. Lenander, E. Lucero, M. Neeley, A. D. O'Connell, D. Sank, M. Weides, A. N. Cleland, and J. M. Martinis, "Improving the coherence time of superconducting coplanar resonators", Applied Physics Letters **95**, 233508 (2009).

[38] C. Owens, A. LaChapelle, B. Saxberg, B. M. Anderson, R. Ma, J. Simon, and D. I. Schuster, "Quarter-Flux Hofstadter Lattice in Qubit-Compatible Microwave Cavity Array", Physical Review A **97**, 013818 (2018).

[39] J. Ningyuan, C. Owens, A. Sommer, D. Schuster, and J. Simon, "Time- and Site-Resolved Dynamics in a Topological Circuit", Physical Review X **5**, 021031 (2015).

[40] M. Milićević, T. Ozawa, P. Andreakou, I. Carusotto, T. Jacqmin, E. Galopin, A. Lemaître, L. Le Gratiet, I. Sagnes, J. Bloch, and A. Amo, "Edge states in polariton honeycomb lattices", 2D Materials **2**, 034012 (2015).

[41] M. Milićević, T. Ozawa, G. Montambaux, I. Carusotto, E. Galopin, A. Lemaître, L. Le Gratiet, I. Sagnes, J. Bloch, and A. Amo, "Orbital Edge States in a Photonic Honeycomb Lattice", Physical Review Letters **118**, 107403 (2017).

[42] T. Jacqmin, I. Carusotto, I. Sagnes, M. Abbarchi, D. D. Solnyshkov, G. Malpuech, E. Galopin, A. Lemaître, J. Bloch, and A. Amo, "Direct Observation of Dirac Cones and a Flatband in a Honeycomb Lattice for Polaritons", Physical Review Letters **112**, 116402 (2014).

[43] U. Kuhl, S. Barkhofen, T. Tudorovskiy, H.-J. Stöckmann, T. Hossain, L. de Forges de Parny, and F. Mortessagne, "Dirac point and edge states in a microwave realization of tight-binding graphene-like structures", Physical Review B **82**, 094308 (2010).

[44] M. Bellec, U. Kuhl, G. Montambaux, and F. Mortessagne, "Tight-binding couplings in microwave artificial graphene", Physical Review B **88**, 115437 (2013).

[45] S. Yves, F. Lemoult, M. Fink, and G. Lerosey, "Crystalline Soda Can Metamaterial exhibiting Graphene-like Dispersion at subwavelength scale", (2017).

[46] M. Gibertini, A. Singha, V. Pellegrini, M. Polini, G. Vignale, A. Pinczuk, L. N. Pfeiffer, and K. W. West, "Engineering artificial graphene in a two-dimensional electron gas", Physical Review B **79**, 241406 (2009).

[47] M. C. Rechtsman, J. M. Zeuner, A. Tünnermann, S. Nolte, M. Segev, and A. Szameit, "Strain-induced pseudomagnetic field and photonic Landau levels in dielectric structures", Nature Photonics **7**, 153–158 (2013).

[48] M. C. Rechtsman, Y. Plotnik, J. M. Zeuner, D. Song, Z. Chen, A. Szameit, and M. Segev, "Topological Creation and Destruction of Edge States in Photonic Graphene", Physical Review Letters **111**, 103901 (2013).

[49] M. C. Rechtsman, Y. Lumer, Y. Plotnik, A. Perez-Leija, A. Szameit, and M. Segev, "Topological protection of photonic path entanglement", Optica **3**, 925 (2016).

[50] S. Wang, D. Scarabelli, L. Du, Y. Y. Kuznetsova, L. N. Pfeiffer, K. W. West, G. C. Gardner, M. J. Manfra, V. Pellegrini, S. J. Wind, and A. Pinczuk, "Observation of Dirac bands in artificial graphene in small-period nanopatterned GaAs quantum wells", Nature Nanotechnology **13**, 29–33 (2018).

[51] B. Dietz and A. Richter, "From graphene to fullerene: experiments with microwave photonic crystals", Physica Scripta **94**, 014002 (2019).

[52] J. C. Culbertson, H. S. Newman, and C. Wilker, "Optical probe of microwave current distributions in high temperature superconducting transmission lines", Journal of Applied Physics **84**, 2768–2787 (1998).

[53] A. P. Zhuravel, C. Kurter, A. V. Ustinov, and S. M. Anlage, "Unconventional rf photoresponse from a superconducting spiral resonator", Physical Review B **85**, 134535 (2012).

[54] A. S. Averkin, A. P. Zhuravel, A. Karpov, S. M. Anlage, and A. V. Ustinov, "Ultracompact superconductive resonator with double-spiral structure", in 2013 7th International Congress on Advanced Electromagnetic Materials in Microwaves and Optics (Sept. 2013), pp. 142–144.

[55] G. W. Semenoff, V. Semenoff, and F. Zhou, "Domain Walls in Gapped Graphene", Physical Review Letters **101**, 087204 (2008).

[56] B. Bernevig and T. Hughes, *Bernevig, B.: Topological Insulators and Topological Superconductors* (Princeton University Press, 2013).

[57] P. Soltan-Panahi, J. Struck, P. Hauke, A. Bick, W. Plenkers, G. Meineke, C. Becker, P. Windpassinger, M. Lewenstein, and K. Sengstock, "Multi-component quantum gases in spin-dependent hexagonal lattices", Nature Physics **7**, 434–440 (2011).

[58] L. Tarruell, D. Greif, T. Uehlinger, G. Jotzu, and T. Esslinger, "Creating, moving and merging Dirac points with a Fermi gas in a tunable honeycomb lattice", Nature **483**, 302–305 (2012).

[59] M. Polini, F. Guinea, M. Lewenstein, H. C. Manoharan, and V. Pellegrini, "Artificial honeycomb lattices for electrons, atoms and photons", Nature Nanotechnology **8**, 625–633 (2013).

[60] S. Yves, R. Fleury, T. Berthelot, M. Fink, F. Lemoult, and G. Lerosey, "Crystalline metamaterials for topological properties at subwavelength scales", Nature Communications **8**, 16023 (2017).

[61] H. Wang, A. P. Zhuravel, S. Indrajeet, B. G. Taketani, M. D. Hutchings, Y. Hao, F. Rouxinol, F. K. Wilhelm, M. LaHaye, A. V. Ustinov, and B. L. T. Plourde, "Mode Structure in Superconducting Metamaterial Transmission Line Resonators", arXiv:1812.02579 [cond-mat, physics:quant-ph] (2018).

[62] G. W. Semenoff, "Condensed-Matter Simulation of a Three-Dimensional Anomaly", Physical Review Letters **53**, 2449–2452 (1984).

[63] E. Akkermans and G. Montambaux, *Mesoscopic physics of electrons and photons*, OCLC: 174557159 (Cambridge University Press, Cambridge, 2007).

[64] S. Ryu and Y. Hatsugai, "Topological Origin of Zero-Energy Edge States in Particle-Hole Symmetric Systems", Physical Review Letters **89**, 077002 (2002).

[65] P. Delplace, D. Ullmo, and G. Montambaux, "Zak phase and the existence of edge states in graphene", Physical Review B **84**, 195452 (2011).

[66] M. Bellec, U. Kuhl, G. Montambaux, and F. Mortessagne, "Manipulation of edge states in microwave artificial graphene", New Journal of Physics **16**, 113023 (2014).

[67] J. Cayssol, "Introduction to Dirac materials and topological insulators", Comptes Rendus Physique **14**, 760–778 (2013).

[68] J.-N. Fuchs and M. O. Goerbig, "Introduction to the Physical Properties of Graphene", (2008).

[69] S. Ryu, C. Mudry, C.-Y. Hou, and C. Chamon, "Masses in graphenelike two-dimensional electronic systems: Topological defects in order parameters and their fractional exchange statistics", Physical Review B **80**, 205319 (2009).

[70] Y. Liu, C.-S. Lian, Y. Li, Y. Xu, and W. Duan, "Pseudospins and Topological Effects of Phonons in a Kekulé Lattice", Physical Review Letters **119**, 255901 (2017).

[71] W. Yao, S. A. Yang, and Q. Niu, "Edge States in Graphene: From Gapped Flat-Band to Gapless Chiral Modes", Physical Review Letters **102**, 096801 (2009).

[72] V. V. Albert, L. I. Glazman, and J. Liang, "Topological Properties of Linear Circuit Lattices", Physical Review L **114**, 173902 (2015).

[73] D. A. Powell, M. Lapine, M. V. Gorkunov, I. V. Shadrivov, and Y. S. Kivshar, "Metamaterial tuning by manipulation of near-field interaction", Physical Review B **82**, 155128 (2010).

[74] V. Lomanets, O. Zhuromskyy, G. Onishchukov, and U. Peschel, "Electrical circuit model of arrays of resonant elements", Physical Review B **85**, 125110 (2012).

[75] S. Y. Elnaggar, R. Tervo, and S. M. Mattar, "Energy Coupled Mode Theory for an arbitrary number of resonators", IEEE Transactions on Microwave Theory and Techniques **63**, 2115–2123 (2015).

[76] J. D. Jackson, *Classical electrodynamics*, 2d ed (Wiley, New York, 1975).

[77] D. L. Underwood, W. E. Shanks, A. C. Y. Li, L. Ateshian, J. Koch, and A. A. Houck, "Imaging Photon Lattice States by Scanning Defect Microscopy", Physical Review X **6**, 021044 (2016).

[78] A. P. Zhuravel, A. G. Sivakov, O. G. Turutanov, A. N. Omelyanchouk, S. M. Anlage, A. Lukashenko, A. V. Ustinov, and D. Abraimov, "Laser scanning microscopy of HTS films and devices (Review Article)", Low Temperature Physics **32**, 592–607 (2006).

[79] J. Gao, "The Physics of Superconducting Microwave Resonators", PhD thesis ().

[80] D. P. Pappas, M. R. Vissers, D. S. Wisbey, J. S. Kline, and J. Gao, "Two Level System Loss in Superconducting Microwave Resonators", IEEE Transactions on Applied Superconductivity **21**, 871–874 (2011).

[81] J. Noh, S. Huang, K. P. Chen, and M. C. Rechtsman, "Observation of Photonic Topological Valley Hall Edge States", Physical Review Letters **120**, 063902 (2018).

[82] V. M. Pereira, F. Guinea, J. M. B. Lopes dos Santos, N. M. R. Peres, and A. H. Castro Neto, "Disorder Induced Localized States in Graphene", Physical Review Letters **96**, 036801 (2006).

[83] A. Karpov, A. P. Zhuravel, A. S. Averkin, V. I. Chichkov, and A. V. Ustinov, "Phase-sensitive imaging of microwave currents in superconductive circuits", arXiv:1804.03026 [cond-mat, physics:physics] (2018).

[84] M. Ramezani Masir, D. Moldovan, and F. Peeters, "Pseudo magnetic field in strained graphene: Revisited", Solid State Communications **175-176**, 76–82 (2013).

[85] C. Poli, J. Arkinstall, and H. Schomerus, "Degeneracy doubling and sublattice polarization in strain-induced pseudo-Landau levels", Physical Review B **90**, 155418 (2014).

[86] G. Salerno, T. Ozawa, H. M. Price, and I. Carusotto, "Propagating edge states in strained honeycomb lattices", Physical Review B **95**, 245418 (2017).

[87] K. Fang, Z. Yu, and S. Fan, "Realizing effective magnetic field for photons by controlling the phase of dynamic modulation", Nature Photonics **6**, 782–787 (2012).

[88] J. Basset, D. Watfa, G. Aiello, M. Féchant, A. Morvan, J. Esteve, J. Gabelli, M. Aprili, R. Weil, A. Kasumov, H. Bouchiat, and R. Deblock, "Non-linear Hybrid Microwave Resonators Made by He-Beam Assisted Deposition of Tungsten Nanowires", arXiv:1811.06496 [cond-mat] (2018).

[89] L. Grünhaupt, M. Spiecker, D. Gusenkova, N. Maleeva, S. T. Skacel, I. Takmakov, F. Valenti, P. Winkel, H. Rotzinger, A. V. Ustinov, and I. M. Pop, "Granular aluminum: A superconducting material for high impedance quantum circuits", arXiv:1809.10646 [cond-mat, physics:quant-ph] (2018).

[90] D. Niepce, J. Burnett, and J. Bylander, "High Kinetic Inductance NbN Nanowire Superinductors", arXiv:1802.01723 [cond-mat] (2018).

université PARIS-SACLAY
ÉCOLE DOCTORALE
Physique en île-de-France (EDPIF)

Réseaux en nid d'abeille de résonateurs supraconducteurs: Observation d'états de bords topologiques de Semenoff

Mots clés : Circuits supraconducteurs, Réseau nid d'abeille, Isolant de Semenoff, État de bord, Topologie

Résumé : Cette thèse décrit la réalisation et l'étude de réseaux bidimensionnels de résonateurs supraconducteurs en nid d'abeille. Ce travail constitue un premier pas vers la simulation de systèmes de la matière condensée avec des circuits supraconducteurs. Ces réseaux sont micro-fabriqués et sont constitués de plusieurs centaines de sites. Afin d'observer les modes propres qui y apparaissent dans une gamme de fréquence entre 4 et 8 GHz, nous avons mis au point une technique d'imagerie. Celle-ci utilise la dissipation locale créée par un laser avec lequel nous pouvons adresser chaque site du réseau. Nous avons ainsi pu mesurer la structure de bande et caractériser les états de bord de nos réseaux. En particulier, nous avons observé les états localisés qui apparaissent à l'interface entre deux isolants de Semenoff ayant des masses opposées. Ces états, dits de Semenoff, sont d'origine topologique. Nos observations sont en excellent accord avec des simulations électromagnétiques ab initio.

Honeycomb lattices of superconducting microwave resonators: Observation of topological Semenoff edge states

Keywords: Superconducting circuits, Honeycomb lattice, Semenoff insulator, Edge states, Topology

Abstract: This thesis describes the realization and study of honeycomb lattices of superconducting resonators. This work is a first step towards the simulation of condensed matter systems with superconducting circuits. Our lattices are micro-fabricated and typically contains a few hundred sites. In order to observe the eigen-modes that appear between 4 and 8 GHz, we have developed a mode imaging technique based on the local dissipation introduced by a laser spot that we can move across the lattice. We have been able to measure the band structure and to characterize the edge states of our lattices. In particular, we observe localized states that appear at the interface between two Semenoff insulators with opposite masses. These states, called Semenoff states, have a topological origin. Our observations are in good agreement with ab initio electromagnetic simulations.

Université Paris-Saclay
Espace Technologique / Immeuble Discovery
Route de l'Orme aux Merisiers RD 128 / 91190 Saint-Aubin, France